

Pulse-shaping strategies in short-pulse fiber amplifiers

Dissertation

zur Erlangung des akademischen Grades

doctor rerum naturalium (Dr. rer. nat.)

vorgelegt dem Rat der Physikalisch-Astronomischen Fakultät
der Friedrich-Schiller-Universität Jena

von Dipl.-Phys. Damian Nikolaus Schimpf
geboren am 06.03.1980 in Halle (Saale)

Gutachter:

1. Prof. Dr. Andreas Tünnermann, Friedrich-Schiller-Universität Jena
2. Prof. Dr. Christian Spielmann, Friedrich-Schiller-Universität Jena
3. Prof. Dr. Franz. X. Kärtner, Massachusetts Institute of Technology

Tag der letzten Rigorosumsprüfung: 6. Januar 2010

Tag der öffentlichen Verteidigung: 9. Februar 2010

Contents

1	Introduction	1
2	Fundamentals of light propagation and amplification in optical fibers	3
2.1	Glass fibers as optical waveguides	3
2.2	Optical fibers as a solid-state laser concept	6
2.3	Pulse amplification	8
2.3.1	Pulse dynamics	9
2.3.2	Energy gain and extraction efficiency	11
2.4	Compensation of saturation-induced pulse-distortion	14
3	Ultrashort pulse propagation and amplification using optical fibers	19
3.1	Ultrashort pulses in optical fibers	19
3.2	Intramodal dispersion	20
3.3	Nonlinear effects	22
3.3.1	Nonlinear refraction and self-phase modulation	23
3.3.2	Stimulated Raman scattering	27
3.4	Challenges of direct ultrashort pulse amplification	27
3.5	Self-similar propagation and amplification	28
3.6	Concepts to generate high peak-power pulses and their limitations	29
3.6.1	Chirped pulse amplification	29
3.6.2	Large mode area fiber-amplifiers	31
4	Analysis of nonlinear chirped-pulse amplification	34
4.1	Analytical model for NLCPA	34
4.2	Evaluation of the pulse quality	39
4.3	Partial compensation of SPM using the compressor	39
5	Stability analysis of nonlinear CPA-systems	42
5.1	Influence of a weak post-pulse	44
5.1.1	Experimental observation of spectral distortions	44
5.1.2	Analysis of pulse-contrast degradation	45

5.2	Influence of weak spectral phase-modulation	51
6	Pulse-shaping strategies in nonlinear chirped pulse amplification	56
6.1	Compensation of SPM using fiber-dispersion	56
6.2	Partial compensation of SPM with GVD and TOD	65
6.3	Perfect compensation of SPM using a parabolic spectrum	69
6.4	Perfect compensation of SPM using phase-shaping	77
6.5	Peak-power scaling by using circularly polarized light	84
6.6	Comparision of techniques	89
7	Conclusion and Outlook	90

1 Introduction

Ultrashort pulse lasers are an important tool in scientific and industrial applications. Areas such as metrology, e.g. precision optical ranging, and biomedical imaging require short pulse durations. Furthermore, the high peak-powers of these lasers are exploited in applications such as frequency conversion, laser-matter-interactions, micromachining, and multi-photon spectroscopy. However, many applications are demanding higher average powers from these ultrashort pulse sources. This can be achieved by combining direct diode pumping with novel gain media designs. Laser geometries such as disk, slab and fiber have been introduced to compensate for thermo-optical effects, which limit the power scaling of conventional designs. In particular, fiber-lasers allow for excellent beam quality at ultrahigh average powers due to a diffraction-less propagation of radiation in the form of a spatial single mode. Continuous-wave fiber lasers with output powers of several kW in a single spatial mode are commercially available; and ultrashort pulse fiber lasers are approaching average powers in the kW range. However, the design of fiber lasers delivering pulses with high peak-powers is challenging due to the impact of nonlinear effects. In particular, the long interaction of the light with the material of the waveguide gives rise to this stringent limitation on ultrafast fiber amplifiers. The most dominant nonlinear effect is self-phase modulation which originates from the optical Kerr-effect. Typically, nonlinear effects must be avoided to prevent severe pulse distortions. To significantly reduce these detrimental effects in ultrashort pulse fiber amplifiers, the combination of chirped pulse amplification (CPA) and large mode area fibers is employed. Using these methods, the pulse energy of fiber lasers has been steadily increasing for the past few years. Recently, a fiber-based CPA-system has been demonstrated which produces pulse energies of around 1 mJ. However, both the stretching and the enlargement of the mode area are limited, and therefore, the impact of nonlinearity is still noticed in systems employing such devices. Having observed nonlinear effects even in state-of-the-art fiber amplifiers, the most pertinent question one can ask is, 'How to transcend the boundary set up by nonlinearity?'

The aim of this thesis is the analysis of CPA-systems operated beyond the conventional nonlinear limit, which corresponds to accumulated nonlinear phase-shifts around 1 rad. This will include a detailed discussion of self-phase modulation in such systems. A pri-

mary object is the control of this nonlinear effect. Experimental observations indicate that the impact of self-phase modulation on stretched pulses is different from the effect on nearly transform-limited pulses. To reveal the fundamental process, the complex pulse dynamics in chirped pulse amplification systems must be reduced to its essential part. This should allow identification of the key parameters. The emphasis of this thesis is placed on the design of novel concepts to control the impact of self-phase modulation in fiber-based chirped pulse amplification. For example, it is well known that self-phase modulation is strongly affected by the pulse shape, and thus, pulse-shaping is regarded as a powerful tool to accomplish this goal. For this reason, the potential of adaptive amplitude shaping, as well as phase shaping, is examined.

This thesis is organized as follows. Chapter 2 introduces pulse-amplification with rare-earth doped fiber amplifiers. Saturation is analyzed in short-pulse fiber amplifiers. Emphasis is placed on pre-compensation of saturation-induced pulse distortion, which is demonstrated in a nanosecond-pulse all-fiber amplification system. Chapter 3 discusses ultrashort pulse propagation. Dispersion and nonlinear effects are introduced. The issues limiting conventional fiber-based amplification of ultrashort pulses are discussed. In chapter 4 the influence of self-phase modulation on the output pulse of chirped pulse amplification systems is revealed. An analytical model is presented. In chapter 5 some of the phenomena limiting nonlinear CPA-systems are identified. In chapter 6, novel methods to control the impact of SPM on the output pulse are experimentally demonstrated. The design of these concepts is based on the theoretical findings. Both amplitude- and phase-shaping are studied. Model-based phase-shaping is implemented in a state-of-the-art fiber CPA-system. The influence of the polarization state is also highlighted. Additionally, existing techniques and recent advances are put into context. Finally, chapter 7 summarizes this thesis.

2 Fundamentals of light propagation and amplification in optical fibers

This chapter aims to provide an overview of the key aspects of light propagation and amplification in fibers. In the first section, modal analysis is employed to describe optical waveguiding in passive fibers. The second part describes pulse amplification in Ytterbium-doped fibers. The fiber is introduced as a solid-state laser concept. Then, the dynamics of nanosecond pulse amplification are discussed. This includes saturation effects. Based on these findings, the pre-compensation of saturation-induced pulse-deformation in an all-fiber amplification system is experimentally demonstrated.

2.1 Glass fibers as optical waveguides

A standard optical fiber guides light in its core by total internal reflection. A representative example of a step index fiber is shown in Fig. 2.1(a). The shaded central region denotes the core, which is surrounded by the cladding. The corresponding refractive index profile of this fiber is shown below. The uniform refractive indexes of the core and cladding are denoted by n_{co} and n_{cl} , respectively. These parameters can be combined with the free-space wavelength λ of light and the core-radius r_{co} , to form a single dimensionless parameter V , which is given by [1]

$$V = \frac{2\pi}{\lambda} r_{\text{co}} \sqrt{n_{\text{co}}^2 - n_{\text{cl}}^2} = \frac{2\pi}{\lambda} r_{\text{co}} NA \quad (2.1)$$

where NA denotes the numerical aperture of the fiber.

In the case of a microstructured fiber, an arrangement of channels of low index material (e.g. air 'holes') running along the fiber provides the confinement and guidance of light [2], as shown in Fig. 2.1(b). To calculate the V -parameter for such fibers, the core radius and the cladding index must be replaced by effective characteristics [3, 4].

After a spatial transient, a finite number of bound modes provide a complete description of linear light propagation in passive waveguides [1]. Due to the translational invariance of the waveguide (along the z -axis), the fields of the modes can be separated into parts depending on the transverse Cartesian coordinates, $\mathbf{e}_j(x, y, \omega)$, and a z -dependent term $\exp(i\beta_j(\omega)z)$. The propagation constant of the j -th mode is denoted by $\beta_j(\omega)$, and ω

2.1 Glass fibers as optical waveguides

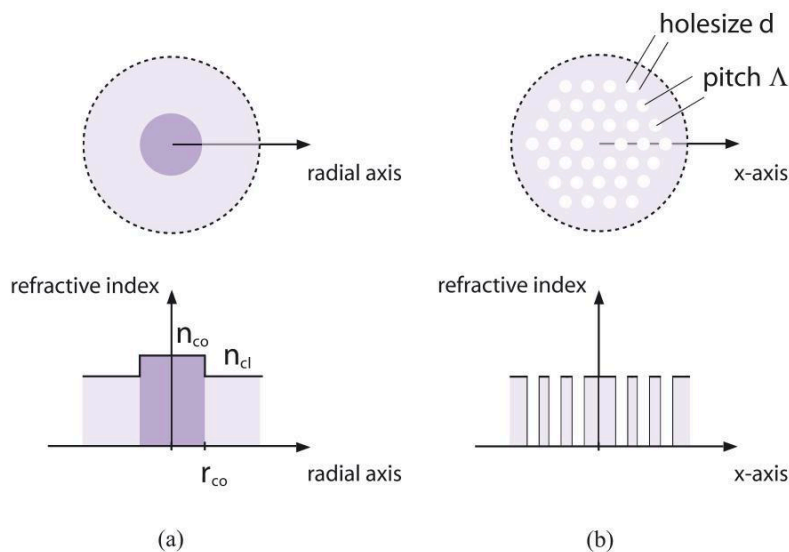


Figure 2.1: (a) Step index fiber, and (b) microstructured fiber which is also known as photonic crystal fiber; the transverse section of the fiber (top) and the refractive index profile (bottom) are shown.

stands for the angular frequency. The effective index of the j -th mode, $n_{\text{eff},j}$ and the propagation constant are related by $\beta_j(\omega) = \frac{\omega}{c} n_{\text{eff},j}(\omega)$.

The guided fields of the waveguide can be represented by an expansion over these modes [1]:

$$\tilde{\mathbf{E}}(x, y, z, \omega) = \sum_j a_j \mathbf{e}_j(x, y, \omega) \exp(i\beta_j(\omega)z) + \sum_j a_{-j} \mathbf{e}_{-j}(x, y, \omega) \exp(-i\beta_j(\omega)z), \quad (2.2)$$

where $j = 1, 2, \dots, M$. The total number of forward- or backward-propagating modes is M . The first and second summation are over the forward and backward propagating modes, respectively. The coefficients a_j denote the modal amplitudes.

The magnetic field is expanded in a similar way. Then, the solutions for the vectorial modes are obtained from Maxwell equations [1, 5]. The refractive index profile of the waveguide determines both the mode-field $\mathbf{e}(x, y, \omega)$ and its propagation constant $\beta_j(\omega)$, which are explicitly obtained from an eigenvalue equation [1]. The magnetic and electric fields are coupled unless the fields are independent of azimuth angle [1, 5]. The TE and TM modes are azimuthally symmetric; HE and EH hybrid modes correspond to modes where both E_z and H_z are nonzero. In general, numerical methods must be employed to obtain the mode-fields and propagation constants, e.g. as shown in [6].

For a circularly symmetric step index fiber with $V=5$, the intensity distributions as well

2.1 Glass fibers as optical waveguides

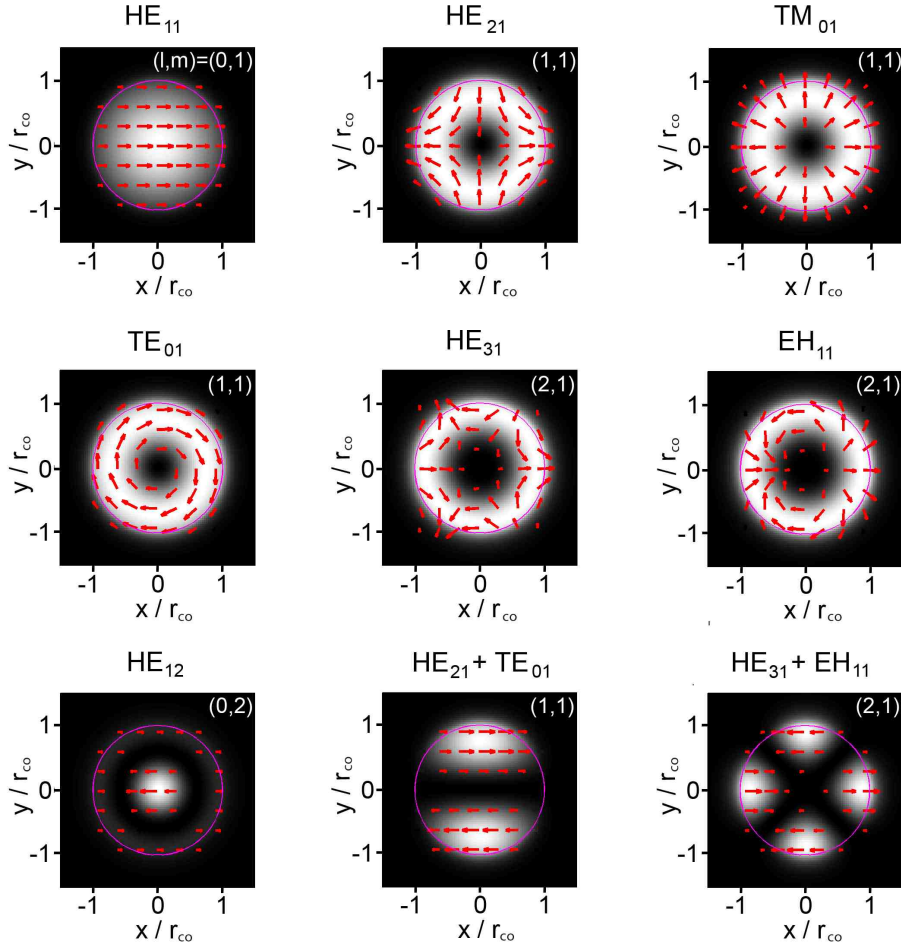


Figure 2.2: Intensity distributions (gray scale) and the transverse electric field vectors (red arrows) of the bound modes of a step-index silica fiber ($V=5$, $r_{co} = 40 \mu\text{m}$, $\lambda = 1.03 \mu\text{m}$).

as the transverse electric field vectors of the modes are shown in Fig. 2.2, where the indices (l,m) refer to the commonly used LP_{lm} -modes (i.e., the scalar description of the modes of a step-index fiber).

For a weakly-guiding step index fiber (i.e. $NA \ll 1$) the electric fields and the propagation constants can be calculated by using analytical expressions [1]. Each mode possesses its own propagation constant. Conventionally, the dimensionless parameter U is introduced as follows $U = \frac{2\pi}{\lambda} r_{co} (n_{co}^2 - n_{eff}^2)^{1/2}$. Fig. 2.3 shows the values of the parameter U as a function of the parameter V for a weakly guiding step-index fiber. It can be seen that the value of V determines the number of guided modes. For $0 < V < 2.405$, the fiber guides only the fundamental mode HE_{11} . In this regime, a fiber amplifier exhibits

2.2 Optical fibers as a solid-state laser concept

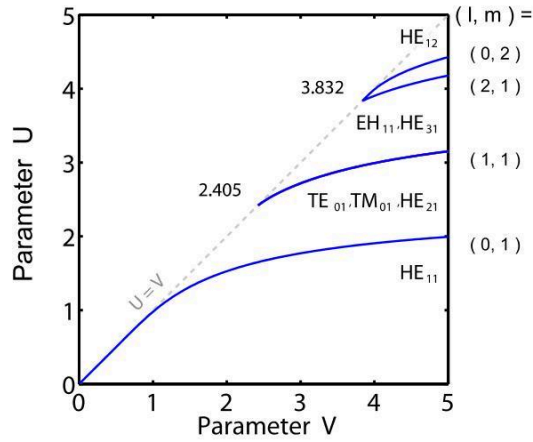


Figure 2.3: Values of the parameter U (related to β_j) as a function of the parameter V for a weakly guiding step-index fiber.

superior beam quality and brightness. The latter is defined as the power per emitter-area per solid-angle divergence of the beam [7]. Furthermore, single mode operation is also required for pulsed fiber amplification systems: if light propagates in more than one mode, the different propagation constants cause temporal spreading of the pulse. This is called intermodal dispersion and is particularly detrimental for ultrashort pulse-amplification. Another cause of pulse broadening originates from intramodal dispersion, which arises from the finite bandwidth of the input signal. This will be discussed in the context of ultrashort pulses in section 3.2.

2.2 Optical fibers as a solid-state laser concept

The simplest fiber-amplifier concept is a doped core surrounded by a single cladding. However, these single-clad fibers are of limited practicality since both the pump and the laser radiation are guided in the active core. In particular, the pump must exhibit a very high brightness. Therefore, the brightness of the single clad fiber-amplifier is limited either by available pump brightness or a degraded beam-quality because of a multimode core. The double-clad concept circumvents this draw-back by surrounding the active core with a second, highly multimode waveguide for the pump light [8]. The idea is illustrated in Fig. 2.4. Coiling a fiber with a cylindrical pump core in a kidney-shape enhances the pump-radiation absorption [9]. The pump-absorption can also be improved by using a non-cylindrical pump-core [10].

The double clad concept offers the combination of excellent signal beam-quality (fundamental mode operation) with efficient diode-pumping and good thermo-optical properties

2.2 Optical fibers as a solid-state laser concept

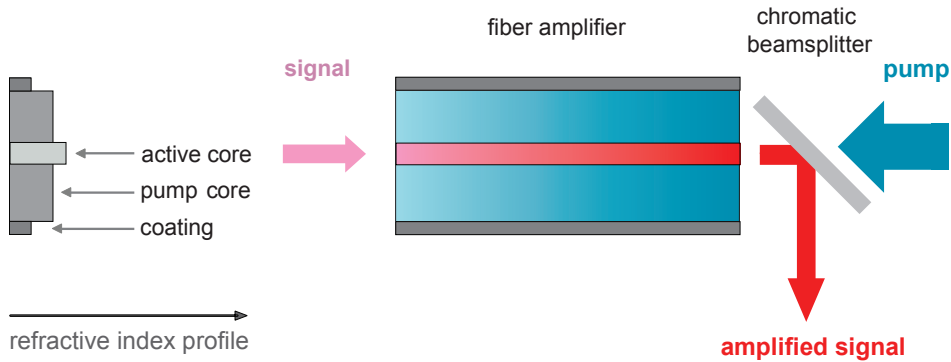


Figure 2.4: Schematic of the double-clad concept for high power fiber-amplifiers

(due to large outer surface of the fiber in relation to the active volume). Thus, single mode fiber lasers possess excellent brightness, which is advantageous for applications such as remote material processing. A drawback is the reduced pump light absorption which results in longer fiber-lengths enforcing nonlinear effects.

Fiber amplifiers feature a high single-pass gain, and thus, no complicated laser architectures are required. Another advantage is the prospect of an all-fiber design in which all components are fiber-integrated, leading to systems with paramount long term stability and compactness.

Throughout this work, Ytterbium-doped silica fibers are used. This gain medium has been extensively studied [11–13]. For the following analysis, knowledge of the emission and absorption cross-sections, as well as the lifetime of the upper state, are of particular significance. The emission and absorption cross-sections are shown in Fig. 2.5 (data according to [14]). The main spectral features are due to the Stark levels of the ground manifold $^2F_{7/2}$ and the excited manifold $^2F_{5/2}$ of the Yb^{3+} ions [11]. The emission and absorption cross-sections can be related to each other by using the McCumber theory [15]. According to this theory, it is also possible to calculate the radiative lifetime of the excited states from the emission cross-sections. The cross-sections depend on the temperature [16], and the co-doping [17]. However, for simplicity, these issues are not accounted for in the following analysis.

2.3 Pulse amplification

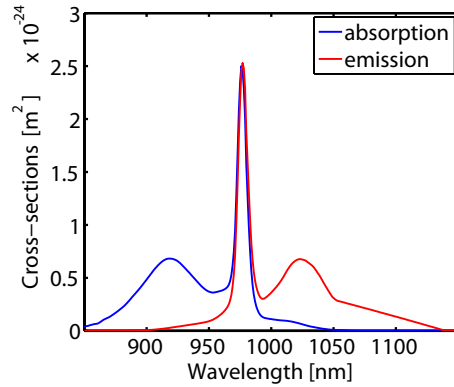


Figure 2.5: Absorption and emission cross-section of Ytterbium in a germanosilicate host (data according to [14]).

2.3 Pulse amplification

Although Ytterbium-doped glass possesses a higher saturation fluence (as defined in Eq. 2.7) than other gain-media (resulting in superior energy-storage capabilities) [18], the small mode-areas of single-mode fibers lead to saturation at pulse-energies in the μJ -range. This causes saturation-induced pulse-deformation at moderate pulse-energies. Fig. 2.6 shows experimental data illustrating the distortion of a rectangular input pulse due to saturation. In the following this behavior is quantitatively described. The energy gain and extraction efficiency are introduced as primary features of a fiber amplifier.

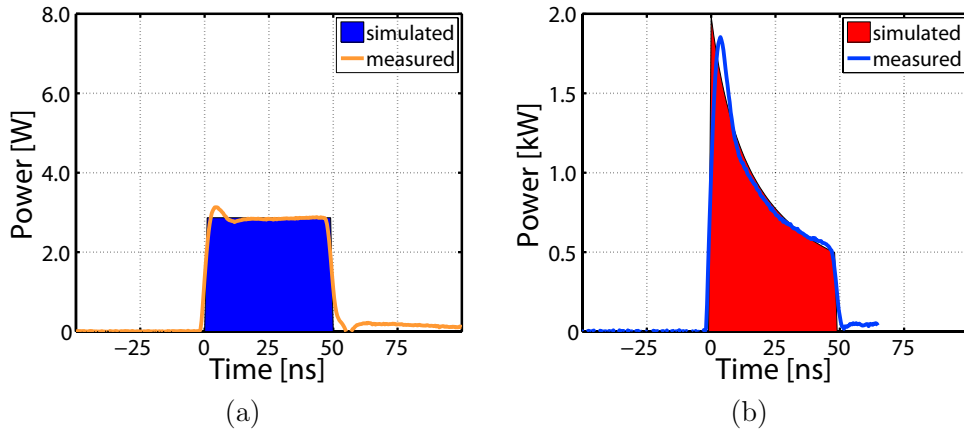


Figure 2.6: (a) Rectangular input pulse, (b) corresponding output pulse which is deformed due to saturation. The solid lines are experimental data. The parameters of the simulation are as follows: The saturation fluence at a signal wavelength of ~ 1030 nm is $J_{sat} = 30$ J/cm², the mode-field diameter is 11 μm , and the small signal gain G_0 is 780.

2.3 Pulse amplification

2.3.1 Pulse dynamics

In general, the interaction of light and matter is described by the Maxwell-Bloch-equations [19,20]. However, the analysis can be simplified if the spectrum of the laser-pulse is narrower than the spectral width of the gain profile of the active medium [19,21]. This is the case in almost all experimental situations of this work. Then, the laser-dynamics can be described by the rate equations [7,22]. Furthermore, if the events taking place during amplification are fast compared to the time-scale of the pump process (i.e., the inverse of the pumping rate) and the time-scale of the spontaneous emission, then the pulse amplification can be analytically described. In the following, light amplification in single-mode fibers is discussed. An one-dimensional problem is considered: the total density of dopants n_0 is assumed to be uniform along the gain medium; furthermore, the actual mode profile of the signal is neglected and an effective (average) intensity I over the doped area A_{dop} is considered. The rate-equations are given by

$$\left[\frac{\partial}{\partial z} + \frac{1}{v_G} \frac{\partial}{\partial t} \right] I(z, t) = \sigma \Delta(z, t) I(z, t), \quad (2.3)$$

$$\frac{\partial}{\partial t} \Delta(z, t) = -\sigma \Delta(z, t) I(z, t) / (h\nu_s), \quad (2.4)$$

where I is the intensity of the pulse. The group-velocity at the signal frequency ν_s is denoted by v_G , and $(h\nu_s)$ is the photon energy. The effective inversion population density is $\Delta(z, t)$, and is given by the term $n_2(z, t) - n_{tra}$, where n_2 and n_{tra} stand for the population-density of the excited states and the transparency inversion-density, respectively. And, n_{tra} is given by $n_0 \sigma_{12}^{(s)} / (\sigma_{12}^{(s)} + \sigma_{21}^{(s)})$, where the emission and absorption cross-sections at the signal wavelength are given by $\sigma_{21}^{(s)}$ and $\sigma_{12}^{(s)}$, respectively. The term σ stands for the sum $(\sigma_{21}^{(s)} + \sigma_{12}^{(s)})$. The z coordinate varies in the range of $0 \dots L$, where L is the fiber-length.

The analytical solution of Eqs. (2.3) and (2.4) is given by the Frantz-Nodvik-equations. One of the equations is a time-dependent radiation transfer equation which accounts for the effect of the radiation on the medium and vice versa [23]

$$I(z, t) = \frac{I_{in}(t - z/v_G)}{1 - [1 - G_0^{-1}(z)] \exp\left(-J_{sat}^{-1} \int_{-\infty}^{t-z/v_G} dt' I_{in}(t')\right)}, \quad (2.5)$$

$$\Delta(z, t) = \frac{\Delta_0(z)}{1 - \left[1 - \exp\left(J_{sat}^{-1} \int_{-\infty}^{t-z/v_G} dt' I_{in}(t')\right)\right] G_0(z)}. \quad (2.6)$$

The Frantz-Nodvik-equations (2.5) and (2.6) are valid for any arbitrary input pulse-shape I_{in} and any initial inversion-distribution $\Delta_0(z)$ that was built up by pumping.

2.3 Pulse amplification

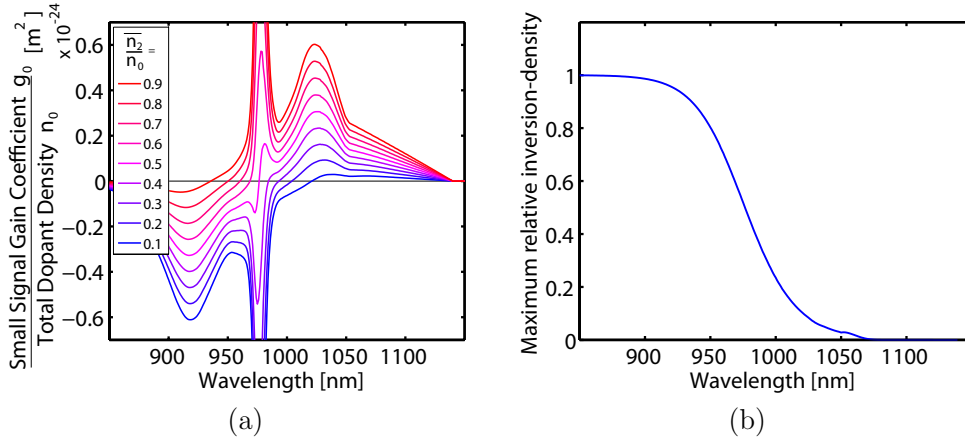


Figure 2.7: (a) Small signal gain coefficient as a function of wavelength at different (average) inversion levels \bar{n}_2/n_0 . (b) Maximum inversion n_2/n_0 as a function of pump-wavelength.

The equations depend only on two main parameters of the gain medium: the saturation fluence J_{sat} and the initial small signal-gain G_0 . The saturation fluence is given by

$$J_{sat} = \frac{h\nu_s}{\sigma_{12}^{(s)} + \sigma_{21}^{(s)}}, \quad (2.7)$$

and is related to the saturation energy by

$$E_{sat} = J_{sat} A_{dop}. \quad (2.8)$$

The small signal gain of the entire amplifier ($z=L$) can be written as

$$G_0 = \exp\left(\sigma \int_0^L dz' \Delta_0(z')\right) = \exp(g_0 L), \quad (2.9)$$

where the small signal gain coefficient g_0 is given by

$$g_0 = \sigma \bar{\Delta}_0 = \left[\sigma_{21}^{(s)} \bar{n}_2 - \sigma_{12}^{(s)} (n_0 - \bar{n}_2) \right], \quad (2.10)$$

where $\bar{\Delta}_0$ is the average effective inversion before the signal propagates through the amplifier, $\bar{\Delta}_0 = \frac{1}{L} \int_0^L dz' \Delta_0(z')$; and \bar{n}_2 is the average initial inversion. Fig. 2.7(a) shows the small signal gain coefficient for different average inversion levels. It is worth noting that the maximum possible (local) inversion level ($\max(n_2/n_0)$) is dependent on the pump-wavelength. Fig. 2.7(b) shows the maximum possible inversion level, i.e. $\max(n_2/n_0) = \sigma_{12}^{(p)} / (\sigma_{12}^{(p)} + \sigma_{21}^{(p)})$, as a function of the pump-wavelength, where the emission and absorption cross-sections at the pump wavelength are denoted by $\sigma_{21}^{(p)}$ and $\sigma_{12}^{(p)}$, respectively. Local inversion levels > 0.9 are possible by pumping at a wavelength around 920 nm. This results in a high energy stored in the amplifier. The stored energy

2.3 Pulse amplification

E_{sto} is defined as [7]

$$E_{sto} = (h\nu_s) \overline{\Delta_0} (A_{dop}L). \quad (2.11)$$

However, the smaller absorption cross-section at a wavelength of 920 nm compared to 975 nm causes longer absorption lengths, and thus, longer fiber-lengths. For the amplification of ultrashort pulses using self-similar propagation (see section 3.5), this is advantageous. However, for chirped-pulse amplification (see section 3.6.1), this is a drawback since a longer fiber length enhances nonlinear effects.

The Frantz-Nodvik-equations (2.5) and (2.6) reveal important aspects of the pulse-dynamics in laser amplifiers: Eq. (2.5) shows that the output pulse-shape is only dependent on the total inversion in the fiber, and not on the particular inversion distribution across the fiber. And, Eq. (2.6) shows that the final inversion-distribution depends only on the energy of the input pulse and not on its shape.

Fig. 2.6 shows the deformation of a rectangular input pulse due to saturation. The Frantz-Nodvik-equation (2.5) describes this pulse distortion. Such a deformation can be observed if the pulse-energy approaches the saturation energy of the amplifier. In particular, the leading part of the pulse significantly depletes the inversion. The reduced inversion results in a lower gain for the trailing part of the pulse.

The Frantz-Nodvik-equations are only valid if nonlinear effects, such as the stimulated Raman-scattering and Four-wave mixing, as well as amplified spontaneous emission, are negligible. To obtain high quality pulse amplification, these effects must be minimized.

2.3.2 Energy gain and extraction efficiency

The evaluation of the pulse amplification requires a relation for the pulse energy as function of the input pulse energy and the amplifier parameters. Temporal integration of Eq. (2.5) leads to an expression for the pulse-energy:

$$E(z) = E_{sat} \ln \left[1 + G_0(z) \left(\exp \left(\frac{E_{in}}{E_{sat}} \right) - 1 \right) \right] \quad (2.12)$$

This result is valid for any arbitrary input pulse-shape $I_{in}(t)$. The pulse-energy at the output of the amplifier is given by $E_{out} = E(z = L)$. Eq. (2.12) shows that the output pulse-energy depends neither on the temporal pulse-shape nor on the spatial distribution of the inversion. The important parameters are, instead, the input pulse-energy and the total initial inversion. Fig. 2.8 shows the output energy as a function of the input energy and the small signal gain. To achieve a certain output energy, low input energies require a high stored energy ($\sim \ln(G_0)$, see Eq. (2.11)). Alternatively, the input energy may

2.3 Pulse amplification

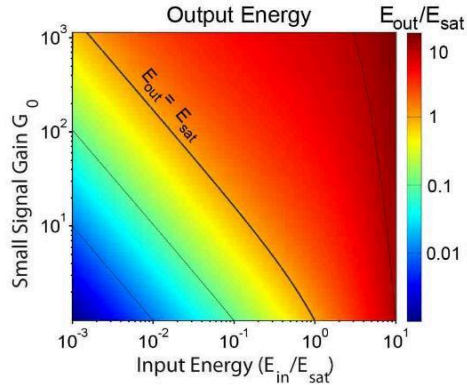


Figure 2.8: Output energy (relative to the saturation energy) as a function of input energy and small signal gain for a single pass amplifier.

be increased at lower stored energies. The amount of stored energy is influenced by the pump level and amplifier length. In practice a chain of amplifiers is usually employed to amplify low seed energies.

Knowing the output pulse-energy, the gain and the extraction efficiency of a laser-amplifier can be calculated. The energy gain G is given by [7]

$$G = \frac{E_{out}}{E_{in}}. \quad (2.13)$$

There are two extreme regimes of amplification: the case of small-signal amplification and the complete saturation of the amplifier. If the input energy is low, the differential energy-growth is linear ($dE/dz = g_0 E$) and Eq. (2.13) can be approximated by $G \approx G_0$. At high-level input signals, the energy-growth 'saturates' and the differential energy-growth is constant ($dE/dz = g_0 E_{sat}$), i.e. every excited state contributes its stimulated emission. Thus, the most efficient conversion of stored energy to pulse-energy is obtained. Eq. (2.13) can be approximated by $G \approx 1 + \ln(G_0) E_{sat}/E_{in}$.

The energy extraction efficiency η is given by [7]

$$\eta = \frac{E_{out} - E_{in}}{E_{sto}}. \quad (2.14)$$

The best extraction efficiency is achieved with complete saturation of the amplifier. The energy gain and extraction efficiency depend only on the input energy E_{in} (relative to the saturation energy E_{sat}) and on the small signal gain G_0 . Fig. 2.9 shows the energy gain and the energy extraction efficiency as a function of these two parameters. It is worth noting that the small-signal gain on the y-axis is directly related to the stored energy, see Eq. (2.11). It can be seen that it is impossible to obtain both maximum gain and maximum extraction efficiency. As mentioned before, efficient energy extraction requires

2.3 Pulse amplification

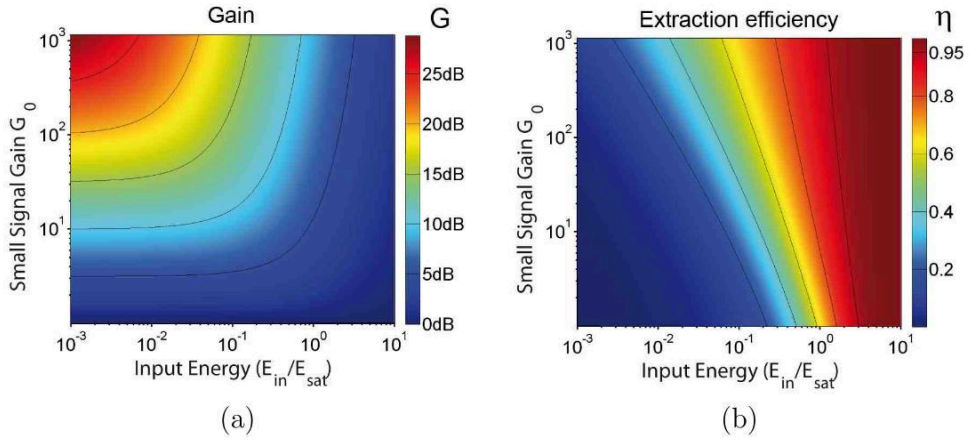


Figure 2.9: (a) Energy gain, and (b) energy extraction efficiency as a function of input energy and small signal gain for a single pass amplifier.

input pulse-energies comparable to the saturation energy. Thus, multiple amplifier stages (alternatively, multiple passes) are used in practice. The pre-amplifiers provide high gain in order to reach efficiency for the main amplifier.

Furthermore, the energy growth is related to the depletion of the (average) inversion. This aspect is particularly important for the understanding of saturation and the pre-compensation of pulse-distortion, which is discussed in the next section.

For this reason, a spatial integration of Eq. (2.6) after the propagation of the signal pulse is performed, and using the expressions for the output energy and small signal gain, Eqs. (2.12) and (2.9), the following conservation law is obtained: [24]

$$A_{dop} \left[\int_0^z dz' n_{2,0}(z') - \int_0^z dz' n_2(z') \right] = \frac{E(z) - E_{in}}{h\nu_s}. \quad (2.15)$$

This balance states that the number of photons that are generated equals the number of excited states that are depleted.

Furthermore, Eq. (2.12) shows that pulses of the same energy but different shapes at the input of an amplifier will result in the same energy-growth behavior (at equal pump conditions). In turn, according to Eq. (2.15), they will also result in the same inversion-distribution in every section of the amplifier. According to Eq. (2.5), the input pulse-shape determines the output pulse-shape. Therefore, modifying the seed pulse-shape (but keeping its energy constant) will allow pre-compensation of any pulse-deformation due to saturation. The analysis is also valid for other laser amplifier concepts, and thus the following method can be applied to such systems as well.

2.4 Compensation of saturation-induced pulse-distortion

In the following, the pre-compensation of pulse distortion due to saturation is discussed. A key result is a simple analytical expression that predicts the input pulse-shape required to obtain any arbitrary target pulse-shape at the output of a saturated amplifier [24]. This relation is derived from the rate-equations and can be regarded as the inverse of the Frantz-Nodvik-equation. Its significance from an experimental point of view is highlighted. The usefulness of this expression is experimentally demonstrated using an all-fiber amplifier chain seeded with a directly modulated laser-diode. This method will prove useful in those applications of high-power, high-energy laser-amplifier systems that require particular pulse-shapes in order to be efficient, e.g. micromachining and scientific light-matter-interaction experiments [25].

Conventionally, numerical calculations have determined the input pulse-shapes that produce special pulse-shapes at the output of saturated amplifiers [22]. However, experimental techniques do not directly benefit from such simulations since they do not reveal the key parameters of the process. To experimentally generate target pulse-shapes at the output of saturated amplifiers, real-world systems have conventionally employed feed-back loops that were combined with the representation of pulse-shapes by temporal slices, e.g. [26], alternatively, by parameterized pulse-shape segments [27]. However, with increasing complexity of the target pulse-shape, the number of variables, and thus, the number of feedback loops is growing. Therefore, there is a high interest in developing an analytical model which reveals the main functionality and the key parameters for pre-compensation of pulse-distortions due to saturation. The input pulse-shape is modified in order to compensate saturation effects.

When integrating Eq. (2.5) to obtain Eq. (2.12), it is found that Eq. (2.12) is valid even if incomplete pulse-areas at the input and at the output of the amplifier are considered, i.e. using $\int_{z/c}^{t+z/c} dt' I(z, t')$ instead of the complete pulse-area $\int_{z/c}^{\tau+z/c} dt' I(z, t')$ at $z = L$ and $z = 0$. The temporal window in which the pulse is located is denoted by τ . Thus, solving Eq. (2.12) for $\int_0^t dt' I_{in}(t')$ and subsequent differentiation with respect to time t results in an expression for the input pulse-shape as a function of the target pulse-shape at the output: [24]

$$I_{in}(t) = \frac{I_{out}(t)}{1 - [1 - G_0] \exp\left(-J_{sat}^{-1} \int_0^t dt' I_{out}(t')\right)}. \quad (2.16)$$

Eqs. (2.16) and (2.5) have the same form except that the roles of $I_{out}(t)$ and $I_{in}(t)$ are interchanged and the integration direction over the inversion-distribution is reversed,

2.4 Compensation of saturation-induced pulse-distortion

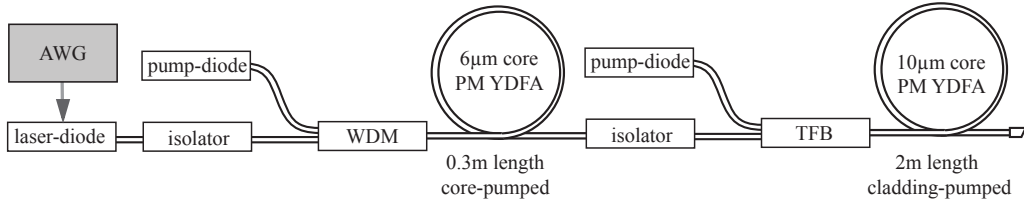


Figure 2.10: Schematic of the all-fiber amplifier system: the current of the laser-diode is driven by the arbitrary waveform generator (AWG), the first Ytterbium-doped fiber-amplifier (YDFA) is core-pumped using a wavelength division multiplexer (WDM), the second YDFA is cladding pumped using a tapered fibre bundle (TFB) pump-coupler

i.e. G_0^{-1} is replaced by G_0 . Therefore, Eq. (2.16) can be regarded as an inverse Frantz-Nodvik-equation. This equation determines the optimum seed pulse-shape to obtain any arbitrary target pulse-shape at the output of a saturated amplifier. For example, if the target is a square pulse, i.e. $I_{out}(t) = \hat{I}$ for $0 \leq t \leq \tau$ and zero otherwise, then the corresponding input pulse-shape has to be $I_{in}(t) = \hat{I} \left(1 - [1 - G_0] \exp(-\hat{I} t / J_{sat}) \right)^{-1}$ for $0 \leq t \leq \tau$ (and zero otherwise). For more complex target pulse-shapes, a numerical integration in the denominator has to be performed.

To pre-compensate pulse-deformation due to saturation, the shape and energy of the input pulse, as well as the saturation fluence and the small signal-gain of the amplifier, are required. These parameters can be obtained from the deformation of a pulse with known shape. If a certain input pulse (e.g., rectangle) is amplified, a fit of the expected output pulse-shape, using Eq. (2.5), will determine the desired parameters. Then, Eq. (2.16) can be applied. Another way is also possible: The saturation fluence is usually known from spectroscopic measurement of the emission and absorption cross-sections (e.g., provided by the fiber manufacturer). Furthermore, in the previous section it was shown that input pulses of different shapes but equal energies result in the same output pulse-energy and the same inversion. Therefore, the small signal gain can be obtained from the energies measured at the input and output and using Eq. (2.12).

To experimentally demonstrate the pre-compensation using the inverse Frantz-Nodvik-equation (2.16), an all-fiber system is designed. The schematic of the system is shown in Fig. 2.10. The master oscillator is a commercially available, fiber pigtailed laser-diode emitting light at a central wavelength of about 1030 nm and with a maximum peak-power of about 0.5 W. The current applied to the laser-diode is controlled by an arbitrary wave-form generator (AWG). The maximum sample rate is 1.1 GS/s and the vertical resolution is 12 bits. The rise times of the AWG and the laser-diode are around 700 ps and 5 ns, respectively. This precludes the generation of optical pulses exhibiting

2.4 Compensation of saturation-induced pulse-distortion

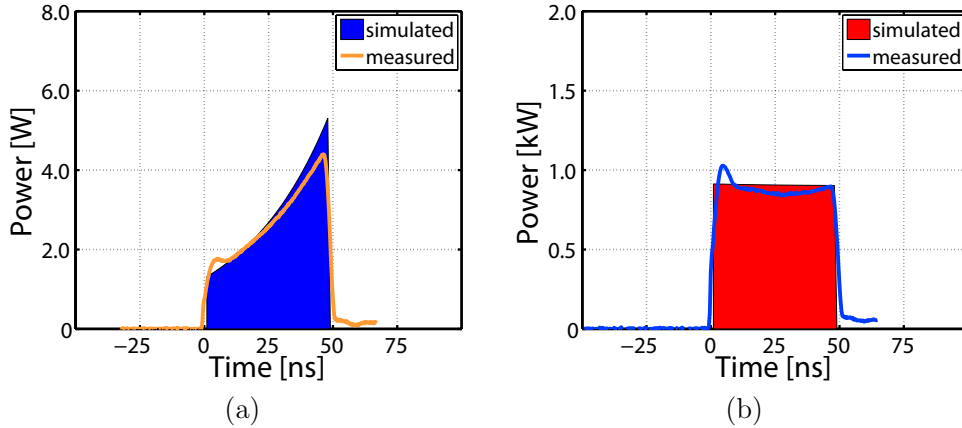


Figure 2.11: (a) Input pulse which pre-compensates the saturation-induced pulse-deformation in order to obtain a rectangular output pulse (b). The solid lines are experimental data. For the calculation of the input pulse, the parameters of Fig. 2.6 were used.

fine structures. In all the experiments, the repetition rate is set to 10 kHz. The pulse-energy is boosted in an all-fiber chain consisting of a pre- and main-amplifier. These Ytterbium-doped fiber-amplifiers are cladding pumped using pig-tailed c.w. laser diodes. The pump wavelength is about 975 nm. The pump delivery fibers are spliced with the fiber-amplifiers. In the amplifiers, the pump light propagates in the same direction as the signal pulse. The mode-field diameter of the main amplifier is about 11 μm . The pulse-distortion due to saturation occurs in the main-amplifier. This was verified by observing the signal at the output of the main amplifier while the pump (at a wavelength of 975 nm) was turned off. The seed into the main amplifier could be also monitored. All pulse-shapes are measured using an InGaAs photodetector (rise time about 100 ps) and a fast oscilloscope (500 MHz and 5 GS/s). Stimulated Raman scattering is neither observed in the experiments nor expected from numerical simulations.

To produce a target pulse-shape from a saturated amplifier, the input pulse-shape can be calculated using Eq. (2.16). The key parameters are determined by reproducing the deformation of a known input shape. Here, the Frantz-Nodvik-equation (2.5) is applied to the distortion of the rectangular input pulse. The experimental data has already been shown in Fig. 2.6. The fiber manufacturer provides the emission and absorption cross-sections, the number of dopants and the fluorescence lifetime [14].

At first, the pre-compensation technique is demonstrated with a rectangular output pulse-shape. The corresponding input pulse-shape is calculated using Eq. (2.16). This profile is then loaded into the arbitrary wave-form generator that drives the current of the laser-diode. The seed into the main-amplifier as well as the calculated profile are

2.4 Compensation of saturation-induced pulse-distortion

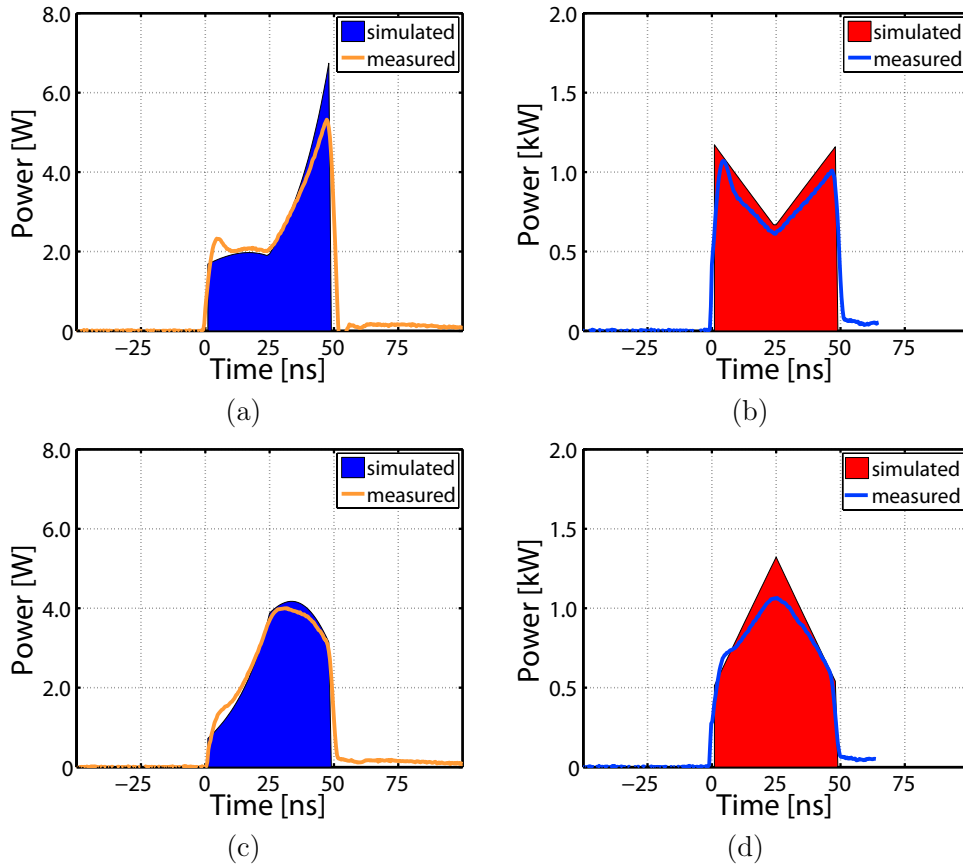


Figure 2.12: (a) Input pulse, (b) and the corresponding 'M'-shaped output pulse. (c) input pulse to generate a 'house'-shaped output (d). The solid lines are experimental data. For the calculation of the input pulse, the parameters of Fig. 2.6 and 2.11 were used.

shown in Fig. 2.11(a). The corresponding output of the fiber MOPA-system and its simulation can be seen in Fig. 2.11(b). Such rectangular output pulses can increase the output pulse energy extractable from a fiber-amplifier, before nonlinear effects, such as stimulated Raman scattering, appear. In particular, pulse-distortion can result in high peak-powers in the final section of the fiber-amplifier (as shown in Fig. 2.6), however, using the pre-compensation, the peak-powers are reduced (see Fig. 2.11). As a consequence, the critical power for Stimulated Raman-scattering is not reached.

Fig. 2.12 demonstrates that other target pulse-shapes can be produced without additional effort. In particular, the number of parameters of Eq. (2.16) does not increase even if more complex output pulse-shapes are produced. Except for the shape of the target pulse, the same parameters as for the generation of the rectangular pulse can be used. Fig. 2.12(a) shows the calculated and then measured input pulse-shapes to obtain

2.4 Compensation of saturation-induced pulse-distortion

a 'M'-shaped output pulse. The target pulse and the measurement of its experimental production are shown in Fig. 2.12(b). To further demonstrate the versatility of the technique a 'house'-shaped output pulse is generated. Experimental data and the target can be seen in Fig. 2.12(d). The corresponding input data are shown in Fig. 2.12(c).

The deviation between experimental data and simulation originates from the response of the master oscillator. First, the response time (≈ 5 ns) precludes the production of very fine temporal features being needed for perfect pre-compensation, as shown in Fig. 2.12(a). Second, the leading edge of the pulse shows an overshoot. If the experimental pulse shape is the input for the simulation, then the experimental output pulse-shape is well reproduced, i.e. the model works fine. However, the generation of specified output pulse shapes is the aim. Thus, the method is limited by the response.

Furthermore, it was experimentally observed that stimulated Brillouin-scattering limits the pulse-shaping. To pre-compensate for strong pulse-distortion, input pulse-shapes with strong amplitude variations are required. However, the dynamic range of a Fabry-Perot diode without wavelength stabilization is limited, which results in high peaks being observed in the spectrum if the driving pulse of the AWG contains small amplitudes. These peaks lead to stimulated Brillouin scattering during amplification. Brillouin scattering can be reduced to some extent by using special fibers [28]. Significant decrease in efficiency for this process is achieved with a broader signal bandwidth, e.g. by using a super-luminescence laser-diode operated in pulsed mode.

To summarize, saturation is detrimental in nanosecond-pulse fiber amplifiers, in which it causes a strong deformation of the pulse. This phenomenon reduces the applicability of the output pulses. Starting with an analysis of saturation in short-pulse fiber amplifiers, a model for the pre-compensation of saturation-induced pulse distortion has been developed. Target pulses of arbitrary shapes have been generated from a saturated fiber amplifier by shaping of the input pulses according to the predictions of the model. The all-fiber design of the system makes this a versatile and compact source for real-world applications, e.g. micromachining. Thus, pulse-shaping extends the functionality of fiber lasers in practice. The analysis of this chapter can also calculate the energy-gain and efficiency of chirped-pulse amplification unless the spectrum is not strongly influenced by the spectral gain characteristics (i.e. spectral dependency of the cross-sections). Such considerations are important for the design of such systems. Furthermore, the model is the basis for an estimation of the amount of accumulated nonlinear phase (see 3.3.1). However, when the interaction of the temporal pulse dynamics and the spectral gain behavior is of interest [29], more advanced modelling is required, e.g. see [30].

3 Ultrashort pulse propagation and amplification using optical fibers

In the following the propagation of ultrashort pulse in fibers is discussed. Dispersion and nonlinear effects are introduced. Some of the phenomena making fiber-based ultrashort pulse amplification challenging are identified. Self-similar propagation in active optical fibers is then briefly discussed as one concept for direct fiber-based ultrashort pulse amplification. Subsequently, techniques to produce pulses with high peak-power are presented. The significance of chirped pulse amplification and large mode area fibers is highlighted, and some of their current limitations are identified.

3.1 Ultrashort pulses in optical fibers

Ultrashort temporal pulses are generated by modelocking [31]. They comprise a spectrum of sinusoidal waves spread over a finite band in frequency-domain. Conventionally, the complex spectral amplitudes at (angular) frequencies ω are defined as $\tilde{A}(z, \omega - \omega_0)$, where ω_0 denotes the central (angular) frequency of the spectrum.

In the following, an expression for an ultrashort pulse in a single mode optical fiber is derived under the assumption that the beam profile of the light source exactly matches one mode of the dispersive medium at the entrance. In the frequency domain, a general representation of an ultrashort pulse in a single mode fiber is found using Eq. (2.2)

$$\tilde{\mathbf{E}}(x, y, z, \omega) = \frac{1}{\sqrt{N}} \mathbf{e}(x, y, \omega) \tilde{A}(z, \omega - \omega_0) \quad (3.1)$$

where N is a dimensionless number that is introduced for the normalization of the field $\mathbf{e}(x, y, \omega)$. In particular, the modal power p (evaluated at $\omega = \omega_0$) results from the integration of the time-averaged Poynting vector over the infinite cross-section [1]: $p = \int dx \int dy \frac{1}{2} [\mathbf{e}(x, y, \omega_0) \times \mathbf{h}^*(x, y, \omega_0)] \cdot \hat{\mathbf{z}}$. For the case of weakly guiding fibers, it can be approximated as $p \approx \frac{1}{2} c \epsilon_0 n_0 \int dx \int dy |\mathbf{e}(x, y, z, \omega_0)|^2$, where the vacuum permittivity is denoted as ϵ_0 , c is speed of light in free-space and n_0 is the linear refractive index of the core. The normalization is then given by $N = p/(1\text{W})$.

3.2 Intramodal dispersion

The electric field of the temporal pulse takes the form

$$\begin{aligned}
\mathbf{E}(x, y, z, t) &= \text{Re} \left(\int \frac{d\omega}{2\pi} \frac{1}{\sqrt{N}} \mathbf{e}(x, y, \omega) \tilde{A}(z, \omega - \omega_0) e^{-i\omega t} \right) \\
&\approx \frac{1}{2} \frac{1}{\sqrt{N}} \mathbf{e}(x, y, \omega_0) e^{-i\omega_0 t} \left[\int \frac{d\omega}{2\pi} \tilde{A}(z, \omega - \omega_0) e^{-i(\omega - \omega_0)t} \right] + c.c. \\
&\approx \frac{1}{2} \frac{1}{\sqrt{N}} \mathbf{e}(x, y, \omega_0) e^{i(\beta_0 z - \omega_0 t)} A(z, T) + c.c., \tag{3.2}
\end{aligned}$$

where $A(z, T)$ denotes the complex slowly varying envelope amplitude of the pulse. The time is taken in a reference frame co-moving at the group-velocity v_G (evaluated at ω_0), $T = t - z/v_G$. In the next section an explicit form for $A(z, T)$ will be given. In Eq. (3.2) the frequency-dependence of the transverse field is neglected $\mathbf{e}(x, y, \omega) \approx \mathbf{e}(x, y, \omega_0)$.

In general, the temporal phase of the complex amplitude $|A(z, T)| e^{i\varphi(z, T)}$ is related to a variation of the instantaneous frequency across the pulse from the central frequency ω_0 . The chirp of a pulse is the difference, which is the time derivative $\delta\omega = -\frac{\partial\varphi}{\partial t}$. An up-chirp refers to an increase of frequency across the pulse. A down-chirp is a decrease. Furthermore, the temporal duration of a pulse is related to the bandwidth of its power-spectrum by the Fourier uncertainty-principle [32]. A pulse is transform-limited if its corresponding time-bandwidth-product is minimal. This corresponds to zero chirp across the pulse. Gaussian and hyperbolic secant pulses possess maximum peak power when they are transform-limited. This is not necessarily true for all shapes. For instance, if a cubic spectral phase is impressed on the amplitude spectrum of a parabolic temporal intensity-pulse, then a higher peak-power is obtained.

3.2 Intramodal dispersion

The group delay of every mode is frequency-dependent, since both the refractive index of the material and the propagation characteristics of a waveguide-mode depend on wavelength. The two components are denoted as material and waveguide dispersion, respectively. The combination is known as intramodal dispersion. In the following, the impact of this kind of dispersion on optical signals is discussed.

Using Eqs. (2.2) and (3.1), the complex amplitude $\tilde{A}(z, \omega - \omega_0)$ at z is given by

$$\tilde{A}(z, \omega - \omega_0) = \tilde{A}(0, \omega - \omega_0) e^{i\beta(\omega)z}, \tag{3.3}$$

and then the slowly varying envelope of the pulse is given by

$$A(z, T) \approx \int \frac{d\Omega}{2\pi} \exp \left(i \left[\frac{\phi^{(2)}}{2} \Omega^2 + \frac{\phi^{(3)}}{6} \Omega^3 \right] \right) \tilde{A}(0, \Omega) \exp(-i\Omega T), \tag{3.4}$$

3.2 Intramodal dispersion

where Ω stands for the difference $(\omega - \omega_0)$. In this expression, the spectral phase-term $\phi(\omega) = \beta(\omega)z$ has been expressed as a Taylor expansion around ω_0 :

$$\phi(\omega) = \beta(\omega)z = \left[\beta^{(0)} + \beta^{(1)}(\omega - \omega_0) + \frac{\beta^{(2)}}{2}(\omega - \omega_0)^2 + \frac{\beta^{(3)}}{6}(\omega - \omega_0)^3 + \dots \right] z. \quad (3.5)$$

Eq. (3.4) includes only second order dispersion and third order dispersion (TOD). Higher-order terms are significant for signals with broad bandwidths, such as ultrashort pulses with durations < 100 fs, and if the central wavelength of the signal is close to the zero-dispersion wavelength for which $\beta^{(2)} = 0$. For example, fused silica exhibits a zero-dispersion wavelength near $1.3 \mu\text{m}$. Furthermore, higher order terms are also relevant with regard to the compensation of self-phase modulation in chirped pulse amplification systems.

In the Taylor expansion, Eq. (3.5), the zero-order phase term is related to a constant phase (at fixed position z), which is particularly relevant to few cycle pulses. The first order term is related to the group-delay which is given by $T_G(\omega') = z/v_G(\omega') = \beta^{(1)}(\omega')z = \phi^{(1)}(\omega')$. The second order term is related to group-delay dispersion at the central frequency ω_0 . The impact of the group velocity dispersion on an ultrashort pulse may simply be considered in terms of the dispersion of the group delay for the different frequencies [33]. For a pulse of bandwidth $\Delta\omega$, the spread in propagation times can be approximated by $(dT_G/d\omega')\Delta\omega$. This pulse broadening per bandwidth is usually meant by 'dispersion' in the context of ultrafast lasers, and it is given by $(dT_G/d\omega') = z(d\beta^{(1)}(\omega')/d\omega') = z\beta^{(2)}(\omega') = \phi^{(2)}(\omega')$. Normal dispersion (also termed positive dispersion) is given for $\beta^{(2)} > 0$. Anomalous dispersion (also known as negative dispersion) corresponds to $\beta^{(2)} < 0$.

An optical fiber of length L is usually characterized by the dispersion parameter D in units [ps/nm/km], which is a function of the free-space wavelength λ and defined by [34]

$$D(\lambda) = \frac{1}{L} \frac{dT_G}{d\lambda} = \frac{d}{d\lambda} \frac{1}{v_G} = -\frac{2\pi c}{\lambda^2} \frac{d}{d\omega} \frac{1}{v_G} = -\frac{2\pi c}{\lambda^2} \beta^{(2)}(\omega). \quad (3.6)$$

Fig. 3.1 shows results of the experimental determination of the dispersion parameters of a telecom fiber (core-diameter $9 \mu\text{m}$, 'j-fiber IG-09/125/250') and a microstructured fiber ('crystal fiber NL-2.0-740'; a one-hole-missing-design with $\Lambda=1.4\mu\text{m}$ and $d=0.67\Lambda$) using the technique of spectral interferometry [35,36]. The experimental results (for the fundamental modes) are shown together with the theoretically expected dispersion curves of bulk fused silica (calculated using Sellmeier coefficients [34]) and the microstructured fiber using expressions for the output of the finite-element-method (FEM) [37].

3.3 Nonlinear effects

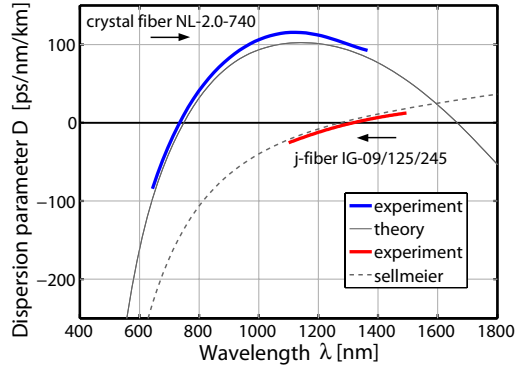


Figure 3.1: Experimental result of dispersion measurement of a $2\mu\text{m}$ -core microstructured fiber (blue curve) and the theoretical estimation (solid grey curve); and the dispersion curves of a telekom fiber (red curve) and bulk fused silica (dashed grey curve).

3.3 Nonlinear effects

The polarization $\mathbf{P}(\mathbf{t})$ of a medium under the influence of an applied electric field can be expressed in terms of a power series [38]

$$\mathbf{P}(\mathbf{t}) = \mathbf{P}^{(0)}(t) + \mathbf{P}^{(1)}(t) + \mathbf{P}^{(2)}(t) + \mathbf{P}^{(3)}(t) + \dots \quad (3.7)$$

where $\mathbf{P}^{(1)}$ is linear in the field and represents the non-instantaneous response of matter to stimulation by light, and corresponds to a frequency-dependent (refractive) index of the optical medium. The term $\mathbf{P}^{(2)}$ is quadratic, and $\mathbf{P}^{(3)}$ is cubic in the field, and so on. The term $\mathbf{P}^{(0)}$ describes a static polarization as found in some crystals. However, this term is irrelevant for fused silica, which is the medium of this work. Due to its isotropy, the third-order term is the lowest-order nonlinear contribution [38].

Many nonlinear travelling-wave-interactions rely on phase-matching, e.g. frequency mixing and parametric amplification. However, there are also nonlinear processes which are intrinsically phase matched, regardless of dispersion, and thus no special experimental preparation is needed. Intensity dependent refractive index, multi-photon absorption, and stimulated Raman-scattering (SRS) are examples of such processes. In the following, the optical Kerr-effect and SRS will be discussed.

Using coupled mode-theory [39, 40], the following propagation equation for the pulse amplitude is obtained:

$$\left(i \frac{\partial}{\partial z} + \sum_{m \geq 2} \frac{i^m \beta^{(m)}}{m!} \frac{\partial^m}{\partial T^m} \right) A(z, T) \approx - \frac{\omega_0}{4\sqrt{N}} \left(1 + \frac{i}{\omega_0} \frac{\partial}{\partial t} \right) \iint dx dy e^{-i\beta_0 z} \mathbf{e}^*(x, y, \omega_0) \hat{\mathbf{P}}^{(3)}(\mathbf{r}, t), \quad (3.8)$$

3.3 Nonlinear effects

where $\hat{\mathbf{P}}^{(3)}(\mathbf{r}, t)$ is the slowly varying envelope amplitude of the third order polarization, $\mathbf{P}^{(3)}(\mathbf{r}, t) = \frac{1}{2}\hat{\mathbf{P}}^{(3)}(\mathbf{r}, t) e^{-i\omega_0 t} + c.c.$. In the following, expressions for the contributions from the optical Kerr-effect and SRS to $\hat{\mathbf{P}}^{(3)}$ will be provided.

3.3.1 Nonlinear refraction and self-phase modulation

Third order polarization

In the following, the electric field of the pulse is expressed as $\mathbf{E}(t) = \frac{1}{2}\hat{\mathbf{E}}(t) e^{-i\omega_0 t} + c.c.$, and according to Eq. (3.2), the envelope is given by

$$\hat{\mathbf{E}}(t) = \mathbf{e}(x, y, \omega_0) e^{i(\beta_0 z)} A(z, T) / \sqrt{N}. \quad (3.9)$$

The response of the Kerr-effect is instantaneous [34], and the Cartesian components of the vector of the slowly varying envelope $\hat{\mathbf{P}}^{(3)}$ are given by [38, 41]

$$\hat{P}_\mu^{(3)} = \varepsilon_0 \frac{1}{4} \chi_{xxxx}^{(3)} \left[2\hat{E}_\mu \left| \hat{\mathbf{E}} \right|^2 + \hat{E}_\mu^* \hat{\mathbf{E}}^2 \right], \quad (3.10)$$

where $\mu \in \{x, y, z\}$, and $\chi^{(3)}$ is the third-order susceptibility tensor (evaluated at ω_0). In general, this fourth-rank tensor has 81 components. However, because of the isotropy of the medium and laser wavelength being far from any resonance of the medium (i.e. Kleinmann symmetry holds), there is only one remaining element [38].

Suppose the light is linearly polarized in the x direction, $\hat{\mathbf{E}} = \hat{E} \hat{\mathbf{x}}$; $\hat{\mathbf{P}}^{(3)}(t)$ is then given by

$$\hat{\mathbf{P}}^{(3)}(t) = \varepsilon_0 \frac{3}{4} \chi_{xxxx}^{(3)} \left| \hat{E}(t) \right|^2 \hat{E}(t) \hat{\mathbf{x}}. \quad (3.11)$$

For left-hand (+) and right-hand (-) circularly polarized light, the Jones vector of the electric envelope is given by $\hat{\mathbf{E}} = \hat{E} \frac{1}{\sqrt{2}}(1, \pm i) = \hat{E} \mathbf{e}_\pm$; and $\hat{\mathbf{P}}^{(3)}(t)$ is then given by

$$\hat{\mathbf{P}}^{(3)}(t) = \varepsilon_0 \frac{2}{4} \chi_{xxxx}^{(3)} \left| \hat{E}(t) \right|^2 \hat{E}(t) \mathbf{e}_\pm. \quad (3.12)$$

Nonlinear refraction

Eqs. (3.11) and (3.12) show that the polarization state remains parallel to the electric field. It is worth noting that for elliptically polarized light this is not the case, and rotation of the polarization ellipse is a consequence [42]. Thus, for linearly and circularly polarized light, it is possible to define a scalar nonlinear susceptibility from which the intensity-dependent refractive index can be deduced [38]:

$$n = n_0 + n_2 I(t), \quad (3.13)$$

3.3 Nonlinear effects

where n_0 is the linear refractive index, n_2 denotes the nonlinear refraction coefficient, and $I(t)$ stands for the temporal intensity of the pulse. Eq. (3.13) describes the optical Kerr-effect. For linearly and circularly polarized light the nonlinear refraction coefficients are given by

$$n_{2,L} = \frac{3}{4} \frac{\text{Re}(\chi_{xxxx}^{(3)})}{\varepsilon_0 c n_0^2} \quad \text{and} \quad n_{2,C} = \frac{2}{4} \frac{\text{Re}(\chi_{xxxx}^{(3)})}{\varepsilon_0 c n_0^2}, \quad (3.14)$$

respectively. Thus, the ratio of $n_{2,C}$ to $n_{2,L}$ is 2/3 [41]. This difference constitutes the basic idea to reduce the Kerr-effect by using circularly instead of linearly polarized light. The value of the nonlinear refraction coefficient for fused silica at a wavelength of 1.06 μm is $n_2 \approx 3 \cdot 10^{-20} \text{ m}^2/\text{W}$ (state of polarization not specified) [34].

Generalized nonlinear Schrödinger equation

The propagation of a pulse under the influence of GVD and Kerr-effect can be described with the (generalized) nonlinear Schrödinger equation, which is obtained by inserting the expression for the nonlinear polarization, Eq. (3.11), in the pulse propagation equation (3.8) and using Eq. (3.9), as well as the expression for the normalization N:

$$\left(i \frac{\partial}{\partial z} + \sum_{m \geq 2} \frac{i^m \beta^{(m)}}{m!} \frac{\partial^m}{\partial T^m} \right) A(z, T) = -\gamma \left(1 + \frac{i}{\omega_0} \frac{\partial}{\partial t} \right) |A(z, T)|^2 A(z, T) + i \frac{g}{2} A(z, T), \quad (3.15)$$

where the nonlinearity parameter γ is defined as [34]

$$\gamma = \frac{\omega_0}{c} \frac{n_2}{A_{\text{eff}}}, \quad (3.16)$$

and A_{eff} is the effective mode-area [34]:

$$A_{\text{eff}} = \frac{\left(\iint_{\mathbb{R}^2} dx dy |\mathbf{e}(x, y, z, \omega_0)|^2 \right)^2}{\iint_{\mathbb{R}^2} dx dy |\mathbf{e}(x, y, z, \omega_0)|^4}. \quad (3.17)$$

The left side of Eq. (3.15) describes dispersion, and the time-derivative on the right side describes the self-steepening [34]. The strength of this effect is in the order of $\Delta\omega/\omega_0$, where $\Delta\omega$ is the spectral bandwidth. If the spectrum is narrow (which is given for all situations of this work), then self steepening can be neglected and the remaining term on the right side (without the gain term) describes the effect of self phase modulation. An exponential amplification term (with gain coefficient g) has also been included in Eq. (3.15), in principle, a more accurate description including gain saturation, gain dispersion, spectral gain characteristics and inversion is possible, e.g. see [30].

3.3 Nonlinear effects

To evaluate the impact of dispersive or nonlinear effects on the pulse evolution, characteristic length scales for dispersion (L_D) and a nonlinearity (L_{NL}) are introduced by

$$L_D = \frac{(\Delta T)^2}{|\beta^{(2)}|}, \quad L_{NL} = \frac{1}{\gamma P_0}, \quad (3.18)$$

and must be compared to the fiber length L . Where (ΔT) is a characteristic time scale of the pulse, e.g. the pulse duration or the inverse of the spectral bandwidth, and P_0 is related to the peak-power of the pulse. In the following, it is assumed that the higher order dispersion terms are small compared to the GVD term.

For example, if the fiber-length is such that $L \ll L_{NL}$ but $L \sim L_D$, then nonlinearity plays a minor role and the pulse evolution is governed by GVD, and the propagation can be described with Eq. (3.4).

In general, numerical methods, such as the split-step Fourier method [34], must be employed in order to grasp the complex pulse dynamics described by Eq. (3.15). However, there exist special classes of pulse-propagations [34]. For instance, in the anomalous dispersion regime (bright) solitons are solutions of the nonlinear Schrödinger equation (neglecting high order dispersion, gain and self-steepening) [43]. The condition for the generation of a fundamental soliton is $L_D = L_{NL}$. These extraordinary pulses propagate without any change of shape. Higher order solitons vary their shapes periodically with distance. Furthermore, in fiber amplifiers, the interplay of normal dispersion, SPM and gain can result in a self-similar propagation [44]. This is discussed in section 3.5.

Self-phase modulation

If the characteristic length scales are such that $L \ll L_D$ but $L \sim L_{NL}$, then the dispersion terms are negligible, and the pulse evolution is governed by self-phase modulation.

In general, the temporal phase of an optical signal can be modulated if the refractive index is modified on a timescale comparable to or faster than the timescale of the optical signal. Optical phase modulation can arise from gain or absorption, where the refractive index changes according to the Kramers-Kronig-relation. Alternatively, it can arise from the optical Kerr-effect, i.e. the intensity-dependence of the refractive index, see Eq. (3.13). If the refractive index is modified by a signal different to the one which is modulated, the effect is called cross-phase modulation [45]. Self-phase modulation takes place if the index is modified by the signal which experiences the modulation [34]:

$$A(z, t) = A(z = 0, t) \exp [i\gamma |A(z = 0, t)|^2 z]. \quad (3.19)$$

3.3 Nonlinear effects

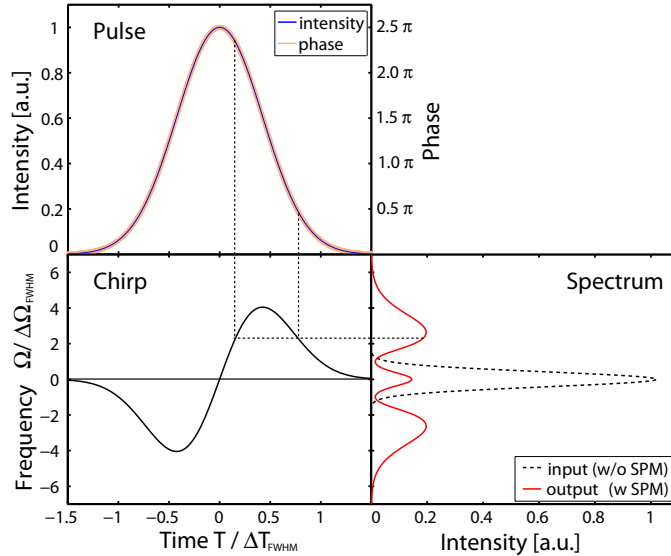


Figure 3.2: SPM-induced broadening of the spectrum for an initially unchirped Gaussian pulse. The maximum nonlinear phase-shift is 2.5π . The dotted lines show the relation of one frequency point to multiple time points.

Fig. 3.2 illustrates the impact of SPM on the spectrum for an initially unchirped pulse. The spectral modulations can be explained by interference of temporally delayed waves (at the same frequency) [46]. The delay between the waves affects the interference term. Conventionally, the B-integral is defined as a measure for the maximum possible magnitude of accumulated SPM during pulse propagation (e.g. in an amplifier) [21]:

$$B = n_2 \frac{\omega_0}{c} \int_0^L dz' \hat{I}(z') \approx \gamma \hat{P}_{in} L_{eff} = \gamma \hat{P}_{out} L_{eff}^* \quad (3.20)$$

where $\hat{I}(z)$ is the peak-intensity of the temporal pulse as a function of the z -position across the fiber, and L is the propagation length. If there is amplification or attenuation during pulse propagation, an effective length L_{eff} must be used instead of L . For an exponential amplification (with constant gain-coefficient g), the effective length is given by $L_{eff} = (\exp(gL) - 1)/g$. It is also common to define an effective length with respect to the output. For an exponential amplification, this is given by $L_{eff}^* = (1 - \exp(-gL))/g$. In general, a numerical simulation is required to estimate the B-integral. In particular, the signal growth across the fiber amplifier has to be calculated. For this reason, the model presented in section 2.3 must be extended by the pump process. A simple approach is described in [24].

Furthermore, in CPA-systems the B-integral can also be measured using model-based phase-shaping, as experimentally demonstrated in section 6.4.

3.4 Challenges of direct ultrashort pulse amplification

3.3.2 Stimulated Raman scattering

A second main class of nonlinear effects results from stimulated inelastic scattering. Molecular vibrations (oscillating at frequency ω_v), excited by the laser wave (at frequency ω), modulate the refractive index of the medium. Thus, frequency sidebands are impressed onto the laser field [41]. Optical phonons result in large frequency shifts ($\omega_v \sim 13$ THz in fused silica). The Stokes wave at $(\omega - \omega_v)$ can be beat with the laser field. This results in coherent excitation of molecular vibrations. The Stokes wave experiences gain. This process is called stimulated Raman scattering (SRS). Acoustic phonons cause a much smaller frequency shift (~ 17 GHz), and the effect is called stimulated Brillouin scattering (SBS). The spectrum of ultrashort pulses is significantly broader than the Brillouin gain bandwidth, and thus, the impact of SBS is negligible [34].

In contrast to the Kerr-effect, SRS is initiated at certain threshold intensity. Above this level, signal energy is rapidly frequency-converted to the Stokes wave. Thus, the Raman effect imposes a limitation on ultrashort pulse amplification in fibers.

Accurate determination of the SRS threshold requires numerical modelling, which must include the experimental Raman gain spectrum [34], and the zero-point quantum noise of the optical field [38]. It is worth mentioning that amplified spontaneous emission and parametric processes strongly affect the onset of SRS.

In the experiments described in this thesis SRS is not observed since LMA fibers of short length are employed. However, it is an issue for other fiber amplifiers, e.g. see [47].

3.4 Challenges of direct ultrashort pulse amplification

Nonlinear processes are much more effective in fibers than in bulk media. If the product of intensity and effective length ($I \cdot L_{eff}^*$) determines the influence of nonlinear effects, then the relative enhancement of nonlinear effects can be approximated by $\lambda L_{eff}^*/A_{eff}$, [34]. Therefore, the generation of high peak-power pulses with fiber-based amplification is challenging. In the following, some of the effects limiting the direct (i.e., unchirped) pulse amplification with fibers are identified and discussed.

Cumulative self-phase modulation represents one of the most dominant limitations. If the effective fiber length is such that $L_{eff}^* \geq L_{NL}$, SPM will result in broadening of the spectrum of an initially unchirped pulse. In Fig. 3.2, the impact of SPM on the spectrum has already been illustrated. This spectral broadening can be utilized for pulse-compression [46]. In this way, the peak-power can be scaled up to an order of magnitude before degradation of pulse-contrast arises. However, active fibers exhibit a certain gain bandwidth. Thus, the interplay of gain and SPM-induced spectral broadening will re-

3.5 Self-similar propagation and amplification

sult in strong spectral shaping of the original spectrum. This is particularly problematic for an amplifier chain, and contrasts the idea of amplification where the shape of the pulse and spectrum are approximately preserved. An broadband external compression is required to compensate for the chirp due to the nonlinear action. The output pulse-contrast is degraded due to side pulses, which originate from the SPM-process and high order dispersion during amplification or compression. Furthermore, small perturbations of the input pulse, e.g. in form of weak post-pulses, may increase due to parametric amplification. Despite these issues, peak-powers around 10 MW have been reported for the direct amplification using a rod-type PCF [48].

To avoid significant pulse distortions after direct amplification, the B-integral must remain below ~ 3 rad [21]. Using this value in Eq. (3.20), the output peak-powers are restricted to < 10 MW for state-of-the-art rod-type PCFs, and in the case of single-mode step-index fibers (core-size $\sim 15 \mu\text{m}$) to a few kW.

Damage of the fiber endfaces is a limitation. It is expressed in terms of fluence F_{damage} , for fused silica and spectral center wavelength $\lambda_0 \sim 1 \mu\text{m}$, it is given by [7]

$$F_{\text{damage}} = 22(\Delta\tau)^{0.4} \text{J/cm}^2, \quad (3.21)$$

where $\Delta\tau$ is the pulse-duration in nanoseconds. The formula is accurate for $\Delta\tau > 10$ ps, for pulse-durations ~ 1 ps the damage fluence is around 2 J/cm^2 . For ultrashort pulses, the extraction of stored energy is usually limited by this damage fluence threshold.

Damage of the fiber amplifier can be also due to Self-focusing, which is the spatial analogue of SPM [49]. It causes a damaging focus within the fiber. The critical peak-power is $\approx \lambda_0^2 / (8n_0n_2)$, where n_0 is the index of the core and λ_0 is the central wavelength.

3.5 Self-similar propagation and amplification

An attractive feature of self-similar propagation in normal-dispersion amplifiers is that it allows for highly nonlinear propagation, typically exhibiting B-integrals of tens of radians. The pulse evolves into an asymptotic parabolic pulse possessing a linear chirp [44, 50]. After the fiber output, this chirp can be efficiently compensated with a bulk grating compressor. Besides the fiber parameters (i.e., $\beta^{(2)}$, gain coefficient g , and γ), the amplitude and width of the so-called similaritons are only dependent on the energy of the initial pulse and not its specific shape. Using this concept, pulses with MWs of peak power have been generated from a step-index Yb-doped fiber-amplifier [47]. However, further peak-power scaling is limited by the available gain bandwidth of Ytterbium-doped fibers. Higher peak-powers can be produced using the technique of chirped-pulse amplification, which will be discussed in the following section.

3.6 Concepts to generate high peak-power pulses and their limitations

3.6.1 Chirped pulse amplification

The energy of a solid-state laser can be directly boosted via the resonator length or cavity dumping [51–53]. However, the key technique to produce high peak-power pulses is chirped pulse amplification (CPA), in which the low-energy signal pulse is stretched, amplified, and recompressed [54]. Fig. 3.3 illustrates such a master oscillator power amplifier (MOPA). The chirping of the pulse corresponds to a lowered peak-power which reduces cumulative nonlinear effects during amplification and also increases the damage threshold. To restore the original pulse-duration at the output of a linear CPA-system, the residual phase including all higher-order terms must be cancelled.

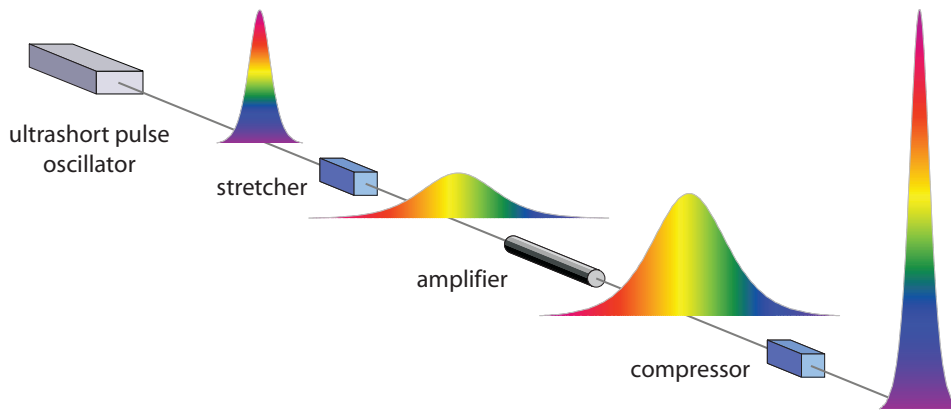


Figure 3.3: Schematic of the technique of chirped pulse amplification.

Monolithic stretchers/compressors

An all-fiber laser-system is a turn-key, ultra-stable, compact source, which is useful for many real-world applications. The integration of optical components in ns-pulse fiber systems is possible (see section 2.4). In fiber-based ultrashort pulse amplification, a stretcher and a compressor are additionally required. The incorporation of these components is challenging.

There have been several demonstrations of fiber-based CPA-systems employing chirped fiber Bragg-gratings (CFBG) as the stretching unit, e.g. [55]. However, the fiber-based compressors are prone to nonlinear effects (due to the small mode-areas), which preclude the generation of high peak-intensities. Air-core Photonic band-gap fibers can be used

3.6 Concepts to generate high peak-power pulses and their limitations

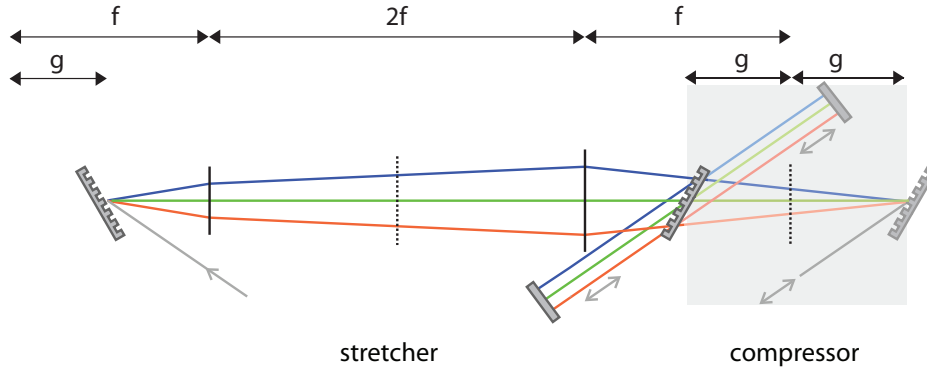


Figure 3.4: Schematic of a setup of a grating-based stretcher, and the corresponding compressor (grey background)

for compression. However, the dispersion is inherently related to loss, and exact phase-compensation is an issue. The pulse-energies from these all-fiber systems are restricted to the μJ -level. Chirped volume Bragg gratings (CVBG) exhibit larger apertures. Such compact fiber CPA-systems enable higher output pulse-energies [56]. However, currently available CVBGs are perturbed in phase and amplitude (due to the writing process). If nonlinear effects are present during amplification, the output pulse-quality is degraded. This will be experimentally demonstrated in section 6.1.

The combination of monolithic stretchers (e.g. fiber-stretchers, CFBGs) and diffraction-grating-based compressors allows for higher pulse-energies. Such a configuration still maintains a high degree of compactness and stability. However, exact phase-compensation requires matched CFBG-stretchers, which typically show small phase- and amplitude modulations. If nonlinear effects are present, degradation of pulse contrast is a consequence. This will be theoretically discussed in section 5.

Diffraction-grating-based stretchers/compressors

Phase-matching is easily accomplished when both the stretcher and compressor are set up with bulk diffraction gratings. Even if compactness and stability are sacrificed, such systems are interesting for a number of applications, e.g. material processing, as they deliver high average powers ($> 50 \text{ W}$) and high pulse-energies ($\sim 1 \text{ mJ}$). The generation of such high power levels requires dielectric gratings [57], which avoid thermal load and damage in the compressor, as well as deformation of the beam. In reflection those highly efficient gratings can handle kW of average-power.

The principles of grating-based stretching and compression are described in detail in [58–60]. Fig. 3.4 shows that the stretching is accomplished by the frequency-dependence

3.6 Concepts to generate high peak-power pulses and their limitations

of the path-lengths at the second grating of the stretcher. This grating-based stretcher produces an up-chirp. As can be seen in Fig. 3.4, the stretcher requires an imaging system [60]. However, lenses introduce additional dispersion, which cannot be compensated for by the compressor, therefore, reflective optics are required if the best compression is a goal. Real-world stretchers employ telescopes of the Newton- or Öffner-type, where the latter minimizes the aberrations inherent to the imaging system [61]. The compressor is less complex: it is a double passage through a grating-pair, as shown in Fig. 3.4. Dielectric gratings exhibit efficiencies close to 100% [57], and thus enable high compressor-efficiencies. The stretcher requires more optical elements, and thus shows a lower transmission. Therefore, up-chirped pulse amplification is advantageous in terms of efficiency. However, there also exist systems for which down-chirped pulse amplification is superior [62].

To reduce nonlinear effects during fiber-based chirped pulse amplification, strong stretching is required. The larger the stretching ratio the lower the influence of nonlinearity. This places several practical limitations. For example, a dielectric grating with a width of ~ 0.35 m is required to stretch the pulses to durations around 2 ns (if the full aperture is used). The production of this key element is not only very expensive, it also demands an optical substrate with a very good surface quality ($< \lambda/10$). Furthermore, the surface qualities of *all* optical elements must be excellent in order to avoid phase perturbations [63]. In spite of these issues a 2 ns pulse stretcher has been realized in our lab. Currently, durations of the stretched pulses around 2 ns are regarded as the frontier. Due to self-focussing, this corresponds to an ultimate pulse-energy ~ 8 mJ (however, the threshold for surface damage is usually much lower).

3.6.2 Large mode area fiber-amplifiers

Nonlinear effects are strongly influenced by the design of the fiber. In section 3.3.1 it has been shown that the amount of accumulated self-phase modulation is directly proportional to the effective length L_{eff} , and is inversely proportional to the effective mode area A_{eff} of the fiber-amplifier. Thus, the Kerr-effect can be reduced if the core of the fiber is enlarged and its effective length is shortened.

To improve the performance of fiber-amplifiers, the design and fabrication of novel active large mode area (LMA) fibers is a key subject. However, the design of practical LMA fibers is challenging: To achieve good beam quality and pulse quality at the output of the fiber amplifier, the laser radiation must propagate in form of a single mode inside the active fiber. The condition for fundamental mode operation is $V < 2.405$. To fulfill this special requirement for larger core-sizes, the numerical aperture (NA) of the fiber

3.6 Concepts to generate high peak-power pulses and their limitations

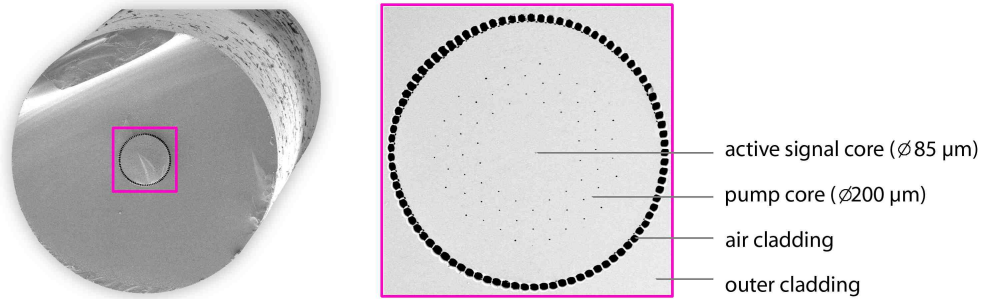


Figure 3.5: Electron microscope image of the entire endface of the rod-type waveguide (left), and a zoom into the micro-structured region (right).

must be decreased according to Eq. 2.1.

For conventional step index fibers, the step of the refractive index profile is controlled during the production process. Using techniques such as modified chemical vapour deposition (MCVD) or direct nanoparticle deposition (DND), the minimum refractive index step is $\sim 10^{-3}$, corresponding to core-diameters of about $15 \mu\text{m}$. Larger core-sizes of conventional step index fibers must employ methods to suppress higher order modes. These techniques include preferential gain management [64], mode filtering with differential bending losses [65] and built-in tapered fiber-sections [66]. In this way, assisted propagation of the fundamental mode was demonstrated in fibers with core-diameters up to $40 \mu\text{m}$ [67]. However, losses and mode-shrinking increase with larger core-sizes. In particular, the relative shrinking of the fundamental mode is the higher the larger the core [68]. This opposes the goal of a reduction of nonlinear effects [69].

A better control of the refractive index step between the doped core and cladding is achieved by a micro-structuring of the fiber cross-section. In particular, the effective index of the micro-structured cladding can be accurately adjusted by the hole-diameter and hole-to-hole pitch, e.g. [4]. For such a single pitch design, the maximum mode-field diameter of true single mode operation is around $30 \mu\text{m}$ because manufacturability and reproducibility of hole sizes are issues of the fiber-drawing process [70].

To permit larger areas of the (fundamental) mode, state-of-the-art LMA fibers are not strictly single-mode [71]. In the following, the so-called rod-type photonic crystal fiber (PCF) is presented [71]. It possesses a parameter $V \sim 3$. Currently, it is the state-of-the-art LMA fiber. This fiber will be used in some of the experimental systems. Some of the issues limiting the enlargement of mode area are discussed in the following. However, the evolution of practical LMA fibers is an ongoing research process, therefore, future developments are anticipated.

3.6 Concepts to generate high peak-power pulses and their limitations

Fig. 3.5 shows an electron microscope image of this rod-type PCF. It is a 19 missing-hole-design, which is realized by removing three inner 'circles' from the micro-structure of the cladding. The rod-type waveguide has an active core with a mean diameter of $85 \mu\text{m}$ and it is surrounded by three 'rings' of air-holes (pitch $\Lambda = 14.9 \mu\text{m}$, hole size $d = 0.1\Lambda$). The pump core has a diameter of $200 \mu\text{m}$ and is surrounded by an air-cladding (discussed below). The NA of the pump core is ~ 0.6 . The pump light absorption is 30 dB/m at 976 nm . Thus, only $\sim 1 \text{ m}$ of rod-length is required. The effective mode area of the fundamental mode is as large as $4000 \mu\text{m}^2$, i.e. about 100 times larger than that of a standard step index fiber. The outer diameter of the whole structure is 1.5 mm ; this rigid design is required since the weakly guiding rod-waveguide is ultra-sensitive to bending in terms of propagation loss and mode distortion.

It is worth noting that there is some degree of higher order mode suppression. In particular, the propagation losses of the modes depends on the relative hole size. The smaller the relative hole size d/Λ , the higher the loss for all modes. However, at common fiber-lengths of $\sim 1 \text{ m}$ efficient mode-discrimination is not possible. Moreover, a trade-off between the loss of the fundamental mode and the number of higher-order modes must be found.

Therefore, during amplification mode discrimination turns out to be the main challenge. In particular, the effect of spatial gain saturation is significant [72,73]. This drawback can be diminished by doping the central region of the core. In particular, it results in a higher gain for the fundamental mode, and thus in preferential gain management [64,74]. However, index matching during fiber-manufacturing is challenging. Furthermore, at the same doping level, a longer fiber-length is needed in order to produce a comparable output pulse-energy. In turn, this increases the efficiency of nonlinear effects and reduces the saturation energy. Higher doping levels are limited by the phenomenon of photo-darkening [17].

Besides the large mode areas, another advantage of the PCF technology is that the inner cladding can be encircled by a so-called air-cladding [75]. Allowing for a high NA of the pump-core (up to 0.8), the diameter of the pump-core can be decreased. Together with the larger signal core, this results in an improved overlap of the pump light with the doped area. This reduces the absorption length compared to conventional double clad fiber amplifiers. In this way, the effective length can be significantly decreased, and thus, nonlinear effects can be reduced. Furthermore, these fibers are ideally suited for high power operation since the radiation has no direct contact to the coating of the fiber.

4 Analysis of nonlinear chirped-pulse amplification

The technique of chirped-pulse amplification (CPA) significantly lowers the magnitude of SPM during amplification [54]. In fiber-based systems, the strength of SPM can be further reduced by using large mode-area (LMA) fibers [71]. Despite these methods, SPM arises in state-of-the-art fiber CPA-systems that produce sub-picosecond pulses with energies in the mJ range [76]. There are two major reasons. First, the stretching of the pulses is limited to factors of about 10^4 . Second, the size of the mode area of single mode fibers is limited. In the previous sections these limitations were discussed in detail. To further increase the pulse-energy of fiber-based CPA-systems, the pulse-amplification should allow for some degree of SPM.

In this chapter, an analytical model for nonlinear CPA-systems is derived. The key parameters that govern such systems are identified. This is followed by introduction of a figure of merit for the output pulse-quality. To compensate the impact of SPM on the chirped pulses, a first course of action is usually the adaptation of the compressor. The associated decrease of output pulse-quality with increasing B-integral will be discussed.

4.1 Analytical model for NLCPA

A model for nonlinear CPA-systems must quantitatively describe the three main stages: the stretching of the ultrashort pulses, the nonlinear propagation of these chirped pulses in the amplifier, and the compression of the amplified stretched pulses.

A numerical approach would model the stretching by using Eq. (3.4), the nonlinear amplification can be described by the generalized nonlinear Schrödinger equation (3.15), and the compression is described similarly to the stretching by employing Eq. (3.4). The description of the stretcher and compressor requires the spectral phases generated by these devices, e.g. in form of analytical expressions [58].

Numerical calculations are usually performed to obtain the final design of an experimental system. However, to specify design guidelines, an analytical model is helpful. In the following, such a model will be derived by making a few reasonable assumptions. The simple theoretical model rapidly predicts useful parameter configurations for optimization of femtosecond fiber amplifiers in the presence of SPM.

4.1 Analytical model for NLCPA

To obtain this analytical model, the main points are: (i) derivation of an analytical expression for the stretched pulse, then (ii), the nonlinear propagation is treated, where the impact of SPM on the stretched pulse is separated from the effect of dispersion. For strong stretching of the pulse, the magnitude of the stretching phase is substantially higher than the phase-shifts resulting from dispersion during amplification. Thus, the pulse-shape does not significantly change during the acquisition of SPM, which is proportional to the intensity of the pulse. Thus, the separation of the two effects is justifiable. In particular, at first, the nonlinear amplification is treated analytically without dispersion. (iii) The amplified pulse is expressed in the frequency-domain. (iv) The phase due to dispersion is added, and (v) the compression is described.

To derive an expression for the stretched pulse, the Fourier-integral of Eq. (3.4) must be analytically integrated using the method of stationary phase, e.g. [46]. To apply this method, the pulse must be transform limited. Furthermore, if a fiber stretcher is employed, then nonlinear effects should not occur during stretching. Another precondition is, that the third-order term of the stretching phase $\varphi_{st}(\Omega)$ has to be small compared to the magnitude of the second-order term, which is valid for most common stretchers. Typically, the ratios $\left| \phi_{st}^{(3)} \Delta\Omega / (3 \cdot \phi_{st}^{(2)}) \right|$ are in the order of 10^{-2} for bandwidths of a few THz. Thus, the third-order term can be neglected in the following analysis.

The method of stationary phase assumes that there are no significant contributions to the Fourier-integral from fast varying phase-terms with frequency, but only from the stationary points of the phase: $\left. \frac{d}{d\Omega} \left[\frac{\phi_{st}^{(2)}}{2} \Omega^2 - \Omega T \right] \right|_{\Omega_s} = 0$, which is equal to $\Omega_s = T / \phi_{st}^{(2)}$. Then, Eq. (3.4) can be approximated by

$$A_{st}(T) \approx \frac{1}{\sqrt{-i2\pi \left| \phi_{st}^{(2)} \right|}} \exp \left(-i \frac{T^2}{2\phi_{st}^{(2)}} \right) \tilde{A}_0 \left(\frac{T}{\phi_{st}^{(2)}} \right). \quad (4.1)$$

Where $\phi_{st}^{(2)}$ corresponds to the slope of the stretching chirp. The intensity-pulse is then given by $|A_{st}(T)|^2 \approx F^2 s \left(T / \phi_{st}^{(2)} \right) / (2\pi \left| \phi_{st}^{(2)} \right|)$, where the normalized power-spectrum is denoted by $s(\Omega)$ (the normalization is $\max[s(\Omega)] = 1$), and F is the peak of the spectral amplitudes. This means that the shape of a stretched pulse mimics the shape of the spectrum. Fig. 4.1 illustrates the mapping of the spectrum into the time-domain.

Due to the Kerr-effect, the pulse will acquire self-phase modulation during amplification [34]. The pulse propagation is determined by the interplay of dispersion, SPM and gain. However, the impact of dispersion can be neglected since the amount of phase, $\beta^{(2)} L (\Delta\Omega)^2 / 2$, is small for pulses with spectral bandwidths of a few THz in state-of-the-art rod-type waveguides of short length ($L \sim 1$ m) where $\beta^{(2)} = 25$ ps²/km (at a

4.1 Analytical model for NLCPA

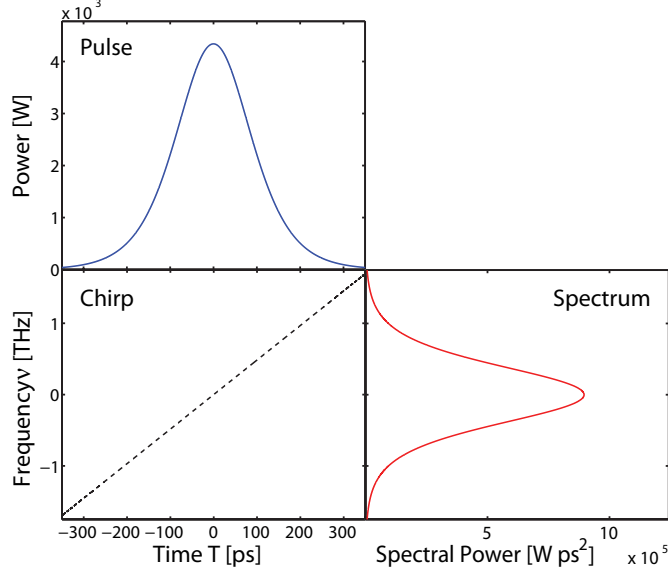


Figure 4.1: Stretching of the pulse, which corresponds to a mapping of the spectrum into the time-domain. The spectrum is of sech^2 -shape.

wavelength around $1 \mu\text{m}$) [44]. Furthermore, it is assumed that higher order dispersion, and other nonlinear effects, such as stimulated Raman scattering, are negligible. Thus, the amplification is dominated by SPM and can be expressed as

$$A_{amp}(T) \approx \sqrt{G} A_{st}(T) \exp(i\gamma L_{eff} |A_{st}(T)|^2) \stackrel{\text{Eq.(4.1)}}{=} \frac{\sqrt{G}}{\sqrt{-i2\pi |\phi_{st}^{(2)}|}} \exp(i\varphi(T)) \tilde{A}_0 \left(\frac{T}{\phi_{st}^{(2)}} \right) \quad (4.2)$$

The amplification is described by the energy-gain factor G . In all of the experiments, the pulses exhibit only small bandwidths and the gain can be considered spectrally uniform. Once the impact of the finite gain bandwidth on the spectrum is noticeable, the behavior of the CPA-system is too complicated to be handled with a simple model. In this case, calculations must employ the generalized nonlinear Schrödinger equation including the gain dynamics, e.g. [30]. For a spectrally uniform exponential gain, $G = \exp(gL)$, the effective length is given by $L_{eff} = (\exp(gL) - 1)/g$. The temporal phase is given by $\varphi(T) = -T^2/(2\phi_{st}^{(2)}) + B \cdot s \left(T/\phi_{st}^{(2)} \right)$. The phase consists of one part due to stretching, $-T^2/(2\phi_{st}^{(2)})$ and the SPM term, where the B-integral is given by:

$$B = \gamma L_{eff} \max[|A_{st}(T)|^2] = \gamma L_{eff} F^2 / (2\pi |\phi_{st}^{(2)}|). \quad (4.3)$$

4.1 Analytical model for NLCPA

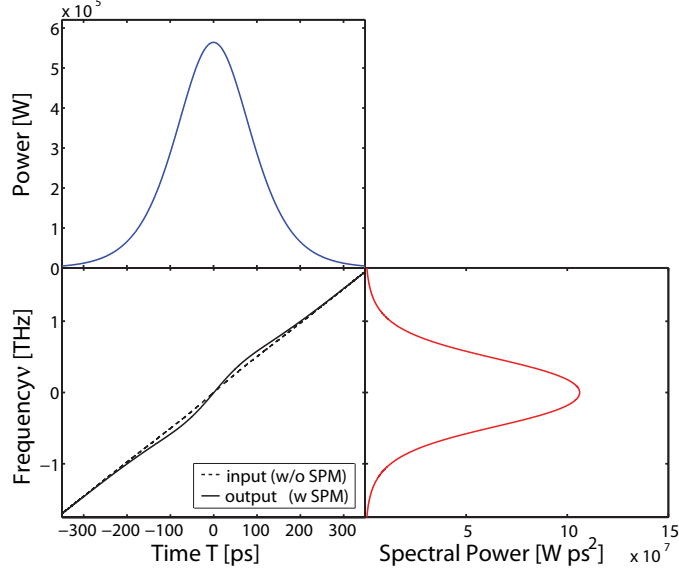


Figure 4.2: Influence of self-phase modulation on the chirp of the stretched pulse. The initial spectrum is of sech^2 -shape. The B-integral of the nonlinear propagation is $B = 20$ rad. To highlight the deviation from the linear (stretching) chirp, the difference is multiplied by 10.

To add dispersion and to describe the compression of the pulses, the amplified pulse must be expressed in the frequency-domain, i.e. a Fourier-transform is necessary:

$$\tilde{A}_{amp}(\Omega) \approx \frac{\sqrt{G}}{\sqrt{-i2\pi |\phi_{st}^{(2)}|}} \int dT \exp(i\Omega T) \exp(i\varphi(T)) \tilde{A}_0\left(\frac{T}{\phi_{st}^{(2)}}\right). \quad (4.4)$$

The method of stationary phase is used to evaluate the Fourier-integral. The stationary points must fulfil the condition: $\left. \frac{d}{dT} [\Omega T + \varphi(T)] \right|_{T_s} = 0$ which is equal to

$$\Omega = T_s / \phi_{st}^{(2)} - B \cdot ds(T / \phi_{st}^{(2)}) / dT \Big|_{T_s}. \quad (4.5)$$

In the case of smooth initial spectra and strong stretching, the chirp still corresponds to approximately linear one-to-one mapping between time and frequency, and the term $-B \cdot ds(T / \phi_{st}^{(2)}) / dT \Big|_{T_s}$ can be neglected. The stationary points are given by $T = \phi_{st}^{(2)} \Omega$, and the complex spectral amplitude can be approximated as

$$\tilde{A}_{amp}(\Omega) \approx \sqrt{G} \tilde{A}_0(\Omega) \exp\left(i \frac{\phi_{st}^{(2)}}{2} \Omega^2\right) \exp(iB s(\Omega)). \quad (4.6)$$

This expression reveals a key result: the shape of the spectral phase due to SPM is determined by the shape of the (normalized) spectrum and has the magnitude of the

4.1 Analytical model for NLCPA

B-integral value. It must be stressed that the Kerr-effect is usually described with the intensity-dependent refractive index in the time-domain, however, Eq. (4.6) describes the resulting impact in the frequency-domain.

Eq. (4.6) is based on the assumption that the accumulated SPM does not cause significant spectral broadening. The change of the spectrum can be determined by using the expression for the new instantaneous frequencies Ω_{out} , Eq. (4.5), where the input frequencies are $\Omega_{in} = T/\phi_{st}^{(2)}$. An approximate expression is then given by $\Omega_{out} = \Omega - \frac{B}{\phi_{st}^{(2)}}s'(\Omega)$. A linear expansion of $s'(\Omega)$ around the central frequency $\Omega = 0$ yields $s'(\Omega) = const - |s''(0)| \cdot \Omega + \dots$, and the relative broadening is estimated as follows

$$\frac{\Delta\Omega_{out} - \Delta\Omega_{in}}{\Delta\Omega_{in}} = \frac{B}{\phi_{st}^{(2)}} |s''(0)| \propto \frac{B}{\phi_{st}^{(2)}(\Delta\Omega_{in})^2}, \quad (4.7)$$

where it is assumed that the spectrum s is a function of the ratio $(\Omega/\Delta\Omega_{in})$. The amount of broadening is dependent on the ratio of the B-integral value to the magnitude of stretching phase, which typically exhibits values of a few hundred radians. Thus, the spectrum remains almost the same, consequently, Eq. 4.6 can be applied.

It must be stressed that in the cases of non-smooth spectra [77, 78], initial phase ripples [79], Eq. (4.6) is not applicable. The influence of these perturbations is discussed in more detail in chapter 5. Furthermore, it is also not valid for weak stretching of the pulses [80]. In particular, in this cases the term $-B \cdot ds(T/\phi_{st}^{(2)})/dT \Big|_{T_s}$ results in a multiple-point-to-point configuration for the chirp.

As mentioned in the beginning of this section, in the case of strong stretching, the impact of Kerr-nonlinearity can be separated from the effect of dispersion. A small amount of dispersion can be introduced in Eq. (4.6) by multiplication with the term $\exp(i\varphi_{disp}(\Omega))$. To describe the spectral phase at the output of the system, the phase of the compressor, φ_{co} , must also be added. Since the phases imposed by the stretcher ($\varphi_{st} = \phi_{st}^{(2)}\Omega^2/2$) and the compressor are also a result of dispersion, all the phase-contributions can be cast into a single parameter for simplicity

$$\varphi_D = \varphi_{st} + \varphi_{disp} + \varphi_{co}. \quad (4.8)$$

After the compressor the amplitude of the output pulse is given by

$$A_{out}(T) \approx \sqrt{GF} \int \frac{d\Omega}{2\pi} \exp(-i\Omega T) \sqrt{s(\Omega)} \exp(i[\varphi_D + B s(\Omega)]), \quad (4.9)$$

since the pulse is transform-limited at the input of the system, it is written as $\tilde{A}_0(\Omega) = F\sqrt{s(\Omega)}$. Eq. (4.9) reveals the key parameters of a nonlinear CPA-system: at a given energy level, the output peak-power, $\hat{P}_{out} = \max |A_{out}(T)|^2$, is only dependent on the

4.2 Evaluation of the pulse quality

shape of the spectrum $s(\Omega)$, the B-integral and the total phase due to dispersion, φ_D . It is worth noting that an expression similar to Eq. (4.9) has already been given in Ref. [81] but without derivation. Here, this key result has been analytically deduced, and all approximations have been highlighted.

4.2 Evaluation of the pulse quality

The output pulse-quality can be measured using the Strehl-ratio, which is the ratio of the output peak-power to the peak-power of the transform-limit [82]

$$S = \frac{\hat{P}_{out}(s, B, \varphi_D)}{\hat{P}_{out}(s, 0, 0)}. \quad (4.10)$$

In this thesis this quantity is also denoted as relative peak power. Furthermore, the phrase 'best compression' refers to the highest Strehl-ratio (if not specified otherwise). To achieve best compression, the Fourier-transform of Eq. (4.9) must be numerically evaluated. Compared to a full numerical approach, the advantage of the analytical model is, that the stretching and the compression do not have to be explicitly modelled. In particular, only the sum of the spectral phase-terms is important. To find the point of best compression, φ_D may be replaced by a single parabolic phase with variable magnitude. The analytical model permits a fast calculation, which is advantageous if many design-parameters are varied.

4.3 Partial compensation of SPM using the compressor

The action of SPM causes the phase-term $B \cdot s(\Omega)$ at the output of the amplifier of the nonlinear CPA-system. To produce (nearly) transform-limited pulses at the output of the entire CPA-system, this spectral phase must be compensated. In particular, a compensation requires positive dispersion. This can be shown by a Taylor-expansion of the term $B \cdot s(\Omega)$:

$$B \cdot s(\Omega) = B \cdot [s^{(0)} + s^{(1)}\Omega + s^{(2)}\Omega^2/2 + \text{higher-order terms}]. \quad (4.11)$$

For standard spectral shapes, such as sech^2 or Gauss, the coefficient $s^{(2)}$ is negative, and thus, positive dispersion is demanded. Furthermore, it can be seen that the higher order terms will prevent perfect phase compensation. The associated residual phase causes a degradation of pulse quality. This will be discussed in the following.

Emphasis is placed on CPA-systems that employ LMA-fiber-amplifiers. Because of the short lengths (~ 1 m) of these amplifiers, dispersion is negligible (for pulse durations > 100 fs). To partially compensate SPM, positive dispersion is produced by the stretcher-

4.3 Partial compensation of SPM using the compressor

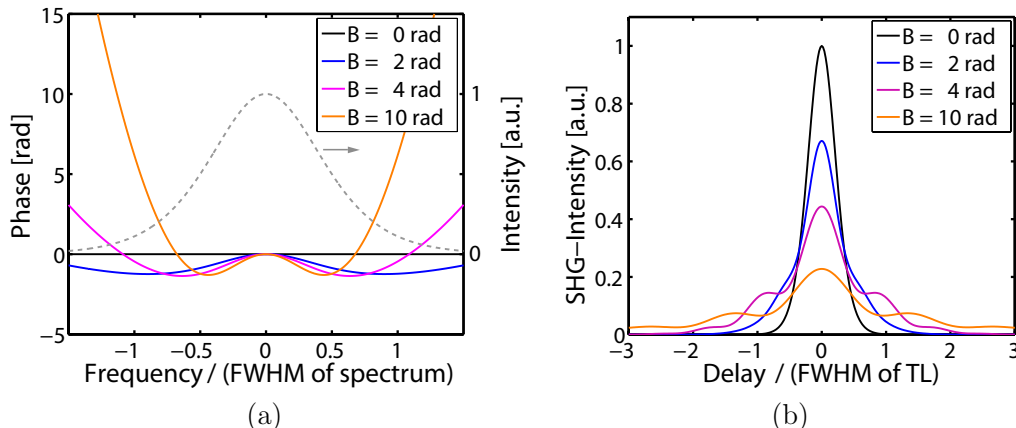


Figure 4.3: (a) Simulation of the residual spectral phase at the output of a nonlinear CPA-system for different B-integrals. The phase is shown at the point of best compression (i.e. highest Strehl-ratio). The input is a transform-limited sech^2 -pulse; (b) corresponding autocorrelations. Delay measured in units of the FWHM at the transform-limit (TL).

compressor mismatch. In the following, it is assumed that the contribution of TOD is negligible. The phase is approximated by a parabolic term, $\varphi_D = \left[\phi_{st}^{(2)} + \phi_{co}^{(2)} \right] \Omega^2 / 2$, with the sign of ϕ_{st} being opposite to ϕ_{co} . Since the second derivative of the spectral shape, $s^{(2)}$, is negative for standard shapes, the compensation of SPM requires a positive value for $\Delta\phi^{(2)} = \left[\phi_{st}^{(2)} + \phi_{co}^{(2)} \right]$. Thus, for the common case of up-chirped pulse amplification, the magnitude of the compressor phase has to be reduced. Using Eq. (4.9), the output pulse of the CPA-system is now described by

$$A_{out}(T) = \sqrt{GF} \int \frac{d\Omega}{2\pi} \exp(-i\Omega T) \sqrt{s(\Omega)} \exp\left(i \left[\frac{\Delta\phi^{(2)}\Omega^2}{2} + B \cdot s(\Omega) \right] \right). \quad (4.12)$$

For a given spectral shape $s(\Omega)$ and B-integral, the parameter $\Delta\phi^{(2)}$ is varied to achieve the best compression. In this way, the residual spectral phase at the output of a real world nonlinear CPA-system can be simulated. It must be emphasized that the compensation does not imply a simple cancellation of the parabolic term of the phase $B \cdot s(\Omega)$ since (according to Eq. (4.12)) the residual phase at the output has to be weighted with the spectral amplitudes. Fig. 4.3(a) shows that over-compensation with parabolic phase-terms results in the highest peak-power. The initial spectrum exhibits a sech^2 -shape, which describes the signal generated by a mode-locked oscillator of soliton-type. It can be seen that the compensation of $B \cdot s(\Omega)$ with the parabolic phase due to the stretcher-compressor-mismatch is the best in the center of the spectrum. However, the higher the B-integral, the higher the phase-shifts at the edges of the spectrum. This discovery has led to an experimental method improving the pulse-quality of a NLCPA by choosing the right spectral window of the stretcher, see section 6.1.

4.3 Partial compensation of SPM using the compressor

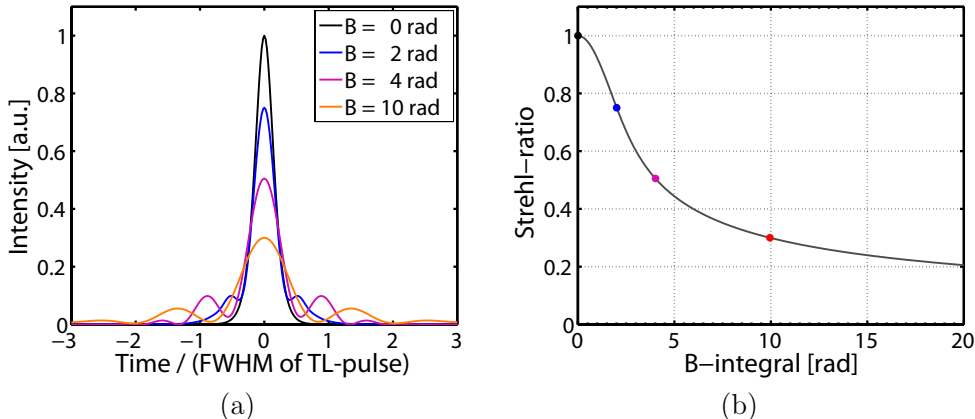


Figure 4.4: (a) Simulation of the best-compressed pulse at the output of the CPA-system for different B-integrals. The time is normalized to the full-width at half maximum (FWHM) of the transform-limited (TL) sech^2 -pulse. (b) Decrease in performance of a NLCPA: Strehl-ratio (at best compression) versus B-integral. The markers highlight the examples shown in (a).

The residual spectral phase corresponds to temporal shifts, which cause temporal spreading of the pulse. In Fig. 4.4(a) the best recompressed pulse is shown for different B-integral values. In practice, different B-integrals correspond to different output pulse-energies, however, the Strehl-ratio (i.e. normalized peak-power) is applied in order to evaluate the impact of nonlinearity on the quality of the output pulse. Due to the temporal spread of energy at higher B-integrals, this effective peak-power decreases as a function of the B-integral. This behavior is shown in Fig. 4.4(b). Experimentally, the decrease of pulse-quality is usually observed with an autocorrelator, therefore, Fig. 4.3(b) shows the corresponding degradation of the autocorrelation.

To summarize, the impact of SPM on a strongly stretched pulse can be approximated by a spectral phase, which exhibits a profile very similar to the spectral shape and a maximum phase-shift according to the B-integral. Compensation of SPM requires positive dispersion. This is a new insight into the nonlinear propagation of chirped pulses. It is worth noting that negative dispersion is usually associated with the cancelation of SPM for nearly transform-limited pulses. An adaptation of the compressor allows only partial compensation of the SPM accumulated by the chirped pulses. Having introduced the Strehl-ratio as a measure for the pulse-quality, it could be shown that the relative peak power decreases with increasing B-integral. This is in accord with previous findings, e.g. [83], stating that modest values of accumulated nonlinear phase, $B \sim 1$ rad, limit the achievable peak-power and pulse-contrast. Moreover, the analysis paves the way for the design of novel methods to control the impact of SPM in CPA-systems. Before this topic is addressed, the influence of perturbations will be discussed in the next chapter.

5 Stability analysis of nonlinear CPA-systems

In the preceding chapter ideal pulses have been considered. However, most real pulses show at least one of the two main kinds of perturbations: spectral amplitude-modulations and spectral phase-modulations. As will be shown in the following, these lead to a degradation of the pulse-contrast at the output of nonlinear CPA-systems.

The case of a spectral amplitude-modulation is illustrated in the first row of Fig. 5.1. This distortion may be caused by a double internal reflection in any optical component before the amplifier. In turn, this creates a post-pulse that follows the main pulse. Correspondingly, the spectrum shows spectral interference. These modulations will be superimposed on the envelope of the stretched pulse, too. During the nonlinear propagation in the amplifier of the CPA-system, the stretched pulse acquires self-phase modulation due to the intensity-dependence of the refractive index. Thus, the intensity modulation also results in a temporal phase-modulation. Ultimately, this phase-modulation causes a splitting of the pulse. The spatial analogue of this process is the diffraction of a beam by a phase-grating. The lower the initial pulse-contrast and the higher the B-integral of the nonlinear amplifier, the lower the pulse-contrast at the output of the nonlinear CPA-system [77, 78].

The second type of perturbation is an initial spectral phase-modulation. To study this case, a sinusoidal phase is considered for simplicity. In the second row of Fig. 5.1, it is shown that a sinusoidal spectral phase-modulation and a smooth power-spectrum result in multiple pulses in the time-domain. Theoretically, the number is infinite, however, only a few orders are relevant as the magnitude of the side pulses depends on the depth of the phase-modulation which is small. The stretched pulse also shows intensity modulations [84]. As in the previous case, due to the Kerr-effect, this modulation results in a temporal phase-grating and in an ultimate splitting of the pulse. With increasing B-integral, the modulation depth of the temporal phase-grating rises, and thus, a larger amount of pulse-energy is transferred into the side-pulses. In addition to the B-integral, the efficiency of this process is determined by the depth and period of the initial spectral phase-modulation, and the strength of the stretching chirp [79].

The two types of modulations differ regarding the impact of the stretching process on the shape of the stretched pulse. However, any modulation superimposed onto the stretched pulse will cause a pulse-degradation at the output of the CPA-system.

5 Stability analysis of nonlinear CPA-systems

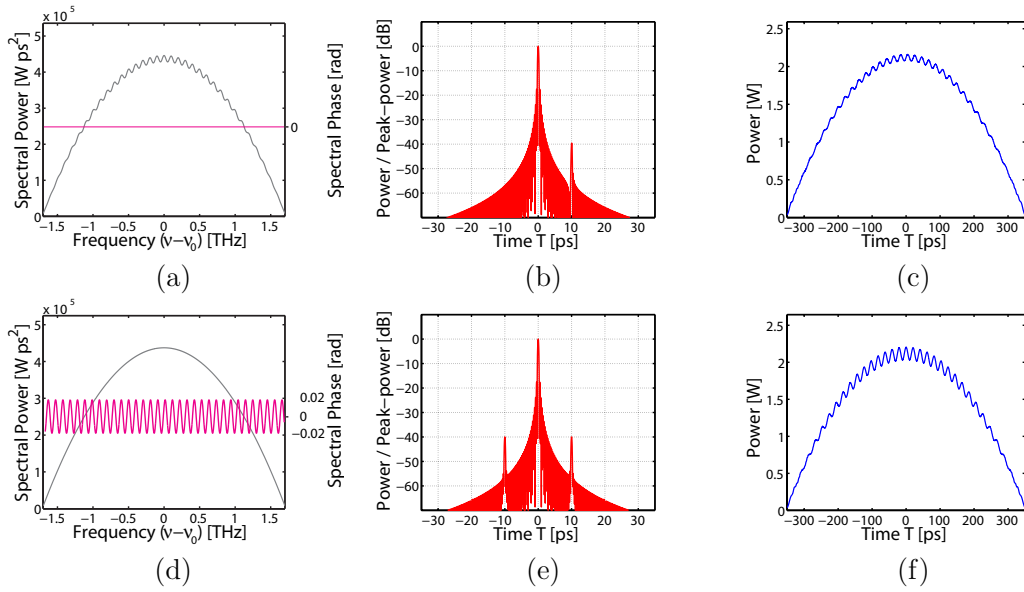


Figure 5.1: (a) Spectral amplitude-modulation, which is due to a post pulse that follows the main pulse (b). The contrast is 40 dB and the delay is 10 ps. (c): The modulated stretched pulse, (d) Spectral phase-modulation, i.e. a smooth intensity spectrum with a weak sinusoidal spectral phase-modulation (modulation depth is $d=0.02$, spectral modulation frequency is 10 ps), (e) this corresponds to a transform-limited multi-pulse in the time-domain, with (f) a modulated pulse in the stretched state

This chapter is organized as follows. In the first section the influence of weak post-pulses on the pulse-contrast at the output of nonlinear CPA-systems is discussed. These theoretical considerations are motivated by the experimental observation of distorted spectra at the output of nonlinear amplifiers. Then, the degradation of the pulse-contrast in the time-domain is analyzed in detail, concluding that this degradation manifests itself in the generation of pre- and post pulses. The focus of the analysis is placed on obtaining analytical results, as they are quite valuable for the design of practical systems. In particular, the build-up of the side pulses can be described by simple formulas. These expressions allow for an accurate estimation of the degradation of the pulse-contrast. Specifically, the relative intensities and temporal delays of the side pulses can be determined. The final section describes the impact of an initial phase-modulation on the performance of nonlinear CPA-systems. As the analysis is quite similar to the case of a spectral amplitude perturbation, emphasis is placed on the presentation of simple analytical results estimating the degradation of pulse-contrast.

5.1 Influence of a weak post-pulse

5.1.1 Experimental observation of spectral distortions

Nonlinear fiber-based CPA-systems running at B-integrals of tens of radians, e.g. [85], typically show an enhancement of any weak spectral modulation superimposed on the envelope of the input spectrum. The spectrum at the output of the nonlinear amplifier shows the same modulation-period, but the ripples are more pronounced the higher the output power.

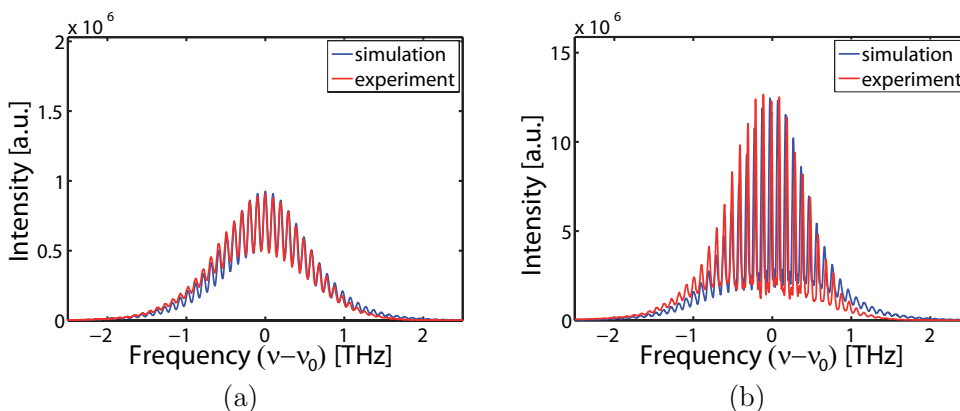


Figure 5.2: (a) Experimental and simulated spectrum of the superposition of a pulse and a weak post-pulse, (b) spectra after nonlinear amplification ($B = 3$ rad).

To identify the reason for this observation, a well-defined spectral modulation was intentionally produced. A post-pulse was generated by a double reflection in a glass plate, which was placed in between the oscillator and the stretcher of the CPA-system. Fig. 5.2(a) shows the experimental spectrum (red curve), and the corresponding numerical simulation (blue curve). The delay of the post-pulse is about 10 ps and the ratio of post to main pulse is about 2.2%. The pulse is stretched to about 170 ps in an optical fiber (without any impact of SPM), and is then amplified in an Ytterbium-doped fiber. During amplification, the pulse acquires SPM. The B-integral is about 3 rad. Fig. 5.2(b) shows that the output spectrum is distorted. The simulation of the amplification only includes the Kerr-effect and an exponential energy-growth, and in spite of this, it is able to accurately predict the output of the system. Therefore, the Kerr-effect is identified as the main cause for the enhancement of the modulations. A similar behavior is observed without the glass plate, i.e. operating the amplifier with the master oscillator's inherent pulse-contrast and at higher B-integrals.

5.1 Influence of a weak post-pulse

5.1.2 Analysis of pulse-contrast degradation

In the following, the degradation of pulse-contrast is shown to be the main issue of a more general distortion mechanism. This includes the identification of the key parameters being responsible for the pulse-contrast degradation. The analysis aims to provide analytical results, as they are quite valuable for the design of practical systems.

The superposition of the amplitudes of the main-pulse and the post-pulse is given by

$$A_{in} = A_0(T) + \sqrt{r}A_0(T - \Delta t), \quad (5.1)$$

where the temporal delay and the intensity ratio of the post pulse are denoted, respectively, by Δt and r . The spectrum shows spectral interference in the form of

$$\left| \tilde{A}_0(\Omega) + \sqrt{r}\tilde{A}_0(\Omega) \exp(i\Omega\Delta t) \right|^2 = F^2 s(\Omega) [1 + r + 2\sqrt{r} \cos(\Omega\Delta t)]. \quad (5.2)$$

Where $s(\Omega)$ is the normalized spectrum of the main pulse, $|\int dT \exp(i\Omega T)A_0(T)|^2 / F^2$. And F is the peak of the spectral amplitude. The delay Δt can be regarded as a spectral modulation frequency. Fig. 5.3 shows the joint time-frequency representation of the stretched state of the main pulse and its weak post pulse. In Fig. 5.3(c), the spectral interference can be seen. A weak side-pulse causes a strong modulation in the spectrum. In Fig. 5.3(c), the peak-to-valley modulation of the spectrum is about 4%, which corresponds to a 40 dB intensity-contrast in the main- to the post-pulse.

The stretched state of the main pulse and its weak post-pulse is given by

$$A_{st}(T) = \int \frac{d\Omega}{2\pi} \exp(-i\Omega T) \exp\left(i\frac{\phi^{(2)}}{2}\Omega^2\right) \left[\tilde{A}_0(\Omega) + \sqrt{r}\tilde{A}_0(\Omega) \exp(i\Omega\Delta t) \right], \quad (5.3)$$

where $\phi^{(2)}$ is the slope of the stretching chirp, Ω is the instantaneous angular frequency ($\Omega = \omega - \omega_0$), and T is the time in a reference frame moving at the group velocity (evaluated at $\omega = \omega_0$). The third-order dispersion during the stretching process has little impact, and is neglected. In this way, simple analytical expressions can reveal the key mechanisms at work. The analytical integration of Eq. (5.3) uses the method of stationary phase [46]. It is assumed that fast variations of the spectral phase do not contribute to the Fourier-integral, thus, only the stationary points of the phase are relevant. Therefore, Eq. (5.3) can be written as

$$A_{st}(T) = \frac{F}{\sqrt{-i2\pi\phi^{(2)}}} \left[e^{-i\frac{T^2}{2\phi^{(2)}}} \sqrt{s\left(\frac{T}{\phi^{(2)}}\right)} + \sqrt{r}e^{-i\frac{(T-\Delta t)^2}{2\phi^{(2)}}} \sqrt{s\left(\frac{T-\Delta t}{\phi^{(2)}}\right)} \right]. \quad (5.4)$$

5.1 Influence of a weak post-pulse

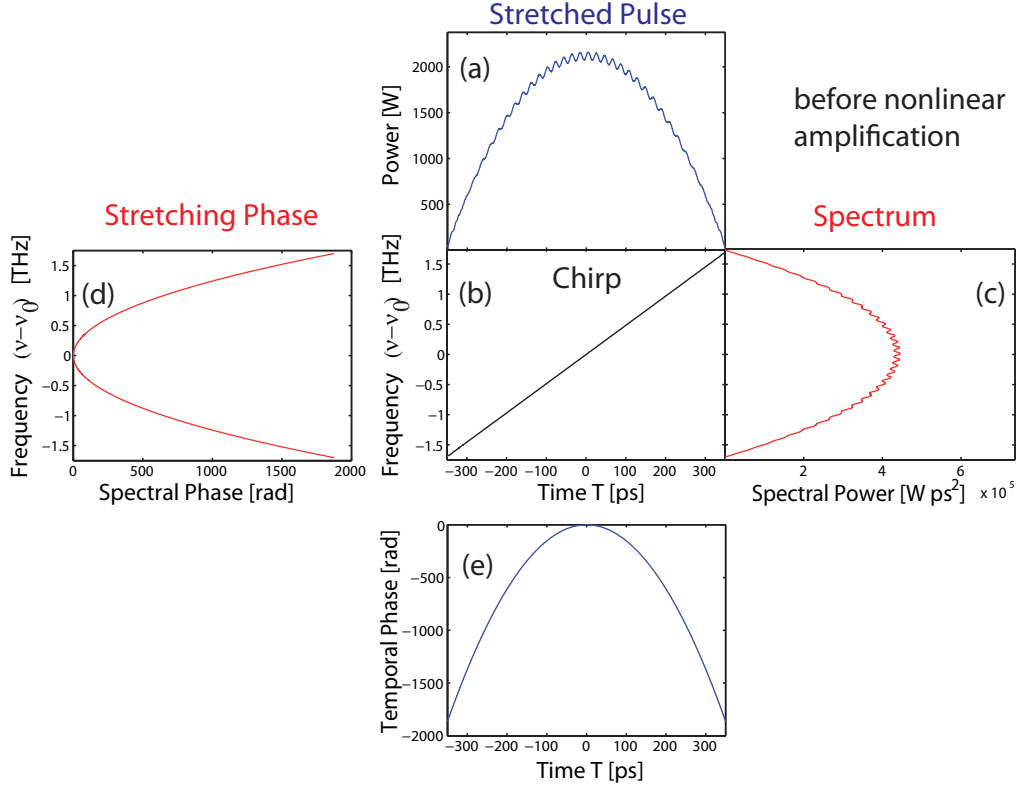


Figure 5.3: Stretched state prior to nonlinear amplification: (a) the stretched pulse with 500 ps FWHM. (b) the linear stretching chirp maps the spectrum into time-domain, (c) the (parabolic) spectrum. The spectral modulations have a frequency of $\Delta t = 10$ ps. (d) parabolic spectral phase, and (e) parabolic spectral phase corresponding to the linear chirp. The state after nonlinear amplification is shown in Fig. 5.4.

To evaluate the impact of the Kerr-effect, the intensity must be calculated:

$$|A_{st}(T)|^2 = \frac{F^2}{2\pi\phi^{(2)}} \left[s \left(\frac{T}{\phi^{(2)}} \right) + rs \left(\frac{T - \Delta t}{\phi^{(2)}} \right) + 2\sqrt{rs \left(\frac{T}{\phi^{(2)}} \right) s \left(\frac{T - \Delta t}{\phi^{(2)}} \right) \cos \left(\frac{T\Delta t}{\phi^{(2)}} - \frac{(\Delta t)^2}{2\phi^{(2)}} \right)} \right]. \quad (5.5)$$

This analytical description agrees with the numerical result shown in Fig. 5.3(a). The stretched pulse mimics the shape of the spectrum. The linear relation between frequency and time is also evident from the linear chirp that is shown in Fig. 5.3(b). The chirp is the temporal evolution of the instantaneous frequency (i.e., the difference of frequency and carrier frequency). The corresponding parabolic stretching phases in time and frequency-domain are plotted in Fig. 5.3(d) and (e), respectively.

5.1 Influence of a weak post-pulse

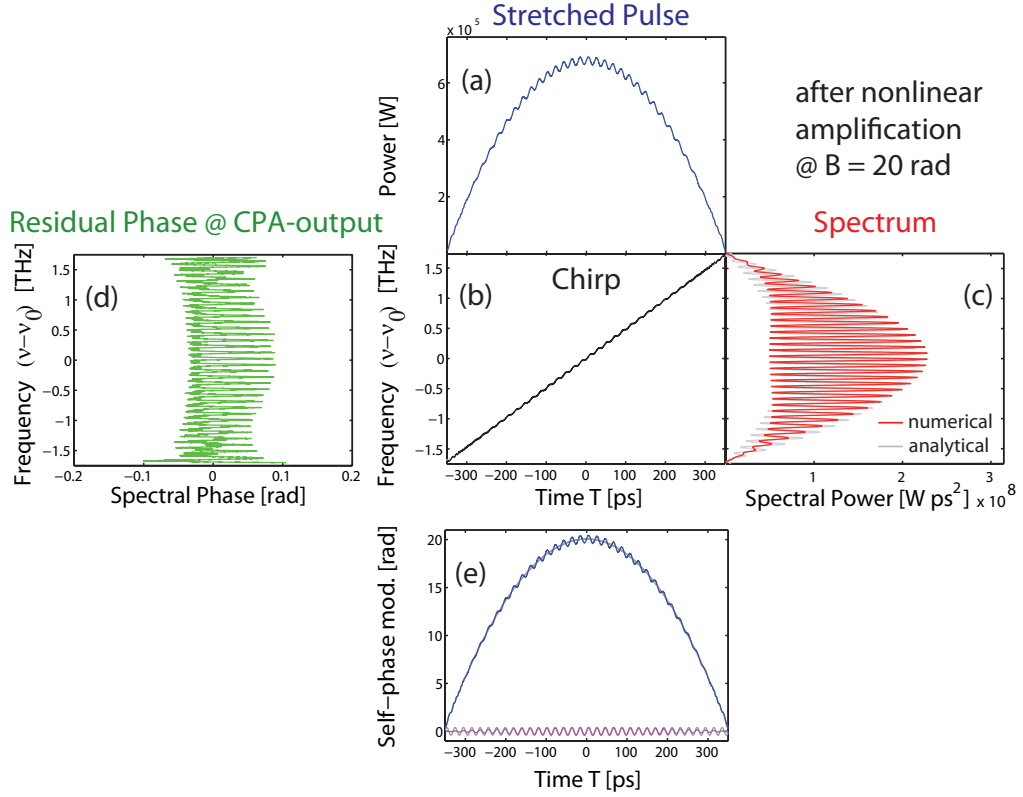


Figure 5.4: State at the output of the nonlinear amplifier when starting with the input shown in Fig. 5.3: (a) stretched pulse. (b) chirp with modulations due to SPM, (c) spectrum. (d) residual non-parabolic spectral phase at the output of the CPA-system due to the nonlinear action. (e) self-phase modulation (blue curve) which adds onto the existing stretching phase shown in Fig. 5.3(e), and its non-parabolic part (magenta curve).

Eq. (5.5) can be simplified when the temporal broadening is large compared to the delay of the post pulse, $\phi^{(2)}\Delta\Omega > \Delta t$ (where $\Delta\Omega$ is the bandwidth of the spectrum). Then, the term $[s(T/\phi^{(2)})s((T - \Delta t)/\phi^{(2)})]^{1/2}$ can be replaced by $s(T/\phi^{(2)})$. It is also assumed that the spectrum $s(\Omega)$ is slowly varying.

As already pointed out, because of the Kerr-effect during the nonlinear amplification, the stretched pulse will acquire a temporal phase which is proportional to the intensity. The amplified stretched pulse is given by

$$A_{amp}(T) = A_{st}(T) \sqrt{G} \exp(i\gamma L_{eff} |A_{st}(T)|^2). \quad (5.6)$$

If the growth of signal intensity along the gain-medium is approximately exponential ($G \approx \exp(gL)$), then the effective length of the amplifier is given by $L_{eff} =$

5.1 Influence of a weak post-pulse

$(\exp(gL) - 1)/g$, where the gain-coefficient, g , is assumed to be spectrally uniform. The fiber nonlinearity parameter is labeled γ (see Eq. 3.16). With these parameters the B-integral of the nonlinear amplifier can be expressed as in Eq. (4.3), under the assumption, that the peak-power of the main pulse is much higher than that of the post-pulse. Dispersion was neglected in Eq. (5.6). This assumption is reasonable since the length of the main-amplifier of a practical high-energy fiber CPA-system is such that $L < L_D$. According to Eq. (5.6), the intensity modulations superimposed onto the envelope of the pulse are transferred to the temporal phase. This is shown in Fig. 5.4(e). It can be seen that the total temporal phase consists of the stretching phase, $-T^2/(2\phi^{(2)})$, and the phase contribution due to SPM. In Fig. 5.4(e), the blue curve corresponds to the nonlinear phase-term only. The total phase is not shown since the magnitude of the stretching phase is substantially higher than the magnitude of the nonlinear phase (20 rad for the example shown).

To discriminate between the effects induced by the envelope and the modulations superimposed onto it, a parabolic envelope is used in Fig. 5.3 and Fig. 5.4. In particular, the nonlinear propagation of the parabolic envelope results in a linear contribution adding to the linear stretching chirp, Fig. 5.4(b), which can be efficiently compensated by the compressor of the CPA-system. On the other hand, the nonlinear ripples of the chirp are solely due to the modulation which is superimposed onto the envelope. The non-parabolic part of the temporal nonlinear phase is the magenta curve shown in Fig. 5.4(e). Using Eqs. (5.5) and (5.6), it can be demonstrated that in the center of the stretched pulse the modulation has a peak-to-valley depth of $B4\sqrt{r}$. Eq. (5.5) expresses that the amplitude of the modulation follows the shape of the spectrum, as shown by the magenta curve in Fig. 5.4(e). This modulation can be interpreted as a temporal phase-grating.

To evaluate the energy transfer to the side pulses (i.e., temporal diffraction orders) caused by this temporal phase-grating, a few assumptions are made: In general, the sinusoidal phase-modulation acts on both the main and the post-pulse. However, the energy is primarily contained in the main pulse. Thus, the weak post-pulse is neglected in the calculation, although its impact is described via the phase-modulation. Furthermore, the nonlinear temporal phase is reduced to the sinusoidal contribution (i.e., only the last term in Eq. (5.5) is kept) and the slowly varying shape of the amplitude of the modulation is neglected, i.e. $s(T/\phi^{(2)}) \approx 1$ in Eq. (5.5). The phase term that is considered in the following, is represented by the grey curve plotted underneath the magenta curve in Fig. 5.4(e). This way, the approximation would only be exact at the center of the pulse and would result in higher intensities of the side pulses. To account for the pulse-shape,

5.1 Influence of a weak post-pulse

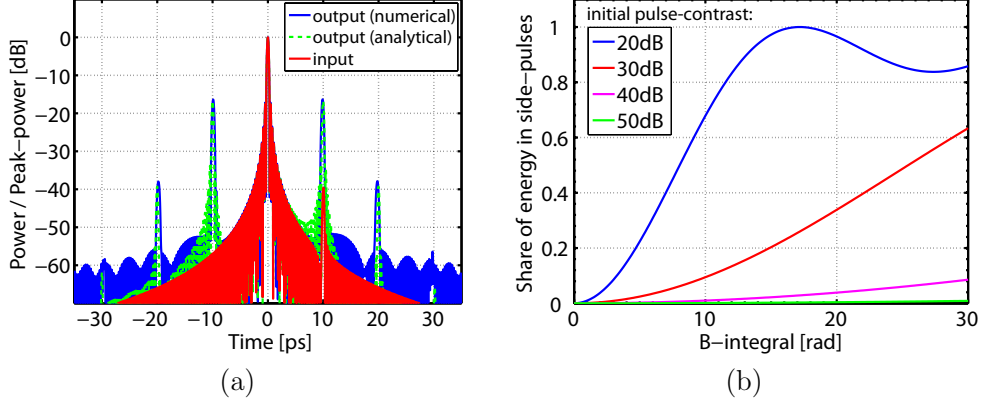


Figure 5.5: (a) Numerical calculation and analytical result (Eq. (5.9)) of the pulse after the nonlinear CPA-system ($B = 20$ rad), the input ($B = 0$ rad) is also shown, (b) total intensity in the side pulses relative to the intensity of the main pulse as a function of the value of the B-integral and for different initial pulse-contrasts r [dB].

a profile-factor p is introduced. For standard spectral profiles p is about 0.7. This value can be regarded as a weighting factor [86]. Thus, Eq. (5.6) can be written as

$$A_{amp}(T) \approx \frac{\exp\left(\frac{gL}{2}\right)}{\sqrt{-i2\pi\phi^{(2)}}} \tilde{A}_0\left(\frac{T}{\phi^{(2)}}\right) \exp\left(-i\frac{T^2}{2\phi^{(2)}}\right) \exp\left(ia \cos\left(T\frac{\Delta t}{\phi^{(2)}} - \frac{(\Delta t)^2}{2\phi^{(2)}}\right)\right). \quad (5.7)$$

Where $pB2\sqrt{r}$ is substituted by the parameter a . Using the definition of the generating function for the Bessel-functions [87],

$$\exp(ia \cos(x - b)) = \sum_{m=-\infty}^{\infty} J_m(a) i^m \exp(-imx) \exp(+imb), \quad (5.8)$$

the last phasor in Eq. (5.7) can be expressed in terms of Bessel-functions. The compression of this stretched multi-pulse signal can also be described analytically [78]. Hence, the final expression for the recompressed multi-pulse is given by

$$A_{out}(T) = \exp\left(\frac{gL}{2}\right) \sum_{m=-\infty}^{\infty} i^m J_m(a) A_0(T + m\Delta t) \exp(i\varphi_m^{out}(T)) \quad (5.9)$$

where

$$\varphi_m^{out}(T) = -m\frac{\Delta t T}{\phi^{(2)}} + m(1 - m)\frac{(\Delta t)^2}{2\phi^{(2)}}. \quad (5.10)$$

These equations show that the energy transfer into the side pulses is determined by the amount of accumulated nonlinear phase-shift (i.e., the B-integral), as well as the initial

5.1 Influence of a weak post-pulse

pulse-contrast r . The pulse-contrast at the output of the nonlinear CPA-system is *not* a function of the delay of the post-pulse Δt [78]. In particular, for small values of the parameter a , the intensity of the first-order pre- and post-pulse relative to the intensity of the zero-order pulse can be approximated by

$$J_1^2(a) \approx \frac{a^2}{4} \approx 2B^2r, \quad (5.11)$$

where p^2 is approximated by 0.5. Thus, the decrease of pulse-contrast is quadratic with the B-integral, and it is linear with the initial pulse-contrast r .

Fig. 5.5 shows the numerical calculation (based on the Fast-fourier transform), as well as the analytical result of the pulse at the output of the nonlinear CPA-system ($p \approx 0.7$). In Fig. 5.5(b), the general behavior of the portion of energy in the side pulses relative to the portion of energy in the main pulse, $1 - J_0^2(pB2\sqrt{r})$, is shown as a function of the B-integral and for different initial pulse-contrasts ($p \approx 0.7$). Thus, applications relying on a high pulse contrast demand a low B-integral of the amplification system and a master-oscillator with an excellent pulse-contrast. At an initial (intensity) pulse-contrast of $r = 10^{-4}$, 10^{-3} or 10^{-2} , no energy will be left in the zero-order (the main pulse) at B-integrals of 170 rad, 54 rad and 17 rad, respectively. It is important to note that the degradation shown in Fig. 5.5(b), is due solely to the amplitude modulations. The interaction with the envelope of the pulse will cause an additional decrease in peak-power of the main pulse. The techniques which control the impact of SPM in nonlinear CPA-systems (chapter 6) demand an excellent pulse-contrast of the master oscillator.

5.2 Influence of weak spectral phase-modulation

As mentioned in the introduction of this chapter, weak initial spectral phase-modulations constitute another origin of pulse-contrast degradation at the output of nonlinear CPA-systems. This is the topic of this section.

This study is particularly relevant since phase-modulations are a subject of concern in every real-world CPA-system. In particular, they can be caused by poor surface qualities of the optical components in bulk stretchers [63], or by group-delay ripples in integrated stretching devices, such as chirped fiber Bragg-gratings, e.g. [55], or chirped volume Bragg-gratings (see section 6.1). Recently, the influence of an initially random phase-modulation on the shape of the stretched pulse has been discussed [84]. The analysis presented here goes further: the impact of the phase-modulation on the pulse-contrast at the output of nonlinear CPA-systems is discussed. As a result of this research, the decrease of pulse-contrast can be estimated with analytical formulas. This analysis also reveals the key parameters. The pulse-degradation implies the generation of pre- and post pulses. The pre-pulses are detrimental for many ultrafast laser applications, such as high field physics (see, for example, [88]).

For the following analysis, it does not matter whether the spectral phase-modulation is acquired before or during the stretching process in the CPA-system. It is assumed that the high-frequency spectral phase modulation is sinusoidal, $d \cos(\Delta t \Omega - b)$. This is a quite simple description of a real modulation, but it serves to reveal the underlying mechanism of the process. In addition to that, useful analytical formulas can be derived. The depth and spectral frequency of the modulation are denoted as d and Δt , respectively. An arbitrary initial shift b is also included. The stretched state of the temporal amplitude of the pulse is given by

$$A_{st}(T) = \frac{1}{2\pi} \int d\Omega \exp(-i\Omega T) \exp\left(i\frac{\phi^{(2)}}{2}\Omega^2\right) \exp(id \cos(\Delta t \Omega - b)) \tilde{A}_0(\Omega). \quad (5.12)$$

It is assumed that the sinusoidal spectral phase-modulation is a perturbation of the stretching phase, and thus, its modulation depth is small. For example, in a bulk stretcher, the modulation may be produced by the limited surface quality of its elements, which are on the scale of about $\lambda/10$ (i.e. 10^{-7} m). This is small compared to the distance that is needed for stretching to pulse-durations of 0.1 ...1 ns (i.e. the distance is typically on the order of 10^{-1} m). Correspondingly, the magnitude of the stretching phase is typically about $10^2 \dots 10^3$ rad. As a consequence, the depth of the phase-modulation can be assumed to be $d < 1$ rad. This assumption is valid for most

5.2 Influence of weak spectral phase-modulation

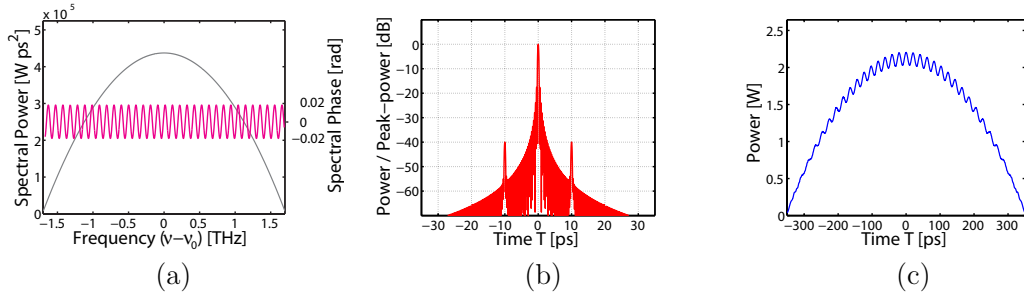


Figure 5.6: (a) Spectral phase-modulation, i.e. a smooth intensity spectrum with a weak sinusoidal spectral phase-modulation ($d=0.02$, $\Delta t = 10$ ps), (b) in time-domain, this corresponds to a transform-limited multi-pulse, (f) the stretched pulse is modulated.

of the stretchers used in practical CPA-systems.

In Fig. 5.6 (which corresponds to the bottom row of Fig.5.1), the depth of the phase-modulation is $d = 0.02$. The corresponding transform-limited pulse is shown in Fig. 5.6(b), and the stretched pulse can be seen in Fig. 5.6(c). To obtain an expression for this modulated stretched pulse, Eq. (5.12) is analytically integrated using the method of stationary phase [79]. The initial spectral amplitude, $\tilde{A}_0(\Omega)$, is assumed to be transform-limited (i.e., constant spectral phase). The spectrum, $|\tilde{A}_0(\Omega)|^2$, is unchanged during stretching as is expected for a multiplication with a phase-transfer function. In particular, the sinusoidal phase-modulation is expanded in terms of Bessel-functions using Eq. (5.8). From a physical point of view, a sinusoidal phase-modulation corresponds to temporally delayed pulses. However, in the stretched state of the pulse, these pulses overlap, causing interference, which is the primary reason for the modulation seen in Fig. 5.1(f). The intensity distribution of the stretched pulse can be approximated by

$$|A_{st}(T)|^2 \approx \frac{|\tilde{A}_0(T/\phi^{(2)})|^2}{2\pi\phi^{(2)}} \left[J_0^2(d) + J_0(d)J_1(d)4 \sin\left(\frac{(\Delta t)^2}{2\phi^{(2)}}\right) \cos\left(\Delta t \frac{T}{\phi^{(2)}} - b\right) \right], \quad (5.13)$$

where it is assumed that the modulation depth is small, i.e. $d < 1$ rad, so that the significant terms in the Bessel-function-expansion are only $m = -1, 0, 1$ are significant. Eq. (5.13) describes the modulated stretched pulse very well (as proven by numerical calculation), and clearly shows that a high-frequency modulation is superimposed on the envelope of the pulse as previously noted. In particular, this high-frequency modulation shows the same characteristic behavior as the initial spectral phase-modulation, i.e. $\cos\left(\Delta t \frac{T}{\phi^{(2)}} - b\right)$. The amplitude of the phase-modulation is strongly dependent on the initial modulation frequency Δt and the slope of the stretching chirp.

5.2 Influence of weak spectral phase-modulation

The impact of SPM is described by Eq. (5.6). For the evaluation of this expression, the analytical form of the stretched pulse is used. During nonlinear propagation, the modulated stretched pulse acquires a high-frequency temporal phase-modulation. As a consequence, a 'temporal phase-grating' is given by [79]

$$\exp(i\gamma L_{eff} |A_{st}(T)|^2) \approx \exp\left(ipB2d \sin\left(\frac{(\Delta t)^2}{2\phi^{(2)}}\right) \cos\left(\Delta t \frac{T}{\phi^{(2)}} - b\right)\right). \quad (5.14)$$

The value of the B-integral is B. As mentioned before, the temporal phase-grating causes an energy transfer from the main pulse to the side-pulses. With these assumptions, and additional steps similar to the previous section (see also [79]), the final expression for the recompressed multi-pulse at the output of the nonlinear CPA-system can be expressed as

$$A_{out}(T) = \exp\left(\frac{gL}{2}\right) \sum_{m=-\infty}^{\infty} i^m J_m(a) A_0(T + m\Delta t) \exp(i\varphi_m^{out}(T)) \quad (5.15)$$

with

$$\varphi_m^{out}(T) = -m \frac{\Delta t T}{\phi^{(2)}} - m^2 \frac{(\Delta t)^2}{2\phi^{(2)}} + mb. \quad (5.16)$$

The parameter a is the amplitude of the temporal phase-modulation, and is given by

$$a = pB2d \sin\left(\frac{(\Delta t)^2}{2\phi^{(2)}}\right). \quad (5.17)$$

These equations demonstrate that the initial spectral phase-modulation results in a transfer of energy from the main pulse to the side pulses (both pre- and post-pulses) at the output of nonlinear CPA-systems. The final energy distribution is determined by the parameter a. If the parameter $a < 1$, then the intensity of the first pre- and post pulse relative to the main pulse can be approximated by

$$J_1^2(a) \approx a^2/4 \approx 2B^2d \sin^2\left(\frac{(\Delta t)^2}{2\phi^{(2)}}\right). \quad (5.18)$$

The output of the nonlinear CPA-system is shown in Fig. 5.7(a). The initial sinusoidal phase-modulation is characterized by the depth $d=0.02$ and spectral frequency $\Delta t = 10$ ps. The input signal is the same as shown in Fig. 5.6(a-c). The initial pulse-contrast is 40 dB. In Fig. 5.7, the analytical result is compared to numerical calculation (based on the Fast-Fourier transform). Fig. 5.7(b) shows that the output pulse-contrast is significantly reduced to 10 dB at a B-integral of 20 rad. Ideally, the parabolic spectrum controls of the impact of nonlinearity: a parabolic SPM can be efficiently compensated by the compressor (see section 6.3). Yet, in spite of this, high pre- and post-pulses can

5.2 Influence of weak spectral phase-modulation

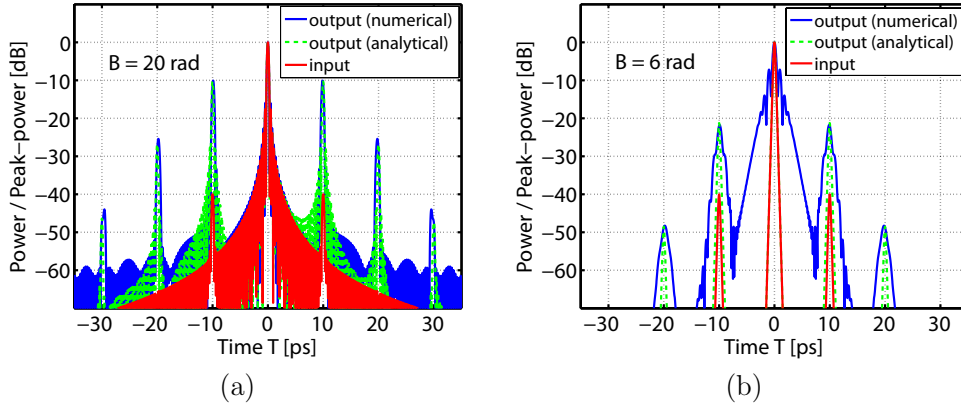


Figure 5.7: (a) Numerical and analytical results of the pulses at the output of the nonlinear CPA-system for the configuration shown in Fig. 5.6(a-c). The spectrum is parabolic. (b) Intensity-distributions for the case of an initial sech^2 -shape. The parameters of the phase-modulation and $\phi^{(2)}$ are the same as in (a).

arise if the seed of the nonlinear amplifier shows a weak phase-modulation.

While deriving Eq. (5.15), the impact of the intensity envelope was neglected. Although the pulse-contrast degradation due to the envelope is not included in the analysis, the intensities of the pre- and post-pulses relative to the main pulse are still well estimated by the model for various initial pulse envelopes. The case of a sech^2 -spectrum is shown in Fig. 5.7(b). In this simulation, the B-integral is lower than in Fig. 5.7(a), since the pulse-degradation due to the envelope is quite strong, and would eventually preclude a distinction between the pulse-contrast degradation due to the initial phase-modulation and that due to the impact of the envelope.

The case of an initial phase-modulation differs significantly from the pulse-contrast degradation due to an initial amplitude modulation. As shown above, the intensity distribution of the satellite pulses depends on the stretching. Specifically, the parameter a depends on the term $\sin((\Delta t)^2/(2\phi^{(2)}))$. The spectral modulation frequency Δt can take values in the range of several picoseconds and $\phi^{(2)}$ is in the order of about $10 \text{ ps}^2/\text{rad}$. Thus, in practical systems the ratio $(\Delta t)^2/(2\phi^{(2)})$ can take any (relevant) value between 0 and 2π . Fig. 5.8 shows the behavior of the energy transfer to the side-pulses as a function of the product of the B-integral and the modulation-depth d for different characteristic ratios $(\Delta t)^2/(2\phi^{(2)})$. Pulse-degradation is lower for small Δt and high magnitudes of the stretching chirp $\phi^{(2)}$, i.e. $2\phi^{(2)} \gg (\Delta t)^2$. Thus, a high stretching chirp results in a higher contrast for small Δt . However, in practical CPA-systems, the magnitude of the stretching chirp is limited to the order of 10 ps^2 . It is

5.2 Influence of weak spectral phase-modulation

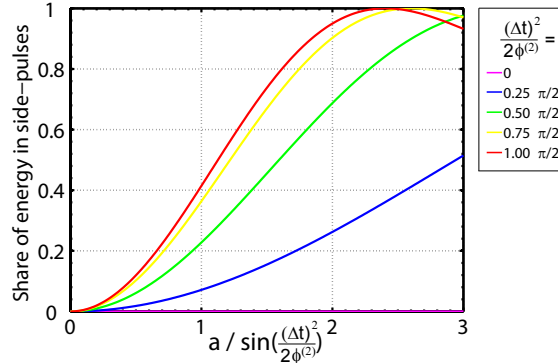


Figure 5.8: (a) Total intensity of the side-pulses relative to the intensity of the main pulse, $1 - J_0^2(a)$, as a function of the parameter a divided by $\sin(\Delta t)^2 / (2\phi^{(2)})$. The decrease is calculated for different ratios $(\Delta t)^2 / (2\phi^{(2)})$ in the sine of the parameter a .

also worth noting that there may be stretching configurations where the pulse-contrast is not degraded at all at the output of a nonlinear CPA-system. These points are given by $(\Delta t)^2 / (2\phi^{(2)}) = k\pi$, where k is an integer. However, in practice, the real phase-modulation will not be sinusoidal, so that this is a rather theoretical argument.

To summarize, initial perturbations imposed on the input pulse affect the pulse contrast at the output of nonlinear CPA-systems. Weak initial post-pulses, as well as weak phase-modulations, cause pulse-contrast degradation at the output. The decrease of pulse-quality manifests itself in form of satellite pulses. The relative intensities of these pulses can be determined using Bessel-functions.

The impact of weak post-pulses and weak spectral phase-modulations was treated separately. In practice, however, both effects will act simultaneously, making it hard to identify the origin of the observable distortions. Furthermore, even though any arbitrary initial phase-modulation would cause a pulse-contrast degradation, the specific case of a sinusoidal phase-modulation has been considered.

In view of this detrimental process inherent in every real nonlinear CPA-system, the methods developed to control the impact of SPM in CPA-systems must be reassessed. The pulse-contrast degradation imposes major limitations on these techniques. The theoretical results allow for determination of useful operation regimes of nonlinear CPA-systems. Future developments of nonlinear CPA-systems will place considerable emphasis on improving the quality of the stretched pulse.

6 Pulse-shaping strategies in nonlinear chirped pulse amplification

In this chapter, novel methods that allow for control of the impact of SPM in nonlinear CPA-systems are experimentally demonstrated. The design of these techniques is based on the model developed in chapter 4. Emphasis is placed on active control of the influence of SPM by spectral amplitude-shaping, as well as spectral phase-shaping. The significance of the polarization state is highlighted. Finally, the advances achieved during the course of this thesis and existing concepts are put into context.

6.1 Compensation of SPM using fiber-dispersion

In this section, the compensation of SPM with positive dispersion of the fiber is discussed and experimentally demonstrated. The considerations are relevant to nonlinear CPA-systems employing a static stretcher and compressor, e.g. a chirped volume Bragg-grating (CVBG). A system such as this is employed in one experiment.

In the following, the condition for best compression is derived and design-guidelines are presented. If the stretcher and compressor of the CPA-system are matched to each other, i.e. $\phi_{co}^{(2)} = -\phi_{st}^{(2)}$, the (partial) compensation of SPM can be achieved by the positive fiber-dispersion. In the following, the compensation of SPM with the dominating parabolic phase-term $\varphi_{disp} = \beta^{(2)}L\Omega^2/2$ is discussed. The second derivative of the mode-propagation constant and the length of the fiber are, respectively, $\beta^{(2)}$ and L . Using Eq. (4.9), the output pulse is described by

$$A_{out}(T) = \sqrt{GF} \int \frac{d\Omega}{2\pi} \exp(-i\Omega T) \sqrt{s(\Omega)} \exp\left(i \left[\frac{\beta^{(2)}L}{2} \Omega^2 + B s(\Omega) \right]\right). \quad (6.1)$$

If the center wavelength of the spectrum is given, then the parameter $\beta^{(2)}$ is fixed and, due to dispersion, the phase can be varied by the fiber length L . Furthermore, if the shape of the spectrum is specified, e.g. sech^2 , then the best Strehl-ratio is only a function of the bandwidth, the length of the dispersive medium and the B-integral. The optimal fiber-length L , which is a function of both the spectral bandwidth and the B-integral, can be obtained by using Eq. (6.1), whereby the highest Strehl-ratio determines the optimal parameter configuration.

6.1 Compensation of SPM using fiber-dispersion

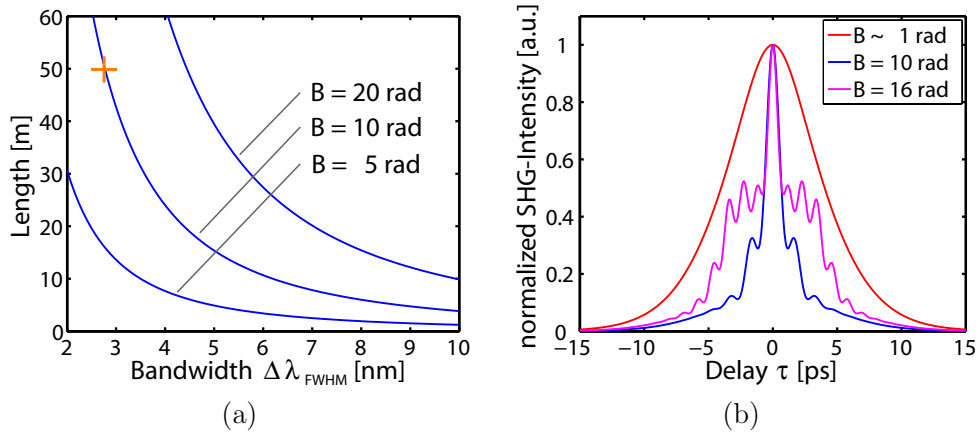


Figure 6.1: (a) The condition for best phase-compensation: fiber length as a function of the FWHM of the sech^2 spectrum for the B-integral values 5 rad, 10 rad and 20 rad. The center-wavelength is 1030 nm, where $\beta^{(2)} = 25 \text{ ps}^2/\text{km}$. The red cross marks the experimental situation. (b) For this configuration of 2.8 nm FWHM and a 50 m fiber, the theoretical autocorrelation is plotted at an optimal B-integral of 10 rad. Curves are also shown at B-integrals above and below the optimum. The traces are normalized to the peak.

Fig. 6.1(a) illustrates the relationship for the case of a sech^2 -spectrum. The red cross marks the optimal situation shown in Fig. 6.1(b). This parameter configuration was chosen with regard to one experimental configuration (using the Öffner-stretcher) : a sech^2 -spectrum with bandwidth of 2.8 nm (FWHM), 50 m fiber length, and a B-integral of about 10 rad (at the optimum). Fig. 6.1(b) illustrates the impact of the phase-compensation on the output pulse. The best autocorrelation is given at the B-integral corresponding to the phase-compensation condition. The autocorrelation trace shows tails due to residual phase terms. This has already been discussed in the previous section. B-integrals below and above the optimal value will result in temporal broadening. For the special case of a parabolic spectrum, the phase-compensation can be determined analytically: A parabolic spectrum $s(\Omega)$ allows perfect compensation of the phase $B \cdot s(\Omega)$ with the parabolic phase due to positive dispersion. In particular, the parabolic spectrum can be expressed as $s(\Omega) = 1 - \Omega^2 (\sqrt{2}/\Delta\Omega_{\text{FWHM}})^2$. $\Delta\Omega_{\text{FWHM}}$ is the full-width-at-half-maximum of the spectrum. The polynomial expansion of the spectral phase due to SPM, Eq. (4.11), contains terms up to second order, and the zero and first (which is zero anyway) term can be neglected because they imply only a constant phase-offset and a temporal delay after compression. The condition for phase-compensation is given by

$$B \frac{2}{\Delta\Omega_{\text{FWHM}}^2} = \beta^{(2)} L / 2. \quad (6.2)$$

6.1 Compensation of SPM using fiber-dispersion

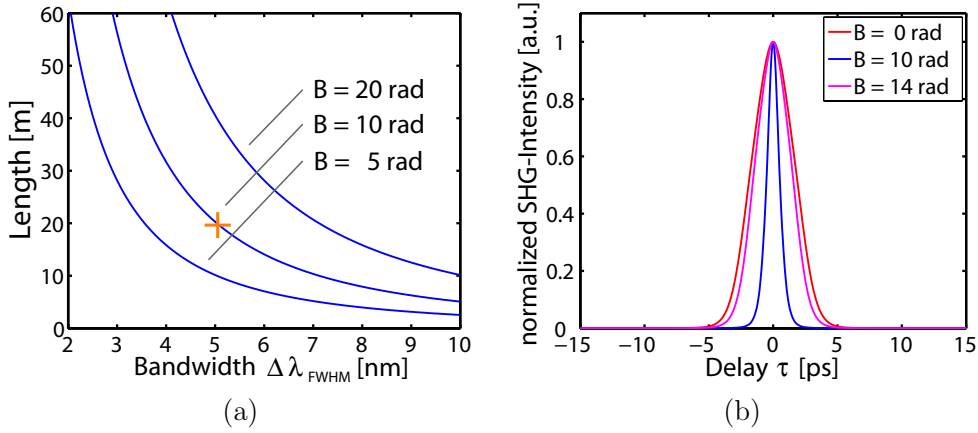


Figure 6.2: (a) The condition for phase-compensation: length of the amplifier as a function of the FWHM of the parabolic spectrum for different B-integral values. The center-wavelength is 1030 nm and $\beta^{(2)} = 25 \text{ ps}^2/\text{km}$. The red cross marks the optimal configuration shown in (b), where the FWHM is 5 nm and the fiber is 20 m. The autocorrelation is plotted at the optimal B-integral of 10 rad. Autocorrelations are also shown above and below the optimum.

The relation determines the length of the fiber-amplifier required for compensation of the spectral phase due to SPM. The phase-compensation is strongly dependent on the bandwidth of the spectrum. According to Eq. (6.2), a broader bandwidth permits operation at higher B-integrals. This can also be seen from Fig. 6.2(a). Comparing Fig. 6.2 and Fig. 6.1, it can be noticed that for high B-integrals, Eq. (6.2) gives quite a good estimate even for non-parabolic spectral shapes. Again, in Fig. 6.2(a), the red cross corresponds to the parameter configuration shown at the right side.

In the following, the compensation of the SPM with positive dispersion is experimentally demonstrated. First, a system employing a chirped volume Bragg-grating (CVBG) is presented; then, a diffraction grating-based system is used. Requirements on the stretching unit are discussed.

System based on a chirped volume Bragg-grating

A schematic of the experimental setup employing the CVBG is shown in Fig. 6.3. The setup consists of a passively mode-locked laser (10 MHz, ~ 400 fs, 1030 nm, 1.5 W), one CVBG is used for both stretching and compression of the pulse. The CVBG has a spectral window of 4.2 nm at a central wavelength of 1029.6 nm. The length of the device is 3 cm corresponding to a duration of 190 ps for the stretched pulse. Fig. 6.4(a) shows the (simulated) spectrum at the input of the fiber. It was estimated by using the spectral window of the CVBG. The phase-compensation occurs during the nonlinear

6.1 Compensation of SPM using fiber-dispersion

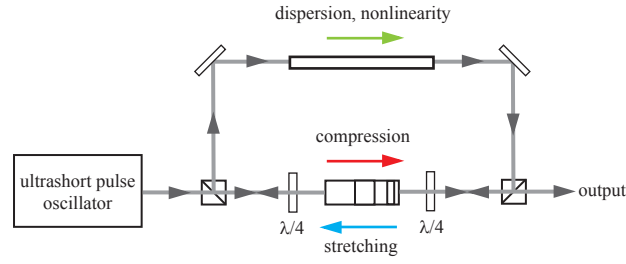


Figure 6.3: Schematic of setup of the ultra-compact fiber CPA-system with intrinsic phase-compensation. One CVBG is used for stretching and compression of the pulses.

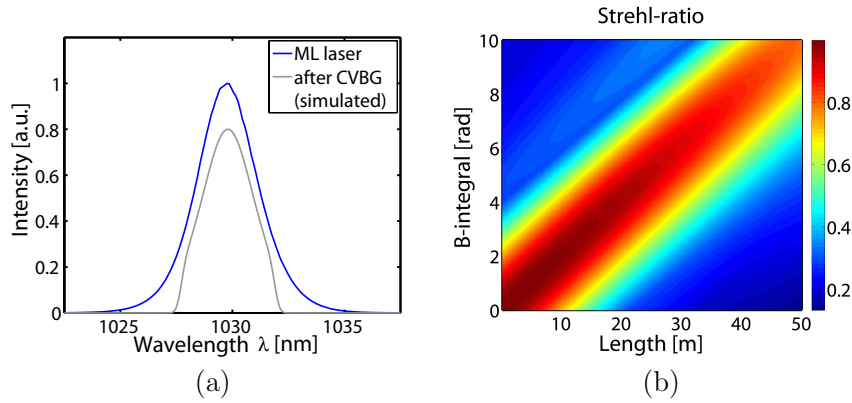


Figure 6.4: (a) Experimental spectrum before the CVBG (i.e. the oscillator spectrum), and the spectrum after stretching with the CVBG. This shape is simulated taking the spectral window and the reflectivity into account. (b) Using the latter, the relative peak-power at the output of the CPA-system is calculated as a function of the B-integral and the fiber-length.

propagation of the stretched pulse in the fiber (mode-field diameter is $5 \mu\text{m}$). Since the spectral shape is given, the Strehl-ratio can be calculated using Eq. (6.1), with $\beta^{(2)} = 25 \text{ ps}^2/\text{km}$. In Fig. 6.4(b), the resulting 2D map is shown as a function of the length L and the B-integral. It can be seen that for this parameter configuration, a clear optimum in CPA-performance will only be seen for fiber-lengths $L > 10 \text{ m}$.

In the experiment, the fiber-length is varied between 10 m and 50 m in steps of 10 m by cutting from the 50 m length of fiber. At every length, the input power is varied to obtain different B-integrals values. The spectrum and autocorrelation are recorded for each configuration. Figure 6.5(a) shows the widths of the measured autocorrelations over the B-integral values. At the minima of the curves, almost transform-limited pulses are produced, since the fiber dispersion and nonlinearity compensate each other. For a length of 40 m, Fig. 6.5(b) shows the autocorrelation traces for the different B-integral values. The optimum corresponds to the B-integral of about 6 rad.

6.1 Compensation of SPM using fiber-dispersion

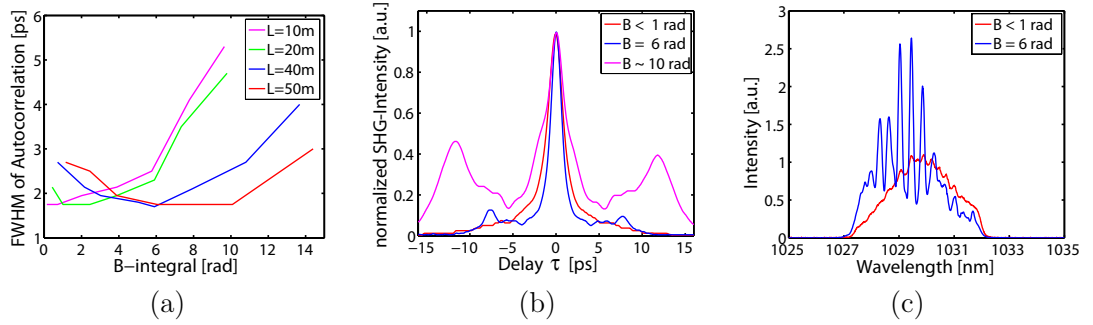


Figure 6.5: (a) Measured FWHM of the autocorrelation versus B-integral of the nonlinear pulse propagation for different fiber-lengths, (b) Autocorrelations for characteristic B-integral values for 40 m length of fiber, (c) output spectrum at a low and a high B-integral.

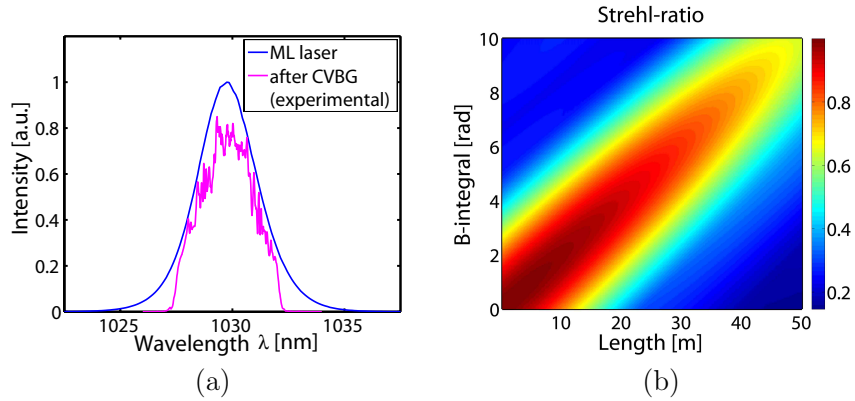


Figure 6.6: (a) Experimental spectrum of the pulse before and after the CVBG. (b) Using the latter, the (normalized) peak-power at the output of the CPA-system (i.e., the Strehl-ratio) is calculated as a function of the B-integral and the fiber-length.

However, the detrimental effect of enhancement of initially weak perturbations is overlapping the effect of phase-compensation. The CVBG imposes spectral amplitude modulation with a peak-to-valley depth of $\sim 10\%$, as shown in Fig. 6.5. For such a spectrum, there will be a build-up of spectral modulations with increasing B-integral: Fig. 6.5(c) shows spectra at $B \sim 0$ rad and $B = 6$ rad. This corresponds to a degradation of pulse contrast, as discussed in chapter 5.

To evaluate the performance of this real-world system, Fig. 6.6 shows the same simulation as Fig. 6.4, but starting with the experimental spectrum after the CVBG. It can be seen that the relative peak-power is washed out with increasing B-integral. This is in agreement with the experimental observation. It should be noted that the simulation only accounts for the observable modulations in the spectrum, however, phase-perturbations could also be an issue.

System based on Öffner-stretcher

To clearly demonstrate the compensation of SPM at high B-integrals, a grating-based Öffner-stretcher was designed and constructed. Thanks to high surface-qualities of its components, and a (nearly) aberration-free imaging system, clean stretched pulses are produced. Thus, a better output pulse-contrast can be obtained.

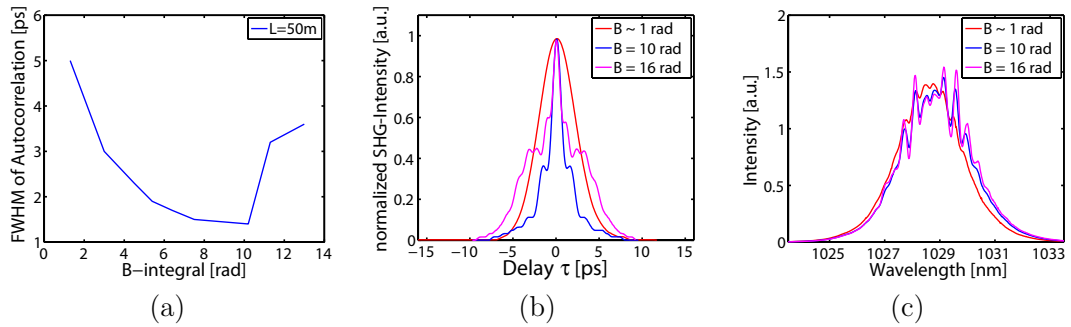


Figure 6.7: Experimental results with the Öffner-stretcher system: (a) Measured temporal widths (FWHM) of the autocorrelation traces as function of the B-integral of the nonlinear pulse propagation for different fiber-lengths, (b) autocorrelation traces at different B-integral values for the 50 m fiber-length, (c) corresponding output spectra.

In this experiment, the same oscillator is used as in the system employing the CVBG. The Öffner-stretcher broadens the pulses to 170 ps. The stretcher and compressor are perfectly matched. Before alignment of the compressor, 30 cm length of fiber (with negligible dispersion) is introduced between stretcher and compressor. Then, the 50 m length of fiber is spliced at the input of this piece of fiber. In this way, the angle of incidence on the compressor gratings, and thus the perfect alignment, is maintained when adding 50 m length of fiber, which introduces dispersion. Figure 6.7(a) shows the temporal widths of the autocorrelations versus B-integral for this fiber (which is slightly different to the fiber of CVBG setup, the MFD is $6 \mu\text{m}$). Since the highest B-integral is of interest, the compensation is only demonstrated using the 50 m length. The autocorrelations are shown in Fig. 6.7(b). Compared to the experiment with the CVBG, the quality of the compression has improved. Outside the window bounded by ± 10 ps there are no satellite pulses. This agrees with the quality of the spectra, which are shown in Fig. 6.7(c). Only a minor build up of distortions can be seen for B-integrals > 10 rad. Using the formulas of chapter 5, the temporal contrast of the recompressed pulse is estimated to be > 30 dB. The experimental autocorrelations agree well with the calculations, which have already been shown in Fig. 6.1(b).

Improved pulse-contrast by spectral clipping

The previous section has shown that a positive parabolic phase can partially compensate the SPM of chirped pulses. However, the residual phase prevents the generation of transform-limited output pulses. The phase-shifts are particularly high at the edges of the spectrum, as shown in Fig. 4.3(a). Therefore, spectral clipping is used to improve the pulse-quality. Fig. 6.8(a) shows this improvement: If a bandpass is introduced into the stretcher, then the Strehl-ratio increases at the output of the nonlinear CPA-system ($B = 10$ rad). The bandpass width is measured in units of the FWHM of the whole sech^2 -spectrum. The smaller the bandpass width the higher the Strehl-ratio.

On the other hand, a reduced spectral bandwidth corresponds to a lower peak-power of the transform limited pulse, as shown in Fig. 6.9. Thus, a compromise between improvement of the Strehl-ratio and decrease of peak-power must be found. At a given bandpass width, the Strehl-ratio is therefore weighted by the peak-power of the transform-limit of the clipped spectrum. Fig. 6.8(b) shows this figure-of-merit as a function of the bandpass width (at $B = 10$ rad). An optimum is found at a bandpass-width of 1.4 times the FWHM of the original spectrum. The pulses are close to the transform-limit, and the increase of performance is around 25% compared to unclipped spectrum. The optimal bandpass width changes with B-integral. The analysis also depends on the shape of the spectrum. Fig. 6.10(a) shows the B-integral as a function of the optimal bandpass width. The width of the spectral window must be reduced if the B-integral increases.

This behavior is experimentally verified by the setup employing the Öffner-stretcher (see previous subsection). The spectrum is symmetrically clipped in the stretcher. The cut is monitored at the output of the system ($B \approx 10$ rad). Simultaneously, the autocorrelations are recorded. Fig. 6.11 shows the improvement of pulse-quality with decreasing spectral window of the stretcher. The experimental optimum is at $1.7 \cdot \text{FWHM}$. The deviation from the theoretical value is due to the imprecise estimation of the B-integral. The design of a stretcher for a nonlinear CPA-system could take the improvement of pulse-quality due to the spectral window into account. In general, the aperture of the diffraction grating determines the duration of the stretched pulse. Thus, a reduced bandwidth would enable an increased slope of the stretching chirp ($\Delta t = \phi^{(2)} \Delta \omega$). Such an adapted design will enhance the output peak-power. If $\Delta \omega_0$ is the bandwidth of the linear system, then the nonlinear system will require $\Delta \omega_{new}$ for a certain B-integral value. Thus, the slope of the stretching chirp $\phi_{st}^{(2)}$ can be increased by the factor $\Delta \omega_0 / \Delta \omega_{new}$. The B-integral is inversely proportional to $\phi_{st}^{(2)}$, see Eq. (4.3). Thus, to reach the same B-integral (for the specified bandpass), the peak-power must be enhanced by the same factor. Fig. 6.10(b) shows this increase as a function of the B-integral.

6.1 Compensation of SPM using fiber-dispersion

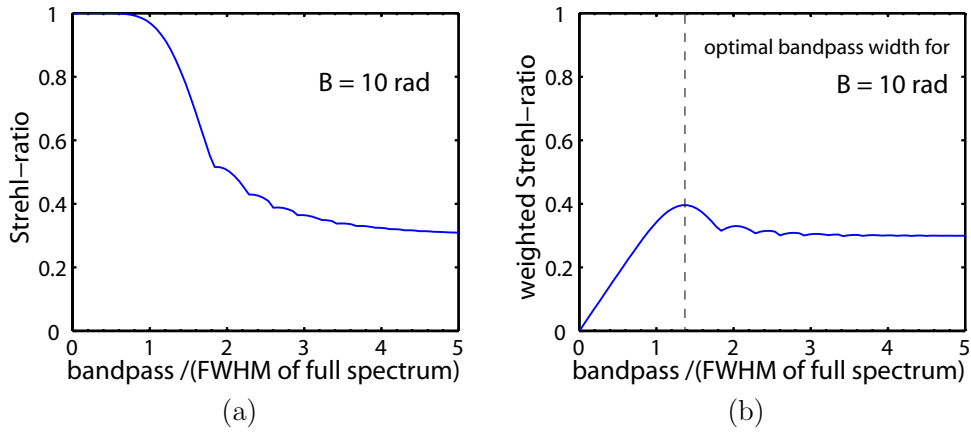


Figure 6.8: (a) Strehl-ratio as a function of the width of the bandpass (in units of the FWHM of the full spectrum). The spectral clipping of the full sech^2 -spectrum is symmetric. The B-integral is $B = 10$ rad for every bandpass-width, (b) the Strehl-ratio weighted by the peak-power of the transform-limit of the clipped spectrum (see Fig. 6.9(b)).

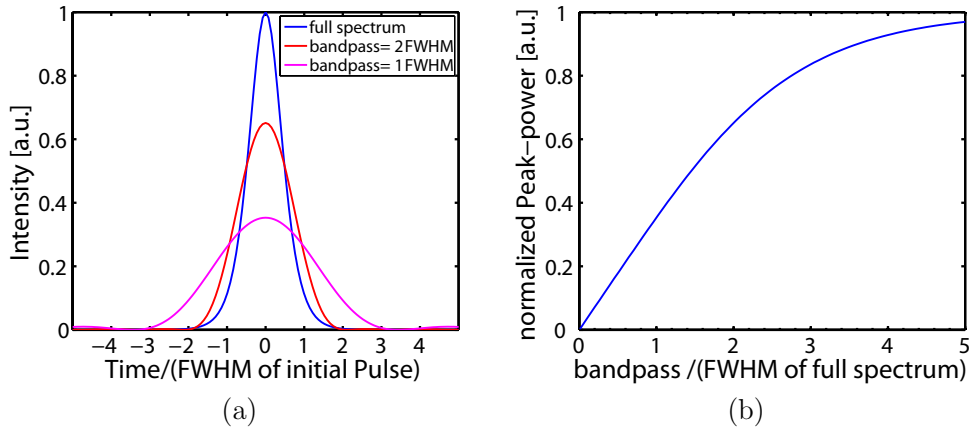


Figure 6.9: (a) Decrease of peak-power by spectral clipping of a transform-limited sech^2 -pulse: (a) initial sech^2 -pulse, and temporally broadened pulses due to symmetric, rectangular bandpassing of the spectrum through filter-width of size of 1 and 2-times the FWHM of the initial spectrum. The pulses have the same energy. (b) Peak-power as a function of the width of the bandpass.

6.1 Compensation of SPM using fiber-dispersion

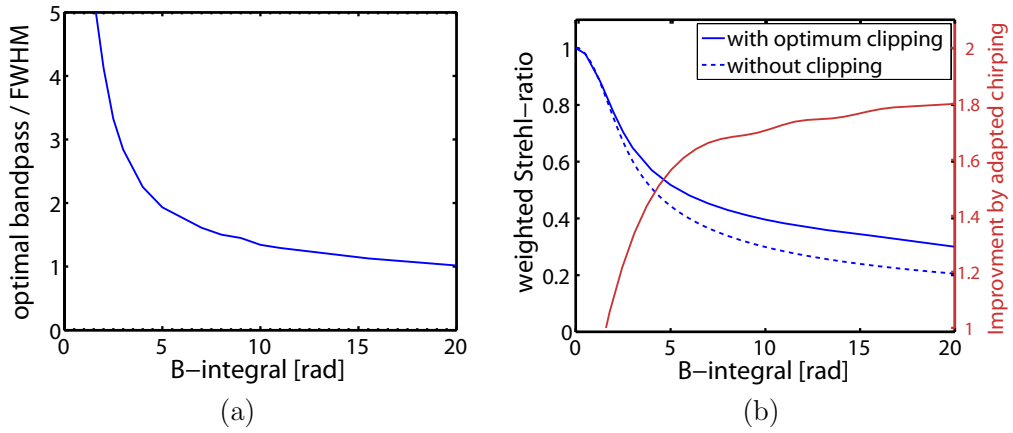


Figure 6.10: (a) Optimal bandpass width as a function of the B-integral. The unclipped spectrum exhibits a sech^2 -shape. (b) Along this optimal curve, the peak-power decreases, however, it is enhanced compared to the case of an unclipped spectrum. If the stretcher is adjusted such that it produces the same temporal duration at a reduced spectral window, higher peak-powers are possible.

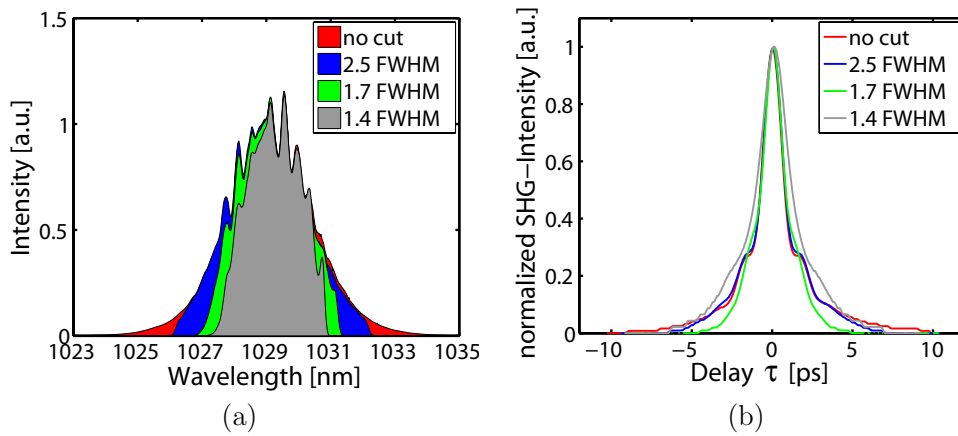


Figure 6.11: (a) Output spectra at a B-integral of 10 rad for different spectral windows (in units of FWHM of the uncut spectrum) (b) Corresponding autocorrelation curves.

6.2 Partial compensation of SPM with GVD and TOD

To summarize, SPM accumulated in a chirped pulse system has been partially compensated using fiber-dispersion. A condition for best phase-compensation could be determined. Improvement of pulse-quality can be achieved by clipping the edges of the spectrum in the stretcher. The design guidelines presented in this section already allow setting up compact nonlinear CPA-systems with a good quality of the output pulse. The use of static stretchers and compressors has been highlighted. In particular, novel chirped volume Bragg gratings possess an intrinsic spectral bandpass. However, in an experimental implementation using these devices, it is observed that small scale perturbations impose limitations on the quality of the recompressed pulse. Currently, bulk grating stretchers lead to better output pulse-contrasts.

6.2 Partial compensation of SPM with GVD and TOD

In linear CPA-systems using Yb-doped amplifiers, the higher order dispersion of a fiber stretcher cannot be compensated by a grating compressor (TOD 2-10 times larger, and equal sign). In particular, third order dispersion adds and results in a dominating residual cubic phase term after compression. This deforms and broadens the output pulse, e.g. [34]. Thus, fiber stretchers are unacceptable at least in linear CPA-systems. In nonlinear operation of a CPA-system, SPM can be compensated to some degree by a cubic spectral phase [90]. In the following, this subject is put in context to the other methods using the analytical model of section 4.1.

The output pulse of the system can be approximated by Eq. (4.9):

$$A_{out}(T) = \sqrt{GF} \int \frac{d\Omega}{2\pi} \exp(-i\Omega T) \sqrt{s(\Omega)} \exp\left(i \left[\frac{\Delta\phi^{(2)}\Omega^2}{2} + \frac{\Delta\phi^{(3)}\Omega^3}{6} + B \cdot s(\Omega) \right]\right), \quad (6.3)$$

where the phase due to the stretcher-compressor-mismatch is given by $\Delta\phi^{(2)}\Omega^2/2 + \Delta\phi^{(3)}\Omega^3/6$. The coefficients $\Delta\phi^{(2)}$ and $\Delta\phi^{(3)}$ denote GVD and TOD, respectively. The dimensionless parameters $|\text{GVD}|(\Delta\Omega)^2$ and $|\text{GVD}/\text{TOD}|(\Delta\Omega)$ are introduced to measure the amount of parabolic phase and the (relative) amount of cubic phase, respectively. $\Delta\Omega$ denotes a characteristic scale of the spectrum. In the following, the FWHM will be used. To obtain the highest peak power for a given spectral shape $s(\Omega)$ and B-integral, both dimensionless parameters must be varied.

Symmetric spectra

For a sech^2 spectrum and $B = 10$ rad, Fig. 6.12(a) shows the Strehl ratio resulting from the partial compensation of SPM with GVD and TOD as independent variables. Fig.

6.2 Partial compensation of SPM with GVD and TOD

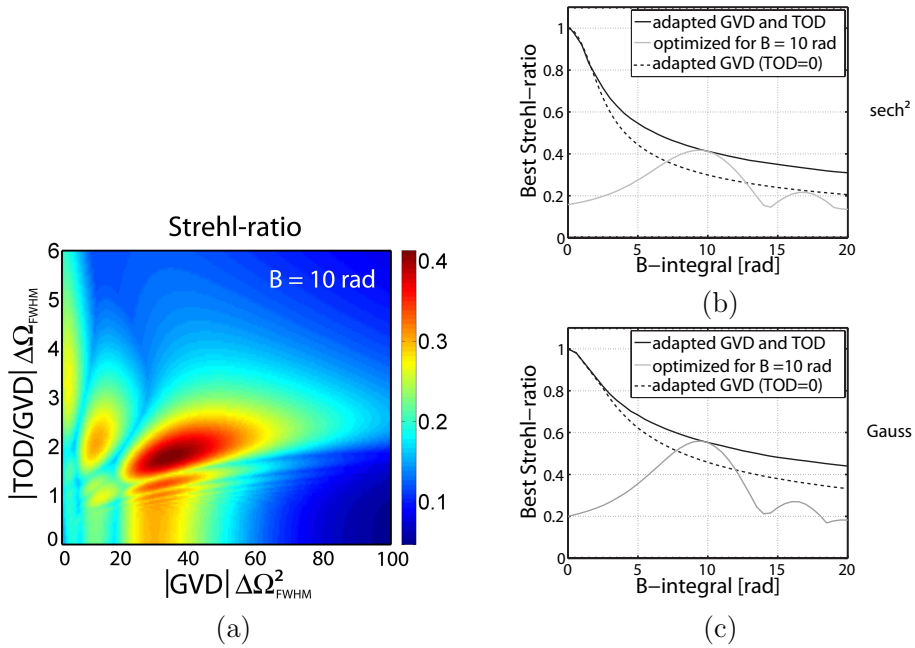


Figure 6.12: (a) Strehl ratio with GVD and TOD as independent variables at $B = 10$ rad for a sech^2 spectrum. (b) and (c) Strehl ratio as a function of the B-integral for a sech^2 and Gaussian spectrum, respectively.

6.12(b) shows the best Strehl-ratio as a function of B-integral if SPM is compensated by GVD and TOD (solid line). It can be seen that the adjustment of both parabolic and cubic phase is superior to an adaptation with only GVD (dashed line). However, in practice, the optimal operating point is dictated by the length of the fiber stretcher, i.e. TOD cannot be adjusted in an adaptive manner [90]. For example, if the stretcher-compressor-combination is optimized for $B = 10$ rad, the system will show a behavior similar to the grey line in Fig. 6.12(b). The output pulse at $B = 10$ rad is shorter than in the absence of nonlinearity ($B = 0$ rad). The principle outcome of the simulation agrees with the findings in [81]. It is worth noting that the root-mean-square pulse duration increases. However, the increase is slower than the increase in relative peak-power. So, the increased peak-power is accompanied by a small sacrifice of pulse contrast [81]. The case of a Gaussian spectrum is displayed in Fig. 6.12(c).

The partial compensation of SPM by GVD and TOD is not limited to fiber devices. For example, using high-energy master oscillators, nonlinearity in the stretcher may be detrimental and it is more sensible to use a mismatched grating stretcher-compressor [91]. An additional advantage is that optimization is possible for any intermediate nonlinear phase shift by adjusting the incidence angle on the stretcher grating.

6.2 Partial compensation of SPM with GVD and TOD

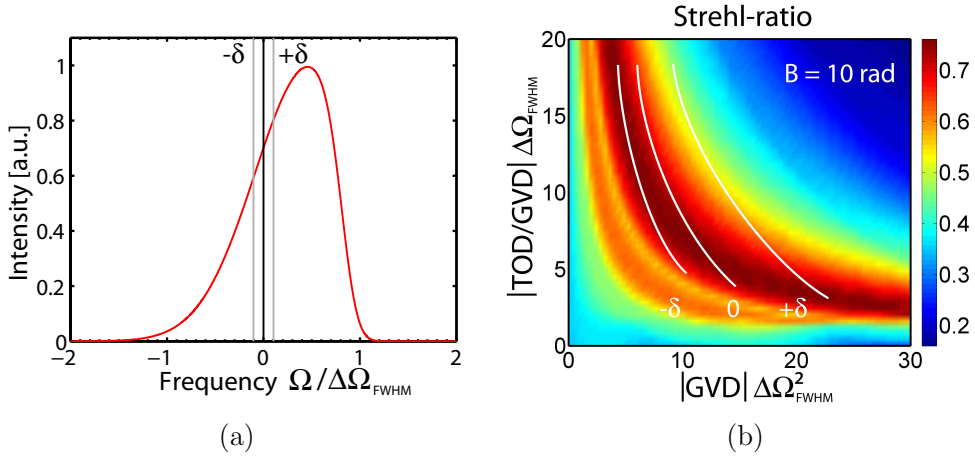


Figure 6.13: (a) 'Cubicon'-spectrum, (b) Strehl ratio with GVD and TOD as independent variables at $B = 10$ rad for this shape. To obtain the highest values, the position of the spectrum is varied relative to the spectral phase. Iso-shift lines for $-\delta$, 0 , and $+\delta$ are indicated.

Asymmetric spectra

The performance of CPA-systems using TOD and GVD for SPM compensation can be greatly enhanced by using highly asymmetric - near triangular - spectral shapes (also termed 'Cubicons') [92]. Fig. 6.13(a) shows an example for such a shape. Such spectra can be obtained by gain shaping inside the fiber amplifier [93]: Because the peak gain of Yb-doped amplifiers is around 1030 nm, the peak of an injected spectrum centered between 1045-1055 nm will be blue shifted. In the presence of SPM the high frequency components will experience a higher phase-shift compared to the low frequency components. The nonlinear phase shifts induce a phase similar to a combination of GVD and TOD. Thus, for a certain output power and certain input spectrum, the positive TOD from the phase mismatch between fiber stretcher and bulk grating compressor can be almost compensated. The spectral situation of the spectrum relative to the phase of the stretcher-compressor-mismatch strongly affects the quality of the output pulse. Therefore, practical systems implement tuneable bandpass filters [92]. To enable flexible control, the spectral bandwidth of the seed source should be larger than the filter bandpass. Moreover, inflexions at the 'red' edge of the spectrum should be avoided to ensure good output pulse quality. In Fig. 6.13(a), the low frequency side of the spectrum exhibits a Gaussian-shape. The phase compensation would improve, if a super-Gaussian shape is used. Fig. 6.13(b) shows the Strehl-ratio at the output of the nonlinear CPA-system ($B = 10$ rad) with GVD and TOD as independent variables. Fig. 6.14 shows the behavior of the best Strehl-ratio with increasing B-integral while GVD and TOD are continuously adapted (solid line). If the 'red' side of the spectrum exhibits super-Gauss

6.2 Partial compensation of SPM with GVD and TOD

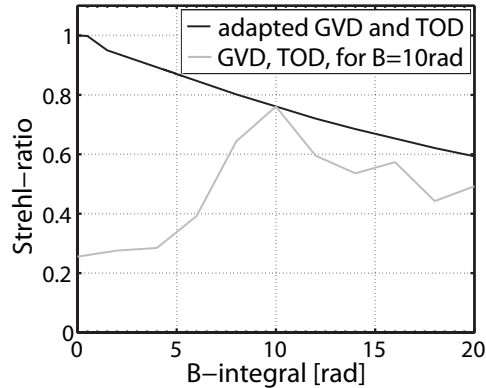


Figure 6.14: Strehl-ratio as a function of the B-integral for the 'Cubicon'-type spectrum.

dependence (i.e. $\sim \exp(-c \cdot \Omega^4)$), the Strehl ratio is 0.85 at $B = 10$ rad, and 0.75 at $B = 20$ rad. If the stretcher-compressor-mismatch is optimized for an operation point at $B = 10$ rad (and Gaussian 'red' edge), a behavior similar to the grey line in Fig. 6.14 is expected. Using cubicon formation, pulse energies $\sim 50 \mu\text{J}$ (after compression) have been obtained [94].

To summarize, appropriate GVD and TOD combinations of the stretcher-compressor-mismatch in nonlinear CPA-systems offer an increase in relative peak power over compensation with GVD only. The use of asymmetric spectra can enhance the compensation of SPM. However, this increases the complexity of the technique. In particular, a multi-dimensional optimization is required to find the point of optimal operation. An advantage of the methods of this section is that a fiber stretcher can be used. There is naturally a strong motivation to employ such a component when using fiber amplifiers. However, if a high-energy oscillator seeds the amplifier chain (e.g. to produce output pulses with energies at the mJ level), bulk stretchers are required. In any case, the performance is less than optimal (Strehl ratio is 0.75 at $B = 10$ rad for the example above) depending on the spectral shape. In the next sections, methods are presented which will allow for the production of (almost) transform limited pulses.

6.3 Perfect compensation of SPM using a parabolic spectrum

In this section, it is shown that the influence of nonlinearity in fiber-based CPA-systems can be controlled using active amplitude shaping. Applying a liquid-crystal spatial light modulator (SLM), the impact of the spectrum on the recompressed pulse quality is experimentally revealed. Compared to standard spectral shapes (such as Gauss or sech^2), a parabolic spectrum improves the pulse-quality at the output of a NLCPA-system [89]. In this way, control at a B-integral as high as 16 rad is demonstrated in a proof-of-principle experiment using an Yb-doped fiber-CPA-system.

In general, at the end of the amplifier of the NLCPA-system, the chirp of the strongly stretched pulse still corresponds to an one-point-to-point configuration between frequency and time, e.g. see Fig. 4.2. The modification of the chirp because of the nonlinear propagation is related to a spectral phase, which is given by $\varphi_{SPM} = B \cdot s(\Omega)$. The uncompressible part of this phase causes a degradation in peak-power with increasing B-integral, as shown in Fig. 4.4. However, if a parabolic spectrum is chosen, the chirp of the stretched pulse is still linear after nonlinear propagation. This is illustrated with Fig. 6.15. The spectral phase due to SPM can be exactly compensated using the positive dispersion due to the stretcher-compressor-mismatch. Fig. 6.16(c) shows a comparison of a sech^2 , a Gaussian and a parabolic spectrum in terms of output peak-power from a NLCPA-system. The Strehl-ratio of the best compression is plotted as a function of the B-integral. In the case of a parabolic spectrum, the Strehl-ratio remains unchanged even at high B-integrals. This behavior is a result of the perfect phase-compensation. It should be noted that there is an additional advantage: if a spectral window is given (e.g. the stretcher) in which the different spectra can fit, then a parabola can have a broader bandwidth compared to spectra such as Gauss or sech^2 , as shown in Fig. 6.16(a). The stretching implies a mapping of the spectrum into the time-domain, and thus, the stretched pulse of a parabolic spectrum will exhibit a lower peak-intensity compared to sech^2 or Gauss (at the same pulse-energy). This leads to a higher output pulse-energy at the same B-integral. For example, the enhancement is about 170% relative to a sech^2 -shape. However, the transform-limited pulse of the parabolic power-spectrum is related to a Bessel function of first kind (order $m=1$), which shows an infinite number of pre- and post-pulses (see Fig. 6.16(a)). Such satellite pulses are always present if the spectrum shows hard edges. This could be a disadvantage for some applications, e.g. in high-field physics.

Fig. 6.17 shows a schematic of the set-up which is used for the experimental demonstration. The master oscillator is a passively mode-locked Nd:glass laser delivering sech^2 pulses with durations of 180 fs (FWHM) at a center-wavelength of 1060 nm. The aver-

6.3 Perfect compensation of SPM using a parabolic spectrum

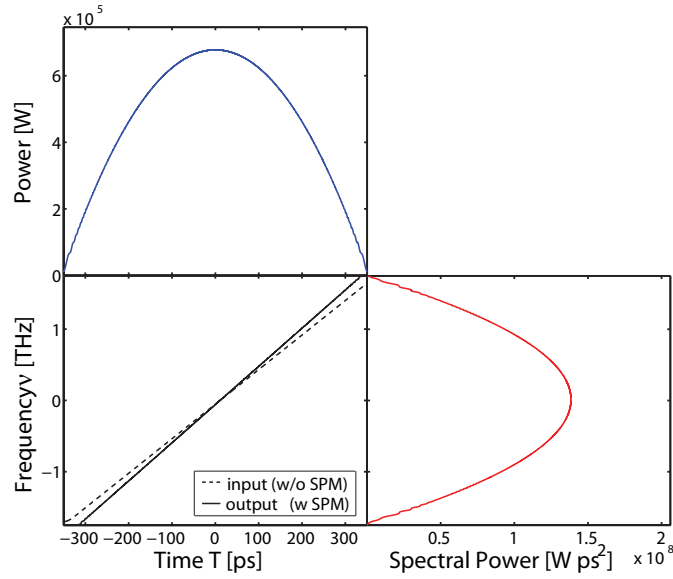


Figure 6.15: Impact of SPM on the chirp of a stretched pulse. The input spectrum is parabolic. The B-integral is $B=20$ rad. To emphasize the change of the chirp (solid line), the difference to the initial chirp (dashed line) is multiplied by 10.

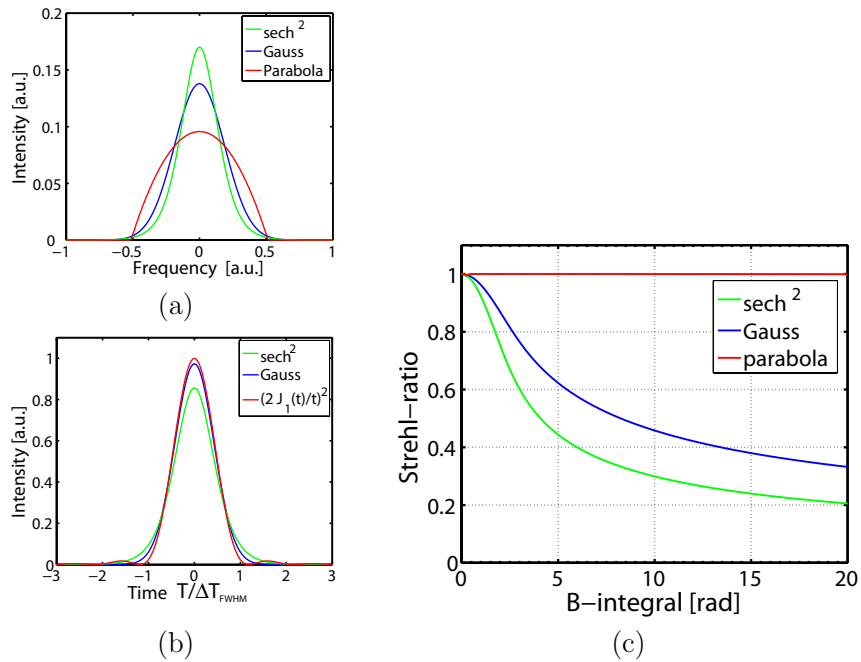


Figure 6.16: (a) Comparison of a Gaussian, sech^2 , and parabolic spectrum. (b) corresponding transform-limited pulses exhibiting the same FWHM. (c) Strehl-ratio as a function of the B-integral for the different spectra (SPM only compensated by a parabolic phase)

6.3 Perfect compensation of SPM using a parabolic spectrum

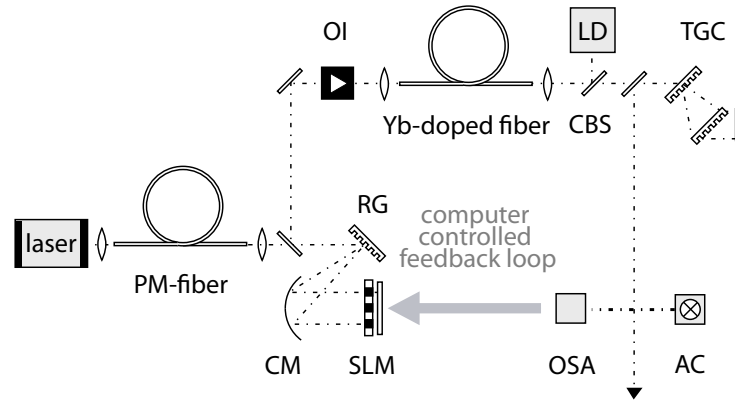


Figure 6.17: Schematic of the experimental set-up: PM-fiber, polarization-maintaining fiber; RG, reflection grating; CM, cylindrical mirror; SLM, spatial light modulator; OI, optical isolator; LD, laser-diode for pumping; CBS, chromatic beam-splitter; TGC, transmission grating compressor; OSA, optical spectrum analyzer; AC, autocorrelator

average power of the laser output is 100 mW at a repetition rate of 75 MHz. The output is coupled into 100 m length of passive polarization maintaining fiber (PM 980). The fiber serves two purposes. First, the pulses are spectrally broadened to about 40 nm (FWHM) in the initial section of the fiber, and second, the pulses experience temporal stretching to about 160 ps due to group-velocity dispersion. The coupling efficiency into the fiber is about 80%. A liquid crystal spatial light modulator (SLM) is set-up in a reflective configuration. In particular, at the reflection grating (1200 lpmm), the beam is spectrally fanned out, then a cylindrical focusing mirror ($f=0.3$ m) projects the spectral components onto a liquid crystal mask which is positioned in the Fourier plane. The mask comprises 640 stripes (each 100 μm wide and 1cm high). The light is reflected directly behind the mask by a mirror. The pulse-shaper can independently modify the phase and amplitude, but in the experiment, only the amplitude is shaped. An improved SLM setup is described in section 6.4. After passage through the pulse-shaper, the beam is steered into the fiber-amplifier. The amplifier is an Ytterbium-doped double cladding fiber with a core-diameter of 4 μm ($NA=0.17$) and a 400 μm D-shaped inner cladding ($NA=0.38$). The length of the fiber is 24 m, and the doping concentration is 7000 ppm. The long length and the small core-size of the fiber-amplifier were intentionally chosen in order to obtain high B-integral values at low average powers in this proof-of-principle experiment. The fiber-amplifier is pumped by a pig-tailed laser diode emitting radiation at a wavelength of 976 nm. The amplified pulses are recompressed by a pair of transmission gratings with a groove frequency of 1250 lpmm. The transmission through the grating-compressor (set up in double pass configuration) is about 80%. The spectra

6.3 Perfect compensation of SPM using a parabolic spectrum

of the pulses are recorded by an optical spectrum analyzer (OSA), and the temporal pulse-quality is monitored with an autocorrelator.

A computer is connected to both the OSA and the SLM. In an iterative procedure, the spectrum acquired by the OSA serves as a feedback signal for the calculation of a new transmission function at the SLM. In this way, a spectrum similar to the specified goal function, e.g. a parabola, is produced. Typically, about 20 iterations are sufficient. In particular, the difference between the measured spectrum and a least-squares fit of the goal function is used for the calculation of the new transmission function. The hands-off iterative routine is required since the gain of the fiber amplifier exhibits a spectral dependency. The spectrum is measured directly behind the fiber-amplifier. As the intensity of the pulse is the highest in the last section of the fiber-amplifier, the influence of SPM on the pulse propagation is the most dominant there, and thus, the shaping precisely affects the nonlinear evolution in the last part of the fiber-amplifier.

In the following, a Gaussian and parabolic spectrum are compared in terms of their impact on the pulse-quality at the output of the NLCPA system. The dependency of SPM on the spectrum of the chirped pulse is experimentally revealed.

At first, the spectrum at the output of the fiber-amplifier is shaped to a Gaussian shape with 10 nm bandwidth (FWHM). The center is at a wavelength of 1075 nm, a region which is favored by the spectrally dependent gain of the amplifier. The spectral broadening in the initial stage of the fiber-stretcher enables shaping in this spectral region. The spectrum generated at the end of the fiber amplifier is shown in Fig. 6.18(a). The temporal duration of the stretched pulse is 45 ps. This value has been obtained from the autocorrelation of the uncompressed pulse. After spectral amplitude shaping (applied transmission function allows only 20% of throughput) with the SLM unit (with an efficiency of $\sim 35\%$, e.g. due to gratings) there is an average power of 3 mW left for the (coupled) seed of the fiber-amplifier. Then, the amplifier is operated at low and high output powers by changing the pump-power while keeping the seed-power constant. The average power levels of the output are 250 mW and 1500 mW, respectively.

Assuming an exponential amplification of the pulse across the fiber, the B-integrals can be calculated from the power levels at the input and output, the temporal duration of the stretched pulse, as well as the estimated effective mode-field area. The impact of dispersion during amplification is neglected for the calculation. The low and high output powers correspond to B-integrals of 3.5 rad and 16 rad, respectively. Fig. 6.18(c) shows the autocorrelation measured for the recompressed pulses in the case of a Gaussian spectrum. In the experiment, the autocorrelations are optimized for shortest FWHM duration of the traces. The autocorrelation trace at a low output power (i.e., corre-

6.3 Perfect compensation of SPM using a parabolic spectrum

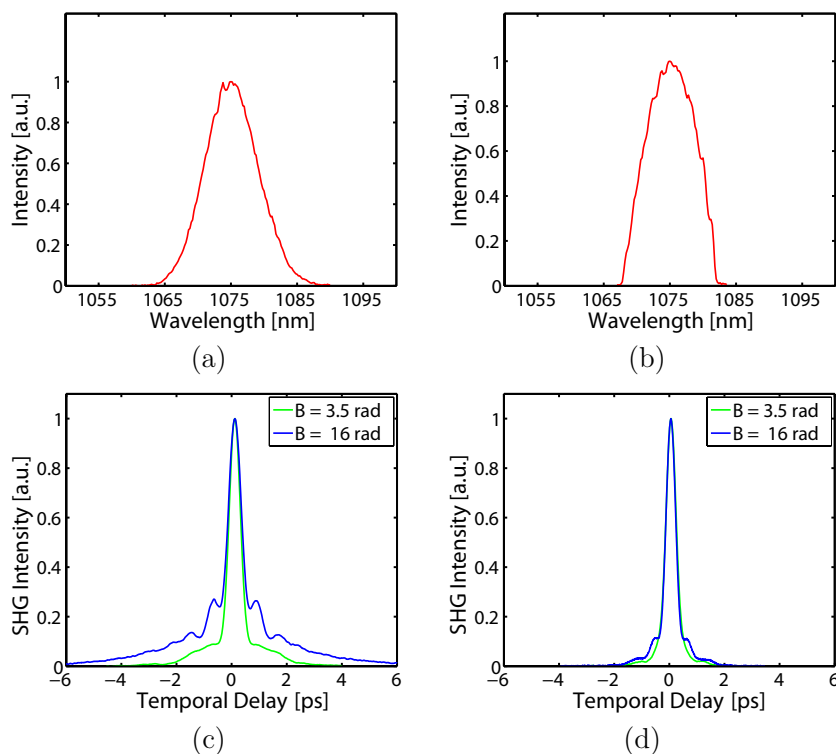


Figure 6.18: (a) Shaped Gaussian, and (b) parabolic spectrum with a FWHM of 10nm; (c) and (d) corresponding autocorrelations at low ($B = 3.5$ rad) and higher power ($B = 16$ rad). The FWHMs of the autocorrelations for the Gauss are 450 fs and 580 fs at low and high power levels, respectively. For the parabolic spectrum, the FWHMs are 420 fs and 410 fs at low and high power, respectively.

sponding to $B = 3.5$ rad) shows a minor pedestal which has its origin in uncompensated higher-order dispersion due to the fiber-stretcher-grating-compressor setup. It is also partly attributed to nonlinearity, which already has a minor influence at a B-integral of 3.5 rad. The initial spectral broadening in the fiber stretcher also introduces a small contribution to the phase-mismatch. The autocorrelation trace at higher output powers (i.e., corresponding to $B = 16$ rad) shows a considerable wing structure. The distance between the gratings of the compressor is optimized for best compression, i.e. the phase due to SPM is partially removed. The experiment demonstrates the degradation of output pulse-quality when common spectra are used. The principal behavior of the degradation of pulse quality is verified by numerical simulations of this fiber CPA-system, as shown in Fig. 6.19(c).

If a parabolic spectrum is produced at the end of the fiber-amplifier, as shown in Fig. 6.18(b), then the pulse-quality is preserved at high power levels, see Fig. 6.18(d). The

6.3 Perfect compensation of SPM using a parabolic spectrum

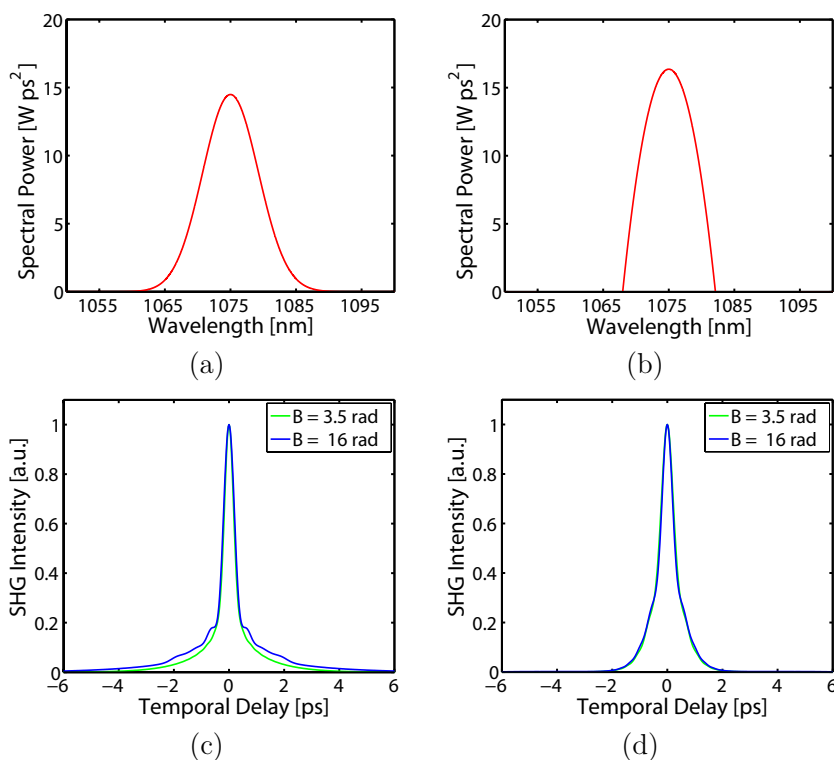


Figure 6.19: Numerical simulations of the experiment: (a) Gaussian, and (b) parabolic spectra centered at 1075 nm with a FWHM of 10 nm; (c) and (d) are the corresponding simulated autocorrelation traces of the experiment at low ($P=250\text{mW}$) and high power levels ($P=1500\text{mW}$) corresponding to B-integral of 3.5 rad and 16 rad. The input sech^2 pulses ($P=80\text{mW}$, $f=75\text{MHz}$, $\text{FWHM}=0.18\text{ ps}$) are spectrally and temporally broadened in the fiber-stretcher ($L=100\text{m}$, $(2)=0.025\text{ ps}^2/\text{m}$, $(3)=4 \times 10^{-5}\text{ ps}^3/\text{m}$, $n_2=2.7 \times 10^{-20}\text{ m}^2/\text{W}$, $\text{MFD} = 6.7\mu\text{m}$ (all values for 1060nm)), then the profiles of (a) and (b) are sliced with a power of 3 mW, the stretched pulses with duration of 40 ps are then amplified in an active fiber ($\text{MFD} = 4.7\mu\text{m}$, $L=24\text{ m}$, dispersion is not considered, and a 1250 lpmm grating compressor is implemented in a Littrow-configuration for the compression. For the Gaussian, the FWHMs of the autocorrelations (AC) are 450 fs (at $B = 3.5\text{ rad}$) and 500 fs (at $B=16\text{ rad}$). For the Parabola, the FWHM is about 500 fs ($B = 3.5\text{ rad}$, $B = 16\text{ rad}$).

parabola exhibits the same FWHM and center as the Gauss, and the same output power is obtained from the fiber-amplifier. A significant improvement of pulse quality is observed at a B-integral of 16 rad. It is worth noting that the spectra shown in Fig. 6.18 were recorded at the low B-integral. At $B = 16\text{ rad}$, the spectra showed modulations (depth $\sim 30\%$). The origin of these modulations is discussed in chapter 5. The pulse-contrast is estimated to be in the order of 10^{-3} .

Fig. 6.19(d) shows numerical data. The simulation verifies that third-order dispersion,

6.3 Perfect compensation of SPM using a parabolic spectrum

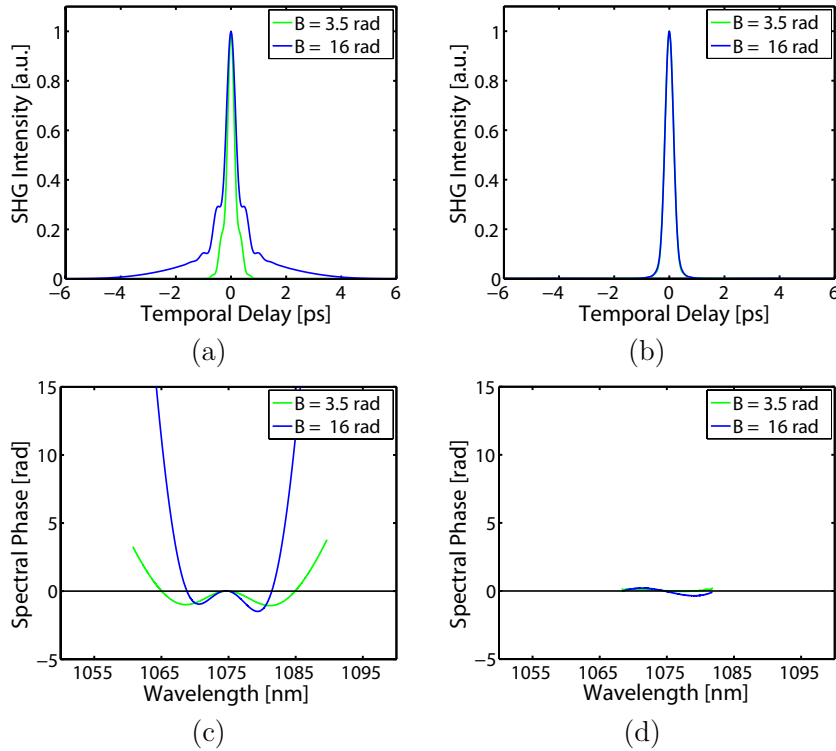


Figure 6.20: Numerical simulation of the autocorrelations when the outset are zero-phase spectra (Fig. 6.19(a) and (b) corresponding to 240 fs and 375 fs FWHM AC, respectively) and a grating-stretcher (1250 lpmm) instead of the fiber-stretcher (while obtaining the same temporal stretch), the results shown in (a) and (b) are obtained, respectively. For the Gaussian the FWHM AC increases from 290fs ($B = 3.5$ rad) to 440 fs ($B = 16$ rad). For a parabolic spectrum, the pulses can be recompressed the transform limit (FWHM AC = 375 fs) for both B-integrals. (c) and (d): simulation of the spectral phases at the output of the CPA-system corresponding to a Gaussian-spectrum, and a parabolic spectrum, respectively.

inherent in this fiber-stretcher-grating-compressor configuration, precludes the generation of transform-limited pulses. If a bulk grating-stretcher is used instead of the fiber, then the anticipated autocorrelations are shown in Fig. 6.20. Fig. 6.20(c) and (d) demonstrate the residual spectral phases after best compression. In the case of a Gaussian spectrum, the strong residual spectral phase is responsible for the degradation of pulse-contrast. To obtain transform-limited output pulses, the Gaussian profile would require phase-shaping. As can be seen Fig. 6.20(d), such a strong spectral phase-modulation is not given in the case of a parabolic spectrum. Consequently, the autocorrelation is also good at a high B-integral, as shown in Fig. 6.20(b)

The phase of the stretcher and compressor is not parabolic, but also exhibits higher order dispersion. In particular, third-order dispersion is introduced by the change of

6.3 Perfect compensation of SPM using a parabolic spectrum

the grating separation distance to compensate SPM. However, the magnitude is small compared to the magnitude of the overall phase. Fig. 6.20(d) shows clearly that its influence on the recompressed pulse is small. In principle, a shape that deviates from a pure parabola could induce a nonlinear phase which accounts for this third-order term. However, as the magnitude of this phase-mismatch is small, it is probably more reasonable to compensate for it by active phase-shaping. Other small residual phases, e.g. due to a stretcher-compressor-mismatch, could be also tackled via this approach.

To summarize, the control of SPM in a fiber CPA-system has been demonstrated by using active spectral amplitude shaping. Previously, nearly parabolic pulses were produced using a master oscillator operated in the similariton regime [47]. Compared to such an approach, the pulse-shaper offers flexibility. In particular, spectral shaping in the stretcher (e.g. due to spectral efficiency of the grating), pre-amplifiers or any other component before the main amplifier can be addressed. In this way, a parabolic pulse shape is obtained right at the point where SPM acts, rather than at the beginning of an amplifier chain. Furthermore, different spectral shapes have been experimentally generated and compared in terms of their impact on the output pulse-quality. It has been shown that the nonlinear phase resulting from a parabolic spectrum can be efficiently removed by adjusting the grating compressor. Moreover, control at a B-integral as high as 16 rad has been demonstrated.

6.4 Perfect compensation of SPM using phase-shaping

In the previous sections, the amplitude of the pulse has been shaped to control the impact of SPM in fiber CPA-systems. In this section, phase-only pulse-shaping is demonstrated experimentally as an alternative.

In general, phase-shaping requires the exact determination of the residual phase. However, phase-measurements using SPIDER require broad spectra in order to accurately determine complex phases from the spectral interference. On the other hand, frequency resolved optical gating (FROG) includes time-consuming retrieval algorithms, which tend to fail in the case of complex phases. Recently, adaptive phase-compensation using SHG-feedback was implemented in a fiber CPA-system [95] (and references therein). The method is sensitive to noise on the feed-back signal, as well as time-consuming. However, the nonlinearity of the system poses the main challenge: a small incorrect phase-modulation can result in satellite pulses [79].

The SPM accumulated in a CPA-system can be canceled using a semiconductor with a negative n_2 [96]. The main drawbacks are the amount of B-integral which can be compensated, typically, ~ 1 rad, and the high losses (e.g., two photon absorption). A LiNbO₃ electro-optic phase modulator and a RF waveform synthesis technique were used to compensate SPM in the time domain by emulating a negative n_2 [97]. However, the electro-optic modulator required small input pulse energies, typically < 1 nJ, and the maximum phase shift was limited to 2π . Furthermore, the effectiveness of the method depends on the shape of the pulse. A more general use of the method would require more than two RF frequencies in order to improve the matching of the electrical and temporal waveforms, however, this demands an adaptive scheme which increases the complexity of the electronics and the method in general.

In the following, SPM in a fiber-based CPA-system is compensated by a simple phase-shaping technique in the frequency domain. The method is based on the analytical expression for the spectral phase due to SPM in a CPA-system (see section 4.1). A pulse-shaper produces the opposite phase, and thus compensates the SPM accumulated during amplification. It is worth noting that the compensation of SPM by a linear phase has already been theoretically proposed in [98]. Here, the implementation is demonstrated in a real world fiber CPA-system which produces pulse-energies around 1 mJ. Nearly transform-limited pulses are generated at B-integrals up to 10 rad, where the B-integral is determined by the phase-compensation method itself. The method relies neither on complex phase-measurements nor on time-consuming optimization routines.

Design of the 4-f zero-dispersion stretcher for the SLM

In the experiment, the pulse shaper is a spatial light modulator (SLM). The device (Jenoptik SLM-S640d) consists of two liquid crystal (LC) displays, and permits independent control of the amplitude and the phase. This mask is placed in the Fourier-plane of a 4-f zero-dispersion stretcher. Fig. 6.21 shows a schematic of the experimental setup. The degrees of freedom in the design are the focus length f of the cylindrical mirror (used instead of lenses to minimize dispersion inherent in the setup) and the grating parameters (groove frequency d , angle of incidence α). The fan out of spectral components and the (vertical) beam waist must be matched to the mask dimensions (width $M = 64 \text{ mm} \hat{=} 3\Delta\omega_{\text{FWHM}}$, height $= 10 \text{ mm} \hat{=} 2w_{in}$, where w_{in} is the $1/e$ size of the input beam). Aside from the grating equation, $\sin(\alpha) + \sin(\beta) = m\lambda d$ with diffraction angle $\beta(\omega)$, there are two constraints [58]: the spectral coverage of the SLM according to $\text{atan}((M/2)/f) = |\beta(\omega_0 + \frac{3}{2}\Delta\omega) - \beta(\omega_0 - \frac{3}{2}\Delta\omega)|/2$, and the condition $\text{atan}(M/r) = |\alpha - \beta(\omega_0)|$, which prevents blocking of the incident beam by optical components, with M being the distance from the optical axis at position $r = (2/3)f$ before the grating, see Fig. 6.21. The solution of this set of nonlinear equations is presented in Fig. 6.22(a). Each dispersed frequency component incident on the discrete mask is associated with a certain beam size. The focal length is determined by the (horizontal) beam waist in the focus $2w_0 = (\cos(\alpha)/\cos(\beta)) \cdot 2\lambda f/(\pi w_{in})$, as well as the double Rayleigh length $2\rho_0 = 2w_0^2\pi/\lambda$, which has to be longer than the mask depth ($\sim 6 \text{ mm}$), so that the phase fronts are plane during passage. To exploit the spatial resolution of the mask, the frequency components should be focused to a spot size comparable with or less than the pixel size w (here $100 \mu\text{m}$). If the spot size is too small, replica waveforms of the output pulse arise from discrete features of the mask (i.e. discrete Fourier sampling) [99]. If the spot size is too large, diffraction effects occur and result in a space-time-profile of the shaped waveform. An estimate of the temporal spacing of the replicas is $\tau = 2\pi a/w$, and a describes the linear dispersion of frequencies across the mask ($x = a \cdot \Omega$). For the present design, $\tau \sim 100 \text{ ps}$. However, the finite spot size attenuates the magnitudes of the replicas [99]. At the same frequency $1/\tau$, the interpixel gap reproduces the input pulse as replica waveforms (at time zero) with a reduced amplitude (proportional to the ratio of gap size and pixel size, here 3%). Fig. 6.22(b) shows the spot size and Rayleigh zone as a function of the focal length, using the parameter configuration shown in Fig. 6.22(a), where the dashed lines mark the two constraints. Thus, for the following experiments a 40 cm focal length and a 1800 lpmm grating were chosen.

6.4 Perfect compensation of SPM using phase-shaping

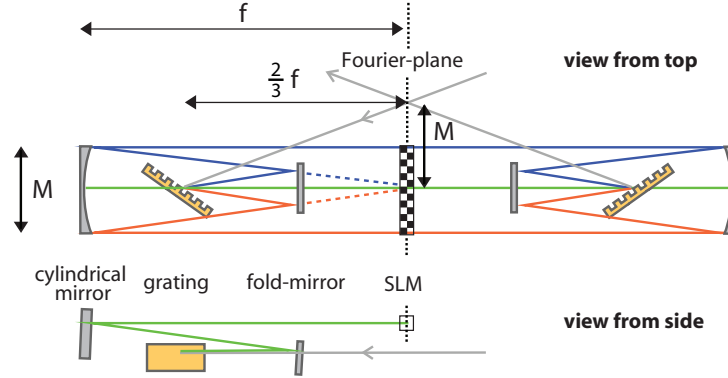


Figure 6.21: Schematic of the 4-f zero-dispersion stretcher for the SLM.

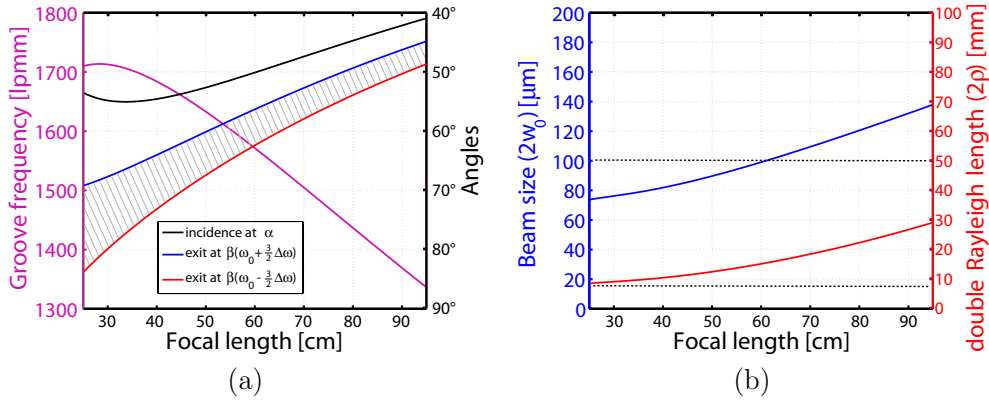


Figure 6.22: (a) Focal-length and groove frequency combination for the SLM-S640d. The central wavelength is 1035 nm and the bandwidth $\Delta\lambda_{FWHM}$ is 11.5 nm. (b) spot size and double Rayleigh length as a function of focal length f for an input beam size of $w_{in} = 5$ mm.

Principles of the method

According to the analytical model of a nonlinear CPA-system, Eq. (4.6), the stretched ultrafast pulse acquires a spectral phase during nonlinear propagation, which can be approximated by $\varphi_{SPM} = B \cdot s(\Omega)$.

For the phase-shaping experiment, the stretcher and compressor are adjusted in linear operation. This match is kept for the nonlinear regime of the CPA-system. Thus, at the output of this system the residual spectral phase due to SPM is given by φ_{SPM} . Nearly transform-limited pulses can be produced when the pulse-shaper generates the phase $\varphi_{ps}^* = -B \cdot s(\Omega)$. The technique only requires the measurement of the spectrum $s(\Omega)$. However, the exact value of the B-integral is unknown. So, in practice, the phase $\varphi_{ps} = \Delta\phi \cdot s(\Omega)$ is generated with the pulse-shaper, and the parameter $\Delta\phi$ is varied (at fixed average power levels). Simultaneously, the autocorrelation is monitored at the output.

6.4 Perfect compensation of SPM using phase-shaping

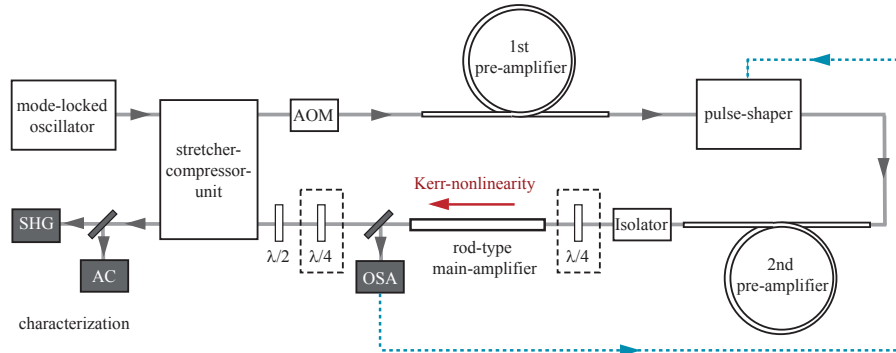


Figure 6.23: Schematic of the experimental setup of the fiber CPA-system with a pulse-shaper for phase-only shaping. AOM, acousto-optical modulator; OSA, optical spectrum analyzer; SHG, second harmonic stage; AC, autocorrelator.

If $(-\Delta\phi)$ agrees with the B-integral, then the (normalized) autocorrelation corresponds to the autocorrelation of the linear CPA-system. In this way, nearly transform-limited pulses are experimentally produced from a nonlinear CPA-system, and the B-integral can be accurately determined.

Experiment and results

This method is implemented in a high-energy fiber-based CPA-system. The schematic of the setup is shown in Fig. 6.23. The main components are an oscillator, a stretcher, an acousto-optical modulator (AOM), a first pre-amplifier, a pulse-shaper, a second pre-amplifier, a main amplifier, and a compressor. The soliton-laser emits pulses with a spectral bandwidth of 3 nm (FWHM) at a repetition rate of 10 MHz and an average power of 3.5 W. The stretcher-compressor unit employs two 1740 lpmm dielectric diffraction gratings. The compressor efficiency is 70%. The quartz-based AOM reduces the repetition rate to 50 kHz. The first amplifier is 1.2 m-length bendable photonic crystal fiber ('crystal fibre 200/40') with a mode-field diameter (MFD) of 33 μm . The pulse-shaper is the spatial light modulator (SLM) described above. In the experiment, only the phase is modified. At a wavelength around 1 μm , the maximum producible phase-shift (without phase-wrapping) is about 9 rad. The first preamplifier raises the average power after pulse-picking in order to compensate for the moderate efficiency ($\sim 30\%$) of the 4-f zero dispersion stretcher. A substitution of the gold-coated diffraction gratings by high-efficiency dielectric diffraction gratings will render the first pre-amplifier redundant. With the present implementation, a seed of ~ 4 mW is launched into the second pre-amplifier. The second pre-amplifier is a 1.3 m-length PCF ('crystal fibre

6.4 Perfect compensation of SPM using phase-shaping

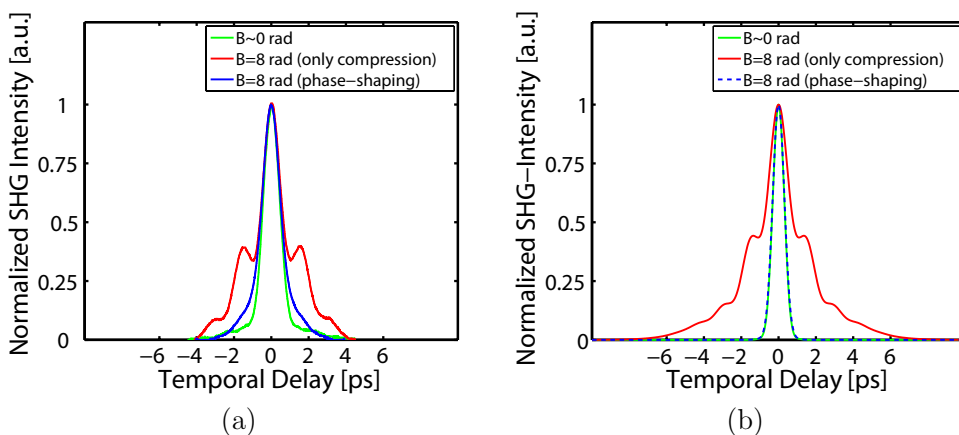


Figure 6.24: (a) Normalized autocorrelation traces measured at $B=0$ rad (green), and at $B=8$ rad with phase-shaping (blue) and without phase-shaping but with an adjustment of the compressor grating separation (red curve). (b) simulated autocorrelations, where only the parabolic phase is adjusted to achieve the best compression (in terms of highest Strehl-ratio), and the spectrum is according to the data required for the phase shown in Fig. 6.25.

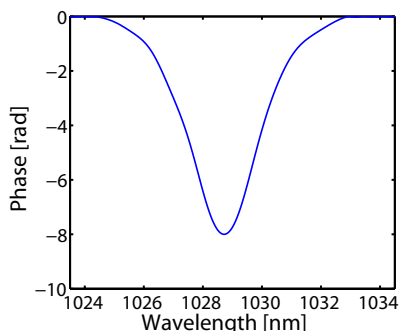


Figure 6.25: Spectral phase produced by the spatial light modulator at $B=8$ rad.

200/40') with a MFD of $33 \mu\text{m}$. The main amplifier is 1.2 m-length of rod-type PCF ('crystal fibre 200/85') with a MFD of $71 \mu\text{m}$. An average power of 300 mW is launched into the main-amplifier. The pulse acquires SPM only in the main amplifier. To keep the nonlinear refraction coefficient n_2 , and thus the B-integral, as low as possible, the light is circularly polarized (see section 6.5). During amplification, the stretched pulses exhibit a bandwidth of 2.6 nm (RMS) and their duration was measured to be 1.4 ns. The spectrum is measured behind the main amplifier using an optical spectrum analyzer (OSA). A computer reads out the data and calculates the phase φ_{ps} for the SLM. The output pulse is monitored with an autocorrelator.

At first, the system is operated at low output power. To obtain nearly transform-limited pulses at the output of this linear CPA-system, the stretcher and compressor are matched. In Fig. 6.24(a) the corresponding autocorrelation is shown (green curve). Its

6.4 Perfect compensation of SPM using phase-shaping

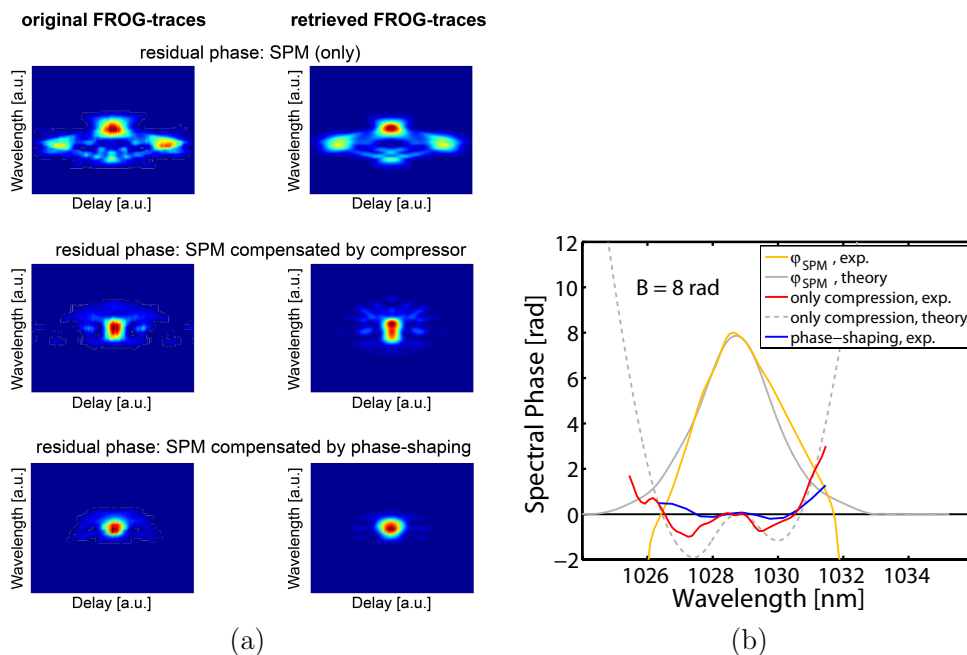


Figure 6.26: (a) FROG-traces, (b) and corresponding retrieved residual phases at $B=8$ rad.

FWHM-width is 1.2 ps. The pulses are close to the transform limit.

Then, the output power of the main-amplifier is increased to 60W, according to a pulse-energy of 1.2 mJ (before compression). The phase φ_{ps} is produced by the pulse-shaper. By variation of the parameter $\Delta\phi$ the B-integral is determined to be 8 rad. As a result, the phase φ_{ps}^* (which compensates SPM) is produced, and it is shown in Fig. 6.25. In Fig. 6.24(a) the corresponding autocorrelation (blue curve) can be seen. It agrees well with the one at low output powers. Thus, nearly transform-limited pulses are produced from a nonlinear CPA-system at $B = 8$ rad. Fig. 6.24(a) also shows the autocorrelation in the case of partial SPM-compensation with a stretcher-compressor-mismatch (red curve), and the pulse-shaper turned off, $\varphi_{ps} = \text{const}$. The pulse quality is degraded and shows a strong wing structure. The FWHM of the autocorrelation increases to about 1.4 ps. To evaluate the effective peak-power, Fig. 6.16 can be used: at $B = 8$ rad, the Strehl-ratio of a conventional nonlinear CPA-system is below 50%. Thus, the implemented phase-shaping at $B = 8$ rad enhances the effective peak-power by a factor of approximately 2. Using the spectral shape, the experimental results can be simulated with the model of section 4.1. Fig. 6.24(b) verifies the principal behavior. However, in the case of an adapted compressor, the features of the experimental autocorrelation are less pronounced. This is attributed to residual phase, e.g. due to cubic stretcher-compressor-mismatch, and the experimental determination of 'best compression'.

6.4 Perfect compensation of SPM using phase-shaping

Although a phase-measurement is not required for the actual phase-compensation technique, frequency resolved optical gating (FROG) verifies the impact of the method. In the case of a perfect stretcher-compressor-match (for the linear system) and operation of the CPA-system at $B = 8$ rad, the retrieved phases before and after phase-shaping are shown in Fig. 6.26. Before phase-shaping, large phase-shifts are given (orange curve in Fig. 6.26(b)). The theoretically expected residual phase is φ_{SPM} . However, the experimentally determined phase differs from the theoretical phase (grey curve) at the edges of the spectrum. It is assumed that this originates from the FROG retrieval algorithm, which uses the intensity distribution to determine the error. Due to this uncertainty of the retrieved phase, pulse-quality improvement is only achieved by phase-shaping using $\varphi_{ps}^* = -B \cdot s(\Omega)$. After the application of this model-based approach, the retrieved phase shows a reduction of phase-shifts (blue curve). For the common case where the spectral phase due to SPM is compensated by a parabolic phase due to a stretcher-compressor mismatch, Fig. 6.26 shows the retrieved phase from the FROG-measurement as well as the corresponding theoretical phase. The latter is obtained by using φ_{SPM} and looking for the highest Strehl-ratio by varying the amount of parabolic phase.

In summary, SPM has been successfully controlled in a fiber CPA-system at the mJ-level using phase-only pulse-shaping. Nearly transform-limited pulses are produced at a B-integral of 8 rad. The pulse energy is $840 \mu\text{J}$ (after compression) and the pulse duration is ~ 780 fs. This result constitutes a considerable improvement compared to the system described in [76]. The pulse-quality could be improved in a reproducible manner. In particular, the Strehl-ratio is increased by a factor of about 2. The method requires only the measurement of the spectrum. This model-based method is fast and easy to implement. However, the technique relies on robust single mode operation (to measure the correct spectrum and not an interference), and it also requires a constant spectrum during the action of SPM. Although saturation did not change the spectrum in this experiment, modifications may be challenging in other situations. An empirical parameter (e.g., scaling the measured spectrum) could account for gain shaping. Compared to the amplitude shaping, phase-shaping has a negligible impact on the dynamics of the laser-amplification, which is strongly affected by the signal intensity (that is modified by amplitude shaping). However, it is advantageous to combine phase and amplitude shaping. As mentioned in section 6.3 already, a flat spectrum exhibiting less energy in the edges can result in a lower B-integral at the same energy. Amplitude shaping could produce such a shape, phase-shaping is then carried out to produce transform-limited pulses.

6.5 Peak-power scaling by using circularly polarized light

In section 3.3.1 it has already been theoretically shown that the nonlinear refraction coefficients of circularly and linearly polarized light differ. Accordingly, in a fiber CPA-system the two polarization states will result in different B-integrals. In the following, it is experimentally demonstrated that circularly polarized light is advantageous if the Kerr-effect has to be minimized during nonlinear amplification in optically isotropic gain media, such as fused silica or YAG. The technique can be employed in large mode area fibers of short-length, which must be non-polarization maintaining and non-polarizing. It has been verified by numerical simulations that the impact of birefringence is negligible in such LMA-PCFs since the beat-length is typically at least an order of magnitude longer than the actual fiber length (~ 1 m).

The optical Kerr-effect decreases the peak-power at the output of nonlinear CPA-systems. In particular, the performance (i.e. the Strehl-ratio) is a function of the B-integral. In turn, the B-integral depends on the nonlinear refraction coefficient n_2 . The state of polarization influences the magnitude of this parameter. Specifically, the nonlinear refraction coefficient of circularly polarized light is reduced by a factor of $2/3$ compared to linearly polarized light. The corresponding B-integrals are reduced likewise. In the case of an initial sech^2 pulse, Fig. 6.27(a) shows the decrease in performance (in terms of the Strehl-ratio) as a function of the B-integral. The curves are identical for linearly and circularly polarized light, however, in the case of circularly polarized light, the data refers to the upper B-integral axis, which is scaled by a factor of $2/3$ compared to the lower axis. The factor $2/3$ corresponds to the ratio $(n_{2,C}/n_{2,L})$. Thus, the use of circularly polarized light instead of linearly polarized light should yield a peak-power enhancement as shown in Fig. 6.27(b). This increase in peak-power is dependent on the pulse-shape, and therefore, the sech^2 pulse is compared to a Gaussian shape. A Gauss pulse allocates less energy to the regions far from the center (i.e., lower kurtosis), and thus, the compensation of SPM with a parabolic phase yields higher peak-powers. Consequently, the relative peak-power enhancement is diminished. In any case, circularly polarized light will increase the self-focusing threshold.

In the following, the ratio of the B-integrals, corresponding to amplification with linearly and circularly polarized light, is experimentally measured using phase shaping. For this purpose, a pulse-shaper is inserted into a fiber-based CPA-system. In particular, the stretcher and compressor are perfectly matched in the linear operation of the CPA-system. This configuration is kept for the nonlinear regime of the CPA-system. For such a configuration, the residual spectral phase due to self-phase modulation is given by $B \cdot s(\Omega)$.

6.5 Peak-power scaling by using circularly polarized light

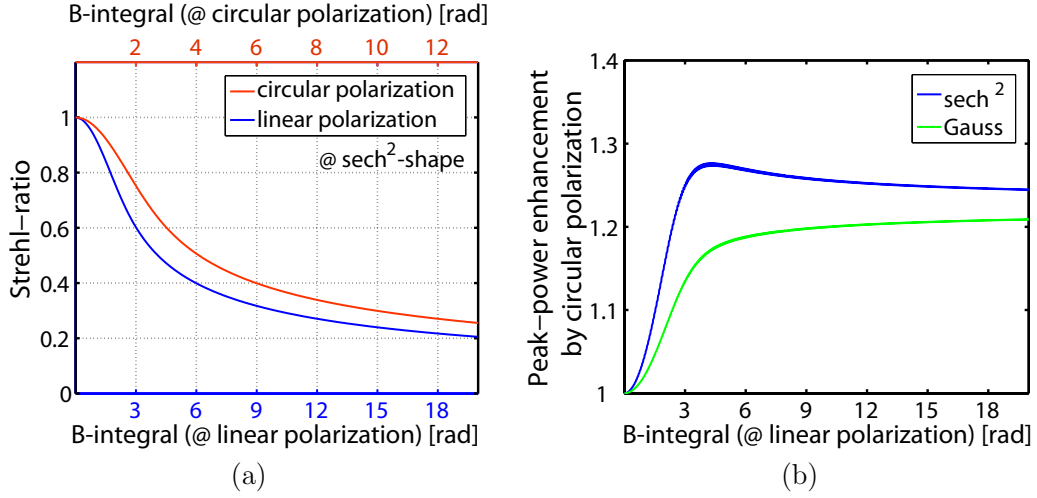


Figure 6.27: (a) Strehl-ratio of the output pulse after nonlinear chirped pulse amplification as a function of the B-integral. (b) Relative peak-power enhancement if circularly polarized light is used instead of linearly polarized light for different pulse shapes.

The B-integral is determined by phase-only shaping. Nearly transform-limited pulses can be produced when a pulse-shaper generates a phase $\varphi_{ps} = -B \cdot s(\Omega)$. The spectrum $s(\Omega)$ is obtained with an optical spectrum analyzer, however, the exact value of the B-integral is unknown. So, in practice, the phase $\varphi_{ps} = \Delta\phi \cdot s(\Omega)$ is generated with the pulse-shaper, and the parameter $\Delta\phi$ is varied. For the different values of $\Delta\phi$, and thus, different phase-shapes realized with the pulse-shaper, the pulse-energy at the input of the amplifier is kept constant, and as a consequence, the output pulse-energy remains the same. In particular, the growth of energy is independent of the pulse-shape [24]. By analogy with the procedure described in the previous section, the B-integral is the $(-\Delta\phi)$ for which the (normalized) autocorrelation corresponds to the autocorrelation of the linear CPA-system. In this way, the B-integrals for the two polarization states can be accurately determined.

The experimental setup is the same as in section 6.4. A schematic of the fiber-based CPA-system has already been shown in Fig. 6.23. To amplify circularly polarized light, a quarter-wave plate is placed before the main-amplifier. At this position, the states of polarizations are measured with a polarimeter. The results are shown in Fig. 6.28. The state of polarization can be represented by an ellipse [100]. The parameter ellipticity is an angle, which is calculated from the arc tangent of the ratio of the semi-minor to the semi-major axis. For the case of circularly polarized light, the ellipticity of the state of polarization is measured to be 43° , and for linearly polarized light it is experimentally

6.5 Peak-power scaling by using circularly polarized light

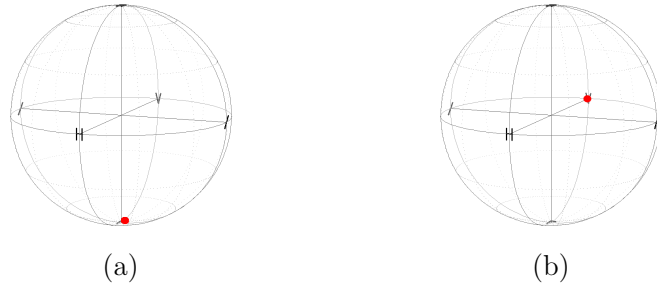


Figure 6.28: Results from the measurement with the polarimeter: representation of the state of polarization on the Poincaré-sphere for the case of circularly polarized light (a), and linearly polarized light (b).

determined to be 0.3° . After the main amplifier the circular polarization is changed to linear polarization with a second quarter-wave plate. For both polarization states, a half-wave plate is used to achieve the 70% efficiency of the compressor. Nonlinear polarization rotation is not an issue. Particularly, the gratings of the compressor are polarization sensitive, and thus nonlinear polarization rotation would cause a drop in compressor efficiency. However, it is experimentally observed that the compressor efficiency is the same for the nonlinear and linear regime of the CPA-system. For both polarization states, 70 mW of average power is launched into the main amplifier at a repetition rate of 50 kHz, and the output power is 31 W (before compression), which is a pulse-energy of $620 \mu\text{J}$. The nonlinearity is solely accumulated in the main amplifier since only moderate pulse energies are extracted from the pre-amplifiers, which feature large-mode areas. The spectrum is measured behind the main amplifier and is shown in Fig. 6.29(a). The spectrum is normalized (i.e., the peak equals 1) and multiplied by the phase-compensation parameter $\Delta\phi$. In the experiment, the parameter $\Delta\phi$ is varied between 0 and -9 rad. The resulting spectral phases, which are produced by the SLM, are shown in Fig. 6.29(b). To facilitate inspection, the step-size in the figure is 1 rad. In the experiment, the actual step is 0.5 rad. For the case of circularly polarized light, the step is refined to 0.25 rad in the region of -4 rad. For linearly polarized light, the steps are reduced to 0.25 rad around $\Delta\phi = -6$ rad. For each $\Delta\phi$, the autocorrelation traces are measured at the output of the nonlinear CPA-system. To minimize the error of the measurement, the sweep of the parameter $\Delta\phi$ is repeated three times for the circular polarization, and two times for linear polarization.

For the case of circularly polarized light, one set of autocorrelation traces is shown in Fig. 6.29(c). Again, only steps of 1 rad are shown. The (average) 'ridge' of the three sets of autocorrelations (full resolution) is shown via the blue line in Fig. 6.29(c). The

6.5 Peak-power scaling by using circularly polarized light

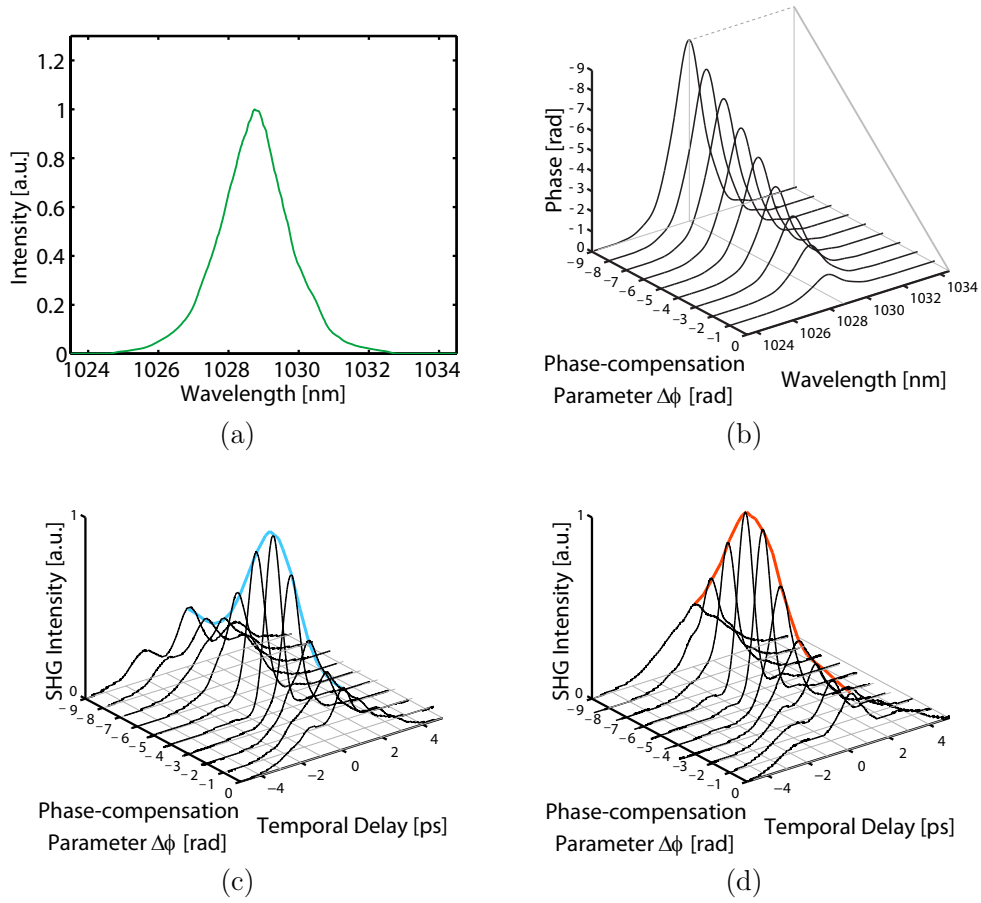


Figure 6.29: (a) The spectrum measured at the output of the main-amplifier. (b) The SLM produces phases with different values of the phase-compensation parameter $\Delta\phi$. The autocorrelation traces measured at the output of the fiber CPA-system for the different $\Delta\phi$: (c) for circularly polarized light and (d) linearly polarized light.

autocorrelation trace with maximum peak agrees with the (normalized) autocorrelation trace that was recorded for the linear system, i.e. nearly transform-limited pulses are produced at this point. Thus, at the maximum peak the absolute value of the phase-compensation parameter equals the B-integral, i.e. $\Delta\phi = -B$. For the case of circularly polarized light, the B-integral is 4.0 rad. The precision is limited by the step-size of 0.25 rad. However, a finer step-size does not improve the measurement because of fluctuations in the autocorrelation traces.

The case of linearly polarized light is shown in Fig. 6.29(d). The B-integral is determined to be 5.8 rad. To better compare the results for the two states of polarization, both sets are shown in Fig. 6.30. The ratio of the B-integrals is found to be in good

6.5 Peak-power scaling by using circularly polarized light

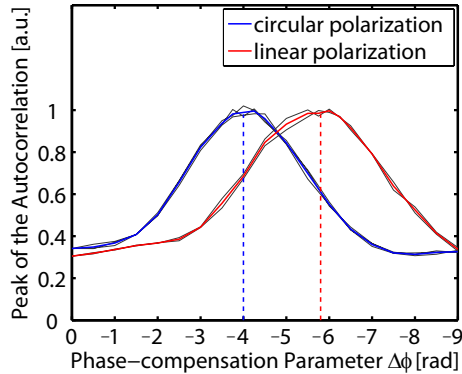


Figure 6.30: Peak of the autocorrelation traces at the output of the fiber CPA-system for the different values of the phase-compensation parameter $\Delta\phi$. The blueish and redish line correspond to linearly and circularly polarized light, respectively. They represent the mean values of the experimental data (grey curves). The vertical lines mark the position of $\Delta\phi = -B$.

agreement with the theoretical value of $2/3$. It can be seen that the maximum is not a sharp peak but a rather smooth curve. Thus, small fluctuations have a strong impact on the exact determination of the ratio of the B-integrals. Nevertheless, the result of Fig. 6.30 shows that circular polarization is advantageous in ultrafast fiber amplifiers.

To summarize, in addition to the technique of chirped pulse amplification and the use of large mode area fibers, the strength of the Kerr-effect has been further reduced by using circularly polarized light instead of linearly polarized light. Using phase-shaping, the ratio of the B-integrals of circular versus linear polarization has been measured to be around $2/3$, which is in accord with theoretical findings. The technique requires an optically isotropic gain medium. The method can be used to increase the peak-power from ultrafast oscillators, and to reduce the impact of modulation instability in twisted-mode resonators. The technique is particularly relevant for ultrafast fiber-systems, which are susceptible to nonlinear effects. It can be combined with techniques that control SPM by using active pulse-shaping. In particular, the requirements on the shaping dynamics can be reduced. In this context, the application of polarization maintaining as well as polarizing fibers seems not ideal for peak-power scaling. In general, the beat-length due to birefringence must be longer compared to the fiber-length. Moreover, the use of circularly polarized light increases the self-focusing threshold (e.g., [49]) from 4 MW to about 6 MW (at a wavelength around $1.03 \mu\text{m}$).

6.6 Comparison of techniques

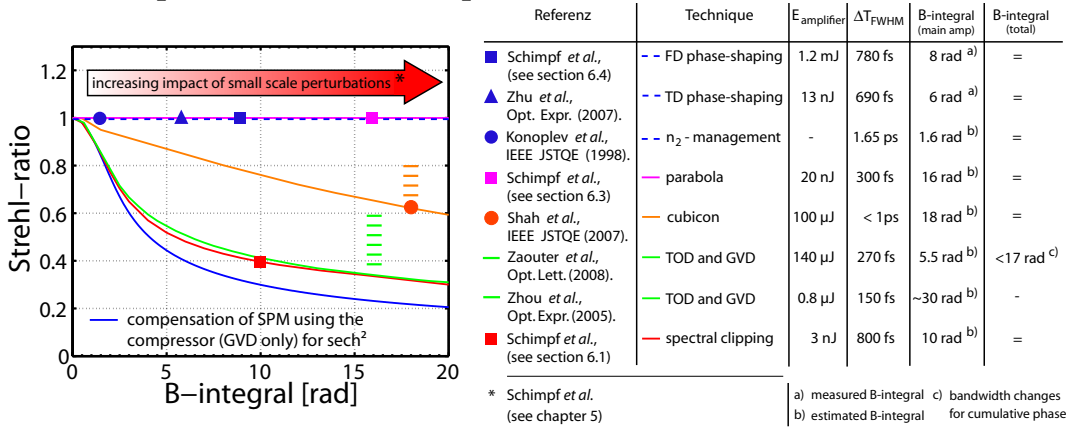


Figure 6.31: Comparison of the methods to control the impact of SPM in fiber CPA-systems.

Fig. 6.31 compares the methods discussed in this chapter in terms of preservation of pulse-quality, as well as output parameters. With the exception of the cubicon (orange line) and parabola (magenta line), the simulations have assumed a sech^2 spectrum. The calculations are based on the analytical model developed in section 4.1. Experimental demonstrations of these methods are marked on the theoretical curves (although in practice there will be deviations from the theoretical behavior). Using spectral clipping in the stretcher, pulse quality improvement has been demonstrated at $B = 10$ rad. This method exhibits a behavior comparable to the method using adaptation of both GVD and TOD. High energy pulses have been obtained by Zaouter *et al.*. However, in this experiment the final spectrum has narrowed, and it is free of a pronounced wing-structure [91], and thus the SPM accumulated in the pre-amplifiers ($B \sim 12$ rad) can be well compensated. If the spectral shape changes, the performance will alter (see also Fig. 6.12). This variability is indicated by the (green) dashed bar. Cubicon formation in a (nearly) all fiber CPA-system has enabled ultrashort 50 μ J pulses (after compression). Active pulse shaping offers flexibility and a good preservation of pulse-quality. Both amplitude and phase shaping have been pursued in this work. In particular, the impact of SPM at $B = 16$ rad has been controlled by generating a parabolic spectrum, and model-based phase-shaping has produced high quality pulses with energies around 1 mJ, which is the record. The B-integral can be exactly measured. In contrast to prior time-domain phase-shaping (emulating a negative n_2), this method modifies the phase in the frequency domain. All methods can benefit from the use of circularly polarized light to lower the B-integral. This technique has been proposed in section 6.5. Furthermore, in all experiments a smooth envelope of the spectrum (or pulse) has been assumed. As discussed in chapter 5, perturbations limit the nonlinear operation regime.

7 Conclusion and Outlook

The rapid development of ultrashort pulse fiber lasers has brought the field to the point where ultrafast sources for particular industrial and scientific applications are commercially available. To further broaden the scope of this technology, there is currently considerable interest in the development of the next generation of fiber lasers exhibiting higher pulse energies and peak-powers. Saturation and nonlinear effects constitute the main challenges in the design of such systems. The goal of this thesis was to control the impact of these limiting processes by applying pulse shaping, and thus, to overcome the drawbacks.

Conventionally, nonlinear effects during the amplification of ultrashort pulses must be avoided in order to obtain a high pulse quality, and thus, high peak-power. For this reason, the technique of chirped pulse amplification, and large mode area fibers are employed in fiber-based amplification systems. Even though these methods are implemented in state-of-the-art ultrashort pulse fiber amplifiers, energy scaling is still limited by nonlinear effects. In particular, the pulse quality rapidly degrades with an increasing impact of nonlinearity. To improve the quality of the output pulses, novel concepts must be developed that control the impact of nonlinearity, and therefore, enable further scaling of the pulse energy.

One objective of this thesis was the development of an analytical model for the ultrashort pulse propagation in nonlinear fiber-based CPA-systems. It could be shown that the impact of self-phase modulation on the stretched pulse can be approximated by a spectral phase which exhibits the shape of the power spectrum and a maximum phase-shift according to the B-integral. This model has significantly simplified the analysis of nonlinear CPA-systems. A direct consequence of this analysis was the experimental demonstration of the compensation of self-phase modulation by positive dispersion. At this point, it is worth noting that negative dispersion is conventionally associated with the cancelation of self-phase modulation. The model is the theoretical basis for the development of novel methods to control the impact of self-phase modulation in ultrashort pulse fiber-amplifiers. Furthermore, the stability of this kind of ultrafast amplification was analyzed. In particular, the influence of initial perturbations imposed on the pulse envelope before amplification was examined. It could be shown that small scale pertur-

7 Conclusion and Outlook

bations cause a degradation in contrast of the output pulse. It could be demonstrated that the decrease of pulse quality manifests itself in the form of satellite pulses. The relative intensities of these pulses grow with increasing B-integral and are dependent on the quality of the stretched pulse before amplification. Thus, the nonlinear operation regime of CPA-systems requires excellent starting conditions. Based on these findings, sensible operation regimes of nonlinear CPA-systems were determined.

Moreover, novel concepts for the generation of high peak-power pulses have been designed within the scope of this thesis. Based on a simple model, pulse shaping has been applied to actively control the impact of self-phase modulation. A new method based on amplitude shaping was demonstrated for the first time in this thesis. The idea behind this technique is that the modified shape of the propagating pulse allows compensation of the self-phase modulation by the compressor. It was demonstrated experimentally that a parabolic spectrum produces nearly transform-limited pulses of nonlinear CPA-systems ($B=16$ rad), whereas standard shapes, such as sech^2 or Gauss, cause a degradation of the pulse quality. This kind of pulse-shaping must address spectral transmission characteristics in the stretcher (e.g. due to spectral efficiency of the gratings), in the pre-amplifiers or any other component before the main amplifier in order to obtain the parabolic shape in the final stage where SPM acts. Therefore, amplitude shaping requires an iterative method.

A further technique is based on phase compensation using phase-shaping. In this way, transform limited pulses can be generated from non-parabolic spectra. This type of pulse-shaping depends only on the output phase, and not on the particular evolution into the output state. Thus, ideally only one step is necessary to achieve phase cancellation. However, exact phase compensation relies on a highly accurate measurement of the residual phase due to self-phase modulation, which is very demanding. An alternative approach, which was developed in this thesis, uses model-based phase-shaping. This method requires only the measurement of the output spectrum instead of complex pulse-diagnostics. Moreover, the B-integral of the nonlinear propagation can be determined. Beyond the conventional limit due to self-phase modulation, i.e. $B = 1$ rad, nearly transform-limited pulses have been produced by a nonlinear fiber CPA-system. The pulse energy was as high as 1 mJ, and the B-integral was as high as 8 rad. Compared to the system without phase-shaping, the relative peak-power has been increased by approximately a factor of two by pulse-shaping. This result constitutes a new record in terms of pulse energy at good pulse quality by a fiber-based CPA-system. The method is reproducible. In the experiment, the technique was limited by the occurrence of higher order modes and surface damage. Current developments on improved designs of the

7 Conclusion and Outlook

main fiber amplifier will solve these issues.

For the first time, it could be demonstrated experimentally that circularly polarized light is advantageous for ultrashort pulse amplifiers. In particular, circularly polarized light results in a lower B-integral than linearly polarized light, i.e. it reduces the strength of self-phase modulation. This was shown by using model-based phase-shaping. Circularly polarized light contributes efficiently to further scaling of the pulse peak-power. In addition to this advantage, this polarization state will increase the self-focussing threshold from 4 MW to about 6 MW (at a wavelength around $1.03 \mu\text{m}$)

Phase-shaping and amplitude shaping can be combined to the best advantage. Amplitude shaping can produce a flatter spectrum which has less energy in the edges. Such a spectral shape will cause a lower B-integral at the same energy level. Then, the application of phase-shaping yields to nearly transform limited output pulses. Moreover, improved high-speed pulse diagnostics will lead to solutions that better match the problem. This approach can take into account gain shaping and saturation. The future will see pulse synthesis routinely employed in ultrafast amplification systems.

The operation of CPA-systems in the nonlinear regime will require an improved quality of the stretched pulse before amplification. Future developments will have to address this topic. In this context, the incorporation of elements possessing negative nonlinear indexes of refraction should be considered, such as semiconductors or cascaded quadratic nonlinearities. This will allow passive management of self-phase modulation; moreover, the degradation of pulse contrast due to small scale perturbations can be offset.

The ultimate limits of energy scaling in state-of-the-art ultrafast fiber amplifiers are given by surface damage and self-focussing. Controlling the impact of nonlinearity up to these limits seems feasible. However, the complexity of pulse-shaping devices should be reduced. The flexibility offered by adaptive pulse shaping will pave the way for compact ultrafast amplification systems. For instance, the phase-mismatch between a compact stretcher and compressor can be compensated by the pulse-shaper. Higher average power and peak-power will be obtained from increasingly compact systems. This will turn the ultrafast fiber laser into a standard instrument in many laboratories and in industrial applications.

Bibliography

- [1] A. W. Snyder, J. D. Love, *Optical Waveguide Theory* (Chapman & Hall, 1983).
- [2] P. Russell, "Photonic Crystal Fibers," *Science* **299**, 358-362 (2003).
- [3] M. Koshiba and K. Saitoh, "Applicability of classical optical fiber theories to holey fibers," *Opt. Lett.* **29**, 1739-1741 (2004).
- [4] N. A. Mortensen *et al.*, "Modal cutoff and the v parameter in photonic crystal fibers," *Opt. Lett.* **28**, 1879-1881 (2003).
- [5] J. D. Jackson, *Classical Electrodynamics* 3rd ed. (Wiley, 1999).
- [6] Z. Zhu, T. G. Brown, "Full-vectorial finite-difference analysis of microstructured optical fibers," *Opt. Expr.* **10**, 853-864 (2002).
- [7] W. Koechner, *Solid-State Laser Engineering* 5th edition (Springer, 1999).
- [8] E. Snitzer, "Proposed Fiber Cavities for Optical Masers," *Journal of Applied Physics* **32**, 36-39 (1961).
- [9] H. Zellmer *et al.*, "High-power cw neodymium-doped fiber laser operating at 9.2 W with high beam quality," *Opt. Letters* **20**, 578-580 (1995).
- [10] H.-R. Müller, J. Kirchhof, V. Reichel, S. Unger, "Fibers for high-power lasers and amplifiers," *C. R. Physique* **7**, 154-162 (2006).
- [11] H. M. Pask *et al.*, "Ytterbium-Doped Silica Fiber Lasers: Versatile Sources for the 1-1.2 μm Region," *IEEE J. Sel. Top. Quantum Electron.* **1**, 2-13 (1995).
- [12] R. Paschotta, J. Nilsson, A. C. Tropper, and D.C. Hanna, "Ytterbium-Doped Fiber Amplifiers," *IEEE J Quantum Electron.* **33**, 1049-1056 (1997).
- [13] C. Hönniger *et al.*, "Ultrafast Ytterbium-doped bulk lasers and laser amplifiers," *Appl. Phys. B.* **69**, 3-17 (1999).
- [14] Liekki Application Designer, <http://www.liekki.fi>.
- [15] D. E. McCumber, "Einstein Relations Connecting Broadband Emission and Absorption Spectra," *Physical Review* **136**, A954-A957 (1964).
- [16] X. Peng, and L. Dong, "Temperature dependence of ytterbium-doped fiber amplifiers," *J. Opt. Soc. Am. B* **25**, 126-130 (2008)
- [17] S. Jetschke *et al.*, "Efficient Yb laser fibers with low photodarkening by optimization of the core composition," *Opt. Express* **16**, 15540-15545 (2008).

Bibliography

- [18] G. Mourou, "The ultrahigh-peak-power laser: present and future," *Appl. Phys. B* **65**, 205-211 (1997).
- [19] W. H. Lowdermilk and J. E. Murray, "The multipass amplifier: Theory and numerical analysis," *J. Appl. Phys.* **51**, 2436-2444 (1980).
- [20] J. V. Moloney, A. C. Newell, *Nonlinear Optics* (Westview Press, 2004).
- [21] A. E. Siegman, *Lasers* (University Science Books, 1986).
- [22] Y. Wang, H. Po, "Dynamic Characteristics of Double-Clad Fiber Amplifiers for High-Power Pulse Amplification," *J. Lightwave Technol.* **21**, 2262- (2003).
- [23] L. M. Frantz, J. S. Nodvik, "Theory of Pulse Propagation in a Laser Amplifier," *J. Appl. Phys.* **34**, 2346-2349 (1963).
- [24] D. N. Schimpf *et al.*, "Compensation of pulse-distortion in saturated laser amplifiers," *Opt. Expr.* **16**, 17637-17646 (2008).
- [25] D. Bäuerle, *Laser Processing and Chemistry* 3rd edition (2000, Springer).
- [26] W. Shaikh *et al.*, "Development of an amplified variable shaped long pulse system for Vulcan," in *Central Laser Facility Annual Report* (CCLRC Rutherford Appleton Laboratory, 2005/2006) p. 199.
- [27] K. T. Vu *et al.*, "Adaptive pulse shape control in a diode-seeded nanosecond fiber MOPA system," *Opt. Expr.* **14**, 10996-11001 (2006).
- [28] M.-J. Li *et al.*, "Al/Ge co-doped large mode area fiber with high SBS threshold," *Opt. Expr.* **15**, 8290-8299 (2007).
- [29] C. Le Blanc, P. Curley, F. Salin, "Gain-narrowing and gain-shifting of ultra-short pulses in Ti:sapphire amplifiers," *Opt. Commun.* **131**, 391-398 (1996).
- [30] T. Feurer, lecture notes, University Bern.
- [31] U. Keller, "Recent developments in compact ultrafast lasers," *Nature* **242**, 831-838 (2003).
- [32] C. W. Wong, *Introduction to Mathematical Physics, Methods & Concepts* (Oxford University Press, 1991).
- [33] P. M. W. French, "The generation of ultrashort laser pulses," *Rep. Prog. Phys.* **58**, 169-267 (1995).
- [34] G. P. Agrawal, *Nonlinear Fiber Optics* 3rd edition (Academic Press, 2001).
- [35] Q. Ye *et al.*, "Dispersion Measurement of Tapered Air-Silica Microstructure Fiber by White-Light Interferometry," *Appl. Opt.* **41**, 4467-4470 (2002).
- [36] L. Lepetit *et al.*, "Linear techniques of phase measurement by femtosecond spectral interferometry for applications in spectroscopy," *J. Opt. Soc. Am. B* **12**, 2467-2474 (1995).

Bibliography

- [37] K. Saitoh, M. Koshiba, "Empirical relations for simple design of photonic crystal fibers," *Opt. Express* **13**, 267-274 (2005).
- [38] P. N. Butcher, D. Cotter, *The Elements of Nonlinear Optics* (Cambridge University Press, 1990).
- [39] M. Börner, R. Müller, R. Schiek, G. Trommer, *Elemente der integrierten Optik* (B. G. Teubner, 1990).
- [40] A. Yariv, and P. Yeh *Optical Waves in Crystals* (Wiley, 1984).
- [41] R. W. Boyd, *Nonlinear Optics* 2nd edition (Academic Press, 2003).
- [42] P. D. Maker, R. W. Terhune, C. M. Savage, "Intensity-Dependent Changes in the Refractive Index of Liquids," *Phys. Rev. Lett.* **12**, 507-507 (1964).
- [43] L. F. Mollenauer *et al.*, "Experimental observation of picosecond pulse narrowing and solitons in optical fibers," *Phys. Rev. Lett.* **45**, 1095 (1980).
- [44] M. E. Fermann *et al.*, "Self-Similar Propagation and Amplification of Parabolic Pulses in Optical Fibers," *Phys. Rev. Lett.* **84**, 6010-6013 (2000).
- [45] G. P. Agrawal *et al.*, "Temporal and spectral effects of cross-phase modulation on copropagating ultrashort pulses in optical fibers," *Phys. Rev. A* **40**, 5063-5072 (1989).
- [46] S. A. Akhmanov, V. A. Vysloukh, A. S. Chirkin, *Optics of Femtosecond Laser Pulses* p. 93-98 (American Institute of Physics, 1992).
- [47] J. Limpert, F. Röser, T. Schreiber, A. Tünnermann, "High-Power Ultrafast Fiber Laser Systems," *IEEE J. Sel. Top. Quantum Electron.* **12**, 233-244 (2006).
- [48] Y. Zaouter *et al.*, "Stretcher-free high energy nonlinear amplification of femtosecond pulses in rod-type fibers," *Opt. Lett.* **33**, 107-109 (2008).
- [49] A. V. Smith *et al.*, "Optical Damage Limits to Pulse Energy From Fibers," *IEEE J. Sel. Top. Quantum Electron.* **15**, 153-158 (2009).
- [50] J. M. Dudley *et al.*, "Self-similarity in ultrafast nonlinear optics," *nature photonics* **3**, 597-602 (2007).
- [51] M. Siegel *et al.*, "Microjoule pulse energy from a chirped-pulse Ti:sapphire oscillator with cavity dumping," *Opt. Lett.* **34**, 740-742 (2009).
- [52] J. Neuhaus *et al.*, "Subpicosecond thin-disk laser oscillator with pulse energies of up to 25.9 microjoules by use of an active multipass geometry," *Opt. Express* **16**, 20530-20539 (2008).
- [53] T. Südmeyer *et al.*, "Femtosecond laser oscillators for high-field science," *Nature photonics* **2**, 599-604 (2008).
- [54] D. M. Strickland, G. Mourou, "Compression of amplified chirped optical pulses," *Opt. Commun.* **56**, 219-221 (1985).

Bibliography

- [55] A. Galvanauskas *et al.*, “All-fiber femtosecond pulse amplification circuit using chirped Bragg gratings,” *Appl. Phys. Lett.* **66**, 1053 (1995).
- [56] K. Liao *et al.*, “Large-aperture chirped volume Bragg grating based fiber CPA system,” *Opt. Express* **15**, 4876-4882 (2007).
- [57] T. Clausnitzer *et al.*, “Highly-dispersive dielectric transmission gratings with 100% diffraction efficiency,” *Opt. Express* **16**, 5577-5584 (2008).
- [58] G. Stobrawa, “Aufbau und Anwendungen eines hochauflösenden Impulsformers zur Kontrolle ultrakurzer Laserimpulse,” PhD thesis, Friedrich Schiller University Jena, <http://www.db-thueringen.de> (2003).
- [59] E. Treacy, “Optical pulse compression with diffraction gratings,” *IEEE J. Quantum Electron.* **5**, 454-458 (1969).
- [60] O. Martinez, “Design of high-power ultrashort pulse amplifiers by expansion and recompression,” *IEEE J. Quantum Electron.* **23**, 1385-1387 (1987).
- [61] G. Cheriaux *et al.*, “Aberration-free stretcher design for ultrashort-pulse amplification,” *Opt. Lett.* **21**, 414-416 (1996).
- [62] H. C. Kapteyn, S. J. Backus, “Downchirped pulse amplification,” US patent 7072101 (2006).
- [63] V. Bagnoud and F. Salin, “Influence of optical quality on chirped-pulse amplification: characterization of a 150-nm-bandwidth stretcher,” *J. Opt. Soc. Am. B* **16**, 188-193 (1999).
- [64] J. M. Sousa, and O. G. Okhotnikov. “Multimode er-doped fiber for single transverse-mode amplification,” *Applied Physics Letters*, **74**, 1528 (1999).
- [65] J. P. Koplow, D. A. V. Kliner, and L. Goldberg, “Single-mode operation of a coiled multimode fiber amplifier,” *Opt. Lett.*, **25**, 442-444 (2000).
- [66] J. A. Alvarez-Chavez *et al.*, “Mode selection in high power cladding pumped fibre lasers with tapered section,” *Conference on Lasers and Electro-Optics (CLEO)* (1999).
- [67] Y. Jeong *et al.*, “Ytterbium-doped large-core fiber laser with 1.36 kW continuous-wave output power,” *Optics Express* **12**, 6088-6092 (2004).
- [68] J. M. Fini, “Intuitive modeling of bend distortion in large-mode-area fibers,” *Optics Letters*, **32**, 1632-1634 (2007).
- [69] J. W. Nicholson *et al.*, “Demonstration of bend-induced nonlinearities in large-mode-area fibers,” *Opt. Lett.*, **32**, 2562-2564 (2007).
- [70] N. A. Mortensen and J. R. Folkenberg, “Low-loss criterion and effective area considerations for photonic crystal fibres,” *Journal of Optics A: Pure and Applied Optics* **5**, 163-167 (2003).

Bibliography

- [71] J. Limpert *et al.*, “Extended single-mode photonic crystal fiber lasers,” *Optics Express* **14**, 2715-2720 (2006).
- [72] A. P. Napartovich, and D. V. Vysotsky, “Theory of spatial mode competition in a fiber amplifier,” *Phys. Rev. A* **76**, 063801 (2007).
- [73] N. Andermahr, and C. Fallnich, “Interaction of transverse modes in a single-frequency few-mode fiber amplifier caused by local gain saturation,” *Opt. Expr.* **16**, 8678-8684 (2008).
- [74] M. Gong *et al.*, “Numerical modeling of transverse mode competition in strongly pumped multimode fiber lasers and amplifiers,” *Opt. Expr.* **15**, 3236-3246 (2007).
- [75] G. Bouwmans *et al.*, “High-power Er: Yb fiber laser with very high numerical aperture pumpcladding waveguide,” *Applied Physics Letters*, **83**, 817 (2003).
- [76] F. Röser *et al.*, “Millijoule pulse energy high repetition rate femtosecond fiber chirped-pulse amplification system,” *Opt. Lett.***32**, 3495-3497 (2007).
- [77] N. V. Didenko *et al.*, “Contrast degradation in a chirped-pulse amplifier due to generation of prepulses by postpulses,” *Opt. Expr.* **16**, 3178-3190 (2008).
- [78] D. N. Schimpf *et al.*, “The impact of spectral modulations on the contrast of pulses of nonlinear chirped-pulse amplification systems,” *Opt. Expr.***16**, 10664-10674 (2008).
- [79] D. N. Schimpf *et al.*, “Decrease of pulse-contrast in nonlinear chirped-pulse amplification systems due to high-frequency spectral phase ripples,” *Opt. Expr.***16**, 8876-8886 (2008).
- [80] D. Anderson *et al.*, “Wave breaking in nonlinear-optical fibers,” *J. Opt. Soc. Am. B* **9**, 1358-1361 (1992).
- [81] A. Chong, L. Kuznetsova, F. W. Wise, “Theoretical optimization of nonlinear chirped pulse fiber amplifiers,” *J. Opt. Soc. Am. B* **24**, 1815-1823 (2007).
- [82] V. N. Mahajan, “Zernike annular polynomials for imaging systems with annular pupils,” *J. Opt. Soc. Am.* **71**, 75-85 (1981).
- [83] M. D. Perry, T. Ditmire, and B. C. Stuart, “Self-phase modulation in chirped-pulse amplification,” *Opt. Lett.* **19**, 2149-2151 (1994).
- [84] C. Dorrer, and J. Bromage, “Impact of high-frequency spectral phase modulation on the temporal profile of short optical pulses,” *Opt. Expr.* **16**, 3058-3068 (2008).
- [85] A. Galvanauskas *et al.*, “Generation of high-energy femtosecond pulses in multi-core Yb-fiber chirped-pulse amplification systems,” *Opt. Lett.* **26**, 935-937 (2001).
- [86] B. C. Walker, C. Toth, D. Fittinghoff, T. Guo, “Theoretical and experimental spectral phase error analysis for pulsed laser fields,” *JOSA B* **16**, 1292-1298 (1999).

Bibliography

- [87] M. Abramowitz, I. A. Stegun, "Handbook of Mathematical Functions with Formulas, Graphs, and Mathematical Tables," Generating Function for the Bessel-function, formula 9.1.41 (Dover Publications, 1970).
- [88] M. Zepf *et al.*, "Role of the plasma scale length in the harmonic generation from solid targets," Phys. Rev. E **58**, R5253-R5256 (1998).
- [89] D. N. Schimpf *et al.*, "Controlling the influence of SPM in fiber-based chirped pulse amplification systems by using an actively shaped parabolic spectrum," Opt. Expr.**15**, 16945-16953 (2007).
- [90] S. Zhou *et al.*, "Compensation of nonlinear phase shifts with third-order dispersion in short-pulse fiber amplifiers," Opt. Expr. **13**, 4869-4877 (2005).
- [91] Y. Zaouter *et al.*, "Transform-limited 100 μ J, 340 MW pulses from a nonlinear-fiber chirped-pulse amplifier using a mismatched grating stretcher-compressor" Opt. Lett. **33**, 1527-1529 (2008).
- [92] M. E. Fermann *et al.*, "All-fiber Chirped Pulse Amplification System," US patent 7414780 (2008).
- [93] L. Kuznetsova, and F. W. Wise, "Scaling of femtosecond Yb-doped fiber amplifiers to tens of microjoule pulse energy via nonlinear chirped pulse amplification," Opt. Lett. **18**, 2671-2673 (2007).
- [94] L. Shah and M. E. Fermann, "High-power Ultrashort-Pulse Fiber Amplifiers," IEEE J. Sel. Top. Quantum Electron. **22**, 552-558
- [95] J. Prawiharjo *et al.*, "High fidelity femtosecond pulses from an ultrafast fiber laser system via adaptive amplitude and phase pre-shaping," Opt. Expr. **16**, 15074-15089 (2008).
- [96] O. A. Konoplev, and D. D. Meyerhofer, "Cancellation of B-integral Accumulation for CPA Lasers," IEEE J. Sel. Top. Quantum Electron. **4**, 459-469 (1998).
- [97] G. Zhu *et al.*, "Nonlinear distortion free fiber-based chirped pulse amplification with self-phase modulation up to 2π ," Opt. Expr. **16**, 2530-2534 (2007).
- [98] A. Braun, S. Kane, and T. Norris, "Compensation of self-phase modulation in chirped-pulse amplification laser systems," Opt. Lett. **22**, 615-617 (1997).
- [99] M. M. Wefers, and K. A. Nelson, "Analysis of programmable ultrashort waveform generation using liquid-crystal spatial light modulators," J. Opt. Soc. Am. B **12**, 1343-1362 (1995).
- [100] E. Hecht, *Optics* 2nd edition (Addison-Wesley, 1987).

Publications

Parts of this thesis are published in the following peer-reviewed journal papers and conference proceedings:

Journal Papers

- D. N. Schimpf, E. Seise, T. Eidam, J. Limpert, and A. Tünnermann, “Control of the optical Kerr-effect in CPA-systems using model-based phase-shaping,” *Opt. Lett.* **34**, 3788-3790 (2009).
- D. N. Schimpf, T. Eidam, E. Seise, S. Hädrich, J. Limpert, and A. Tünnermann, “Circular vs linear polarization in laser-amplifiers with Kerr-nonlinearity,” *Opt. Expr.* **17**, 18774-18781 (2009).
- D. N. Schimpf, E. Seise, J. Limpert, and A. Tünnermann, “Self-phase modulation compensated by positive dispersion in chirped-pulse systems,” *Opt. Expr.* **17**, 4997-5007 (2009).
- D. N. Schimpf, C. Ruchert, D. Nodop, J. Limpert, and A. Tünnermann, and Francois Salin, “Compensation of pulse-distortion in saturated laser amplifiers,” *Opt. Expr.* **16**, 17637-17646 (2008).
- D. N. Schimpf, E. Seise, J. Limpert, and A. Tünnermann, “The impact of spectral modulations on the contrast of pulses of nonlinear chirped-pulse amplification systems,” *Opt. Expr.* **16**, 10664-10674 (2008).
- D. N. Schimpf, E. Seise, J. Limpert, and A. Tünnermann, “Decrease of pulse-contrast in nonlinear chirped-pulse amplification systems due to high-frequency spectral phase ripples,” *Opt. Expr.* **16**, 8876-8886 (2008).
- D. N. Schimpf, J. Limpert, and A. Tünnermann, “Controlling the influence of SPM in fiber-based chirped-pulse amplification systems by using an actively shaped parabolic spectrum,” *Opt. Expr.* **15**, 16945-16953 (2007).
- D. N. Schimpf, J. Rothhardt, J. Limpert, A. Tünnermann, and D. C. Hanna, “Theoretical analysis of the gain bandwidth for noncollinear parametric amplification of ultrafast pulses,” *J. Opt. Soc. Am. B* **24**, 2837-2846 (2007).
- J. Limpert, F. Röser, D. N. Schimpf, E. Seise, T. Eidam, S. Hädrich, J. Rothhardt, C. Jauregui Misas, and A. Tünnermann, “High Repetition Rate Gigawatt Peak

Power Fiber Laser Systems: Challenges, Design, and Experiment,” *IEEE J. Sel. Top. of Quantum Electron.* **15**, 159-169 (2009).

- F. Röser, T. Eidam, J. Rothhardt, O. Schmidt, D. N. Schimpf, J. Limpert, and A. Tünnermann, “Millijoule pulse energy high repetition rate femtosecond fiber chirped-pulse amplification system,” *Opt. Lett.* **32**, 3495-3497 (2007).
- F. Röser, D. Schimpf, O. Schmidt, B. Ortaç, K. Rademaker, J. Limpert, and A. Tünnermann, “90 W average power 100 μ J energy femtosecond fiber chirped-pulse amplification system,” *Opt. Lett.* **32**, 2230-2232 (2007).
- J. Rothhardt, S. Hädrich, D. N. Schimpf, J. Limpert, and A. Tünnermann, “High repetition rate fiber amplifier pumped sub-20 fs optical parametric amplifier,” *Opt. Expr.* **15**, 16729-16736 (2007).
- T. Schreiber, D. Schimpf, D. Müller, F. Röser, J. Limpert, and A. Tünnermann, “Influence of pulse shape in self-phase-modulation-limited chirped pulse fiber amplifier systems,” *J. Opt. Soc. Am. B* **24**, 1809-1814 (2007).
- T. Schreiber, T. Andersen, D. Schimpf, J. Limpert, and A. Tünnermann, “Supercontinuum generation by femtosecond single and dual wavelength pumping in photonic crystal fibers with two zero dispersion wavelengths,” *Opt. Expr.* **13**, 9556-9569 (2005).
- C. Agüergaray, T. V. Andersen, D. N. Schimpf, O. Schmidt, J. Rothhardt, T. Schreiber, J. Limpert, E. Cormier, and A. Tünnermann, “Parametric amplification and compression to ultrashort pulse duration of resonant linear waves,” *Opt. Expr.* **15**, 5699-5710 (2007).
- C. Agüergaray, O. Schmidt, J. Rothhardt, D. Schimpf, D. Descamps, S. Petit, J. Limpert, and E. Cormier, “Ultra-wide parametric amplification at 800 nm toward octave spanning,” *Opt. Expr.* **17**, 5153-5162 (2009).
- D. M. Grant, D. S. Elson, D. Schimpf, C. Dunsby, J. Requejo-Isidro, E. Auksoorius, I. Munro, M. A. Neil, P. M. French, E. Nye, G. Stamp, and P. Courtney, “Optically sectioned fluorescence lifetime imaging using a Nipkow disk microscope and a tunable ultrafast continuum excitation source,” *Opt. Lett.* **30**, 3353-3355 (2005).
- J. Thomas, Christian Voigtländer, Damian Schimpf, Fabian Stutzki, Elodie Wikszak, Jens Limpert, Stefan Nolte, and Andreas Tünnermann, “Continuously chirped fiber Bragg gratings by femtosecond laser structuring,” *Opt. Lett.* **33**, 1560-1562 (2008).

Conference Papers

- T. V. Andersen, T. Schreiber, D. Schimpf, J. Limpert, and A. Tünnermann “Super-continuum generation with femtosecond dual pumping,” Photonics West (2006), paper 6103-33
- J. Limpert, D. Schimpf, J. Rothhardt, S. Hädrich, O. Schmidt, F. Röser, T. Schreiber, A. Tünnermann, C. Aguergaray, E. Cormier, T.V. Andersen and C.F. Pedersen, “Fiber laser pumped ultra-fast parametric amplifiers,” Photonics West paper 6453-22 (2007).
- F. Röser, D. Schimpf, O. Schmidt, B. Ortac, K. Rademaker, J. Limpert, and A. Tünnermann, “90-W average power high energy femtosecond fiber laser system,” Photonics West (2007), paper 6453-36.
- D. N. Schimpf, J. Limpert, and A. Tünnermann, “Amplification of actively shaped parabolic pulses in fiber-CPA system,” Photonics West (2007), postdeadline paper 6453-5.
- D. N. Schimpf, J. Rothardt, J. Limpert, and A. Tünnermann, “Optimization of noncollinear optical parametric amplification,” Photonics West (2007), paper 6455-11.
- D. Schimpf, D. Müller, S. Hädrich, T. Schreiber, J. Limpert, and A. Tünnermann, “Control of Nonlinearity in Fiber CPA System by Pulse Shaping,” in Advanced Solid-State Photonics, (2007), paper TuC2.
- D. N. Schimpf, D. Müller, S. Hädrich, F. Röser, J. Limpert, and A. Tünnermann, “High Quality Fiber CPA-System at a B-Integral of 16,” in Conference on Lasers and Electro-Optics (2007), paper CMEE6.
- F. Röser, J. Rothhardt, T. Eidam, O. Schmidt, D.N. Schimpf, A. Ancona, S. Nolte, J. Limpert, and A. Tünnermann, “Millijoule Pulse Energy High Repetition Rate Femtosecond Fiber CPA System: Results, Micromachining Application and Scaling Potential,” Photonics West (2008), postdeadline paper.
- D. Nodop, S. Linke, D. Schimpf, C. Jauregui, J. Limpert, and A. Tünnermann “Long Period Gratings written in Large-Mode-Area Photonic Crystal fibers,” Photonics West (2008), paper 6873-32.
- D. N. Schimpf, J. Limpert, and A. Tünnermann, “The influence of the spectral amplitude on the performance of chirped pulse large mode-area fiber-amplifiers,” Photonics West (2008), talk 6873-56.
- D. N. Schimpf, S. Hädrich, J. Rothhardt, J. Limpert, A. Tünnermann, and David Hanna, “Optimization of the gain bandwidth for noncollinear parametric amplification of ultrafast pulses,” Photonics West (2008), talk 6875-31.

- F. Röser, T. Eidam, J. Rothhardt, O. Schmidt, D. Schimpf, J. Limpert, and A. Tünnermann, "Millijoule Pulse Energy High Repetition Rate Femtosecond Fiber CPA System," in *Advanced Solid-State Photonics* (2008), paper TuA5.
- J. Rothhardt, S. Hädrich, D. Schimpf, J. Limpert, and A. Tünnermann, "High Repetition Rate-Sub 20 fs Optical Parametric Amplifier Pumped by High Power Fiber Amplifier," in *Advanced Solid-State Photonics* (2008), paper TuA3.
- F. Röser, D. Schimpf, J. Rothhardt, T. Eidam, J. Limpert, A. Tünnermann, and F. Salin, "Gain Limitations and Consequences for Short Length Fiber Amplifiers," in *Advanced Solid-State Photonics*(2008), paper WB22.
- F. Röser, J. Rothhardt, T. Eidam, O. Schmidt, D. N. Schimpf, J. Limpert, and A. Tünnermann, "Millijoule Pulse Energy High Repetition Rate Femtosecond Fiber CPA System," in *Conference on Lasers and Electro-Optics* (2008), paper CThB2.
- D. N. Schimpf, J. Limpert, A. Tünnermann, and F. Salin, "Seed Pulse Optimization for Saturated Fiber-Amplifiers," *Conference on Lasers and Electro-Optics* (2008), paper: CThB6.
- F. Röser, J. Rothhardt, T. Eidam, O. Schmidt, D.N. Schimpf, A. Ancona, S. Nolte, J. Limpert, and A. Tünnermann, "Millijoule Pulse Energy High Repetition Rate Femtosecond Fiber CPA System: Results, Micromachining Application and Scaling Potential," *Conference on Ultrafast Phenomena* (2008), paper Mon4A.4.
- S. Hädrich, J. Rothhardt, F. Röser, D. Schimpf, J. Limpert, and A. Tünnermann, "2 MHz repetition rate - 15 fs fiber amplifier pumped optical parametric amplifier," *Conference on Ultrafast Phenomena* (2008), paper FRI1P.6.
- F. Röser, D. N. Schimpf, C. Jauregui, J. Limpert, A. Tünnermann, "45 W 980 nm single transverse mode Yb-doped fiber laser," *Europhoton Conference* (2008), paper TuoC.2 .
- D. Schimpf, E. Seise, J. Limpert, and A. Tünnermann, "Degradation of pulse-contrast of nonlinear CPAsystems due to high-frequency spectral amplitude and phase modulations," *Europhoton Conference* (2008), paper TUp.12.
- D. N. Schimpf, E. Seise, J. Limpert, A. Tünnermann, "Sensitivity of nonlinear fiber CPA-systems to initial spectral amplitude modulations and spectral phase ripples," *Photonics West* (2009), paper 7195-91.
- D. N. Schimpf, C. Ruchert, D. Nodop, J. Limpert, A. Tünnermann, "Compensation of pulse-shaping due to saturation in fiber-amplifiers," *Photonics West* (2009), paper 7195-49.
- D. N. Schimpf, E. Seise, J. Limpert, and A. Tünnermann, "Analysis of Nonlinear CPA-Systems with Real Input Pulses," in *Advanced Solid-State Photonics* (2009), paper TuB7.

- C. Jauregui, T. Eidam, D. N. Schimpf, J. Limpert, and A. Tünnermann, “Raman Threshold for CW Double-Clad Fiber Amplifiers,” in *Advanced Solid-State Photonics (2009)*, paper TuB27.
- D. N. Schimpf, E. Seise, J. Limpert, and A. Tünnermann, “Ultra-Compact CPA-System with Intrinsic Phase-Compensation,” in *Advanced Solid-State Photonics (2009)*, paper TuB6.
- S. Hädrich, J. Rothhardt, T. Eidam, D. N. Schimpf, F. Röser, J. Limpert, and A. Tünnermann, “Peak Power Scaling towards Ultrashort Pulses at High Repetition Rates,” in *Conference on Lasers and Electro-Optics (2009)*, paper CWK1.
- F. Röser, T. Eidam, J. Rothhardt, S. Hädrich, D. N. Schimpf, J. Limpert, and A. Tünnermann, “High Time for Fibers-Towards kW Class Laser Systems with GW Peak Power,” in *Conference on Lasers and Electro-Optics (2009)*, paper CThJ1.
- D. N. Schimpf, E. Seise, J. Limpert, and A. Tünnermann, “Self-phase modulation compensated by positive dispersion in chirped pulse systems,” *UFO/HSFW (2009)*, paper P1.9.
- E. Seise, T. Eidam, D. N. Schimpf, J. Limpert, and A. Tünnermann, “Pulse quality improvement in high repetition-rate mJ pulse energy fiber CPA-system by active phase-shaping,” *UFO/HSFW (2009)*, paper P1.24.
- D. Schimpf, E. Seise, T. Eidam, S. Hädrich, J. Limpert, and A. Tünnermann, “Advantage of circularly polarized light in nonlinear fiber-amplifiers,” accepted for conference *Photonics West 2010*
- D. Schimpf, F. Röser, J. Limpert, and A. Tünnermann, “Spectral-temporal management of Yb-doped fiber CPA-systems ,” accepted for conference *Photonics West 2010*
- E. Seise, T. Eidam, D. Schimpf, J. Limpert, and A. Tünnermann, “Transform-limited pulses from a mJ-class nonlinear fiber CPA-system by phase shaping,” accepted for conference *Photonics West 2010*
- E. Seise, D. Schimpf, J. Limpert, and A. Tünnermann, “Improved performance of nonlinear CPA-systems by spectral clipping,” accepted for conference *Photonics West 2010*
- D. Nodop, C. Jauregui, D. Schimpf, J. Limpert, and A. Tünnermann, “Efficient near-infrared light conversion to visible and mid-infrared radiation in an endlessly single-mode photonic crystal fiber,” accepted for conference *Photonics West 2010*

Patents

- D. Schimpf *et al.*, Patentanmeldetitel “Vorrichtung zum Verstärken von Lichtimpulsen,” urspr. “Chirped-pulse Verstärkersystem,” DE 10 2008 047 226.3, DPMA-Anmeldung 12.09.2008
- J. Limpert, D. Schimpf, A. Tünnermann, Patentanmeldetitel “Vorrichtung zum Verstärken von Lichtimpulsen,” urspr. “Ultrakurzpulsverstärker mit spektraler Formung,” DE 10 2008 063 368.2, DPMA-Anmeldung 30.12.2008
- D. Schimpf *et al.*, “Vorrichtung zum Verstärken und/oder Transportieren von elektromagnetischer Strahlung,” urspr. “Laser-Verstärkern mit nicht-linear polarisiertem Licht,” DE 10 2009 032 803.3, DPMA-Anmeldung 10.07.2009

Zusammenfassung

Pulsformung in faseroptischen Verstärkersystemen

Die raschen Fortschritte in der Entwicklung des faseroptischen Ultrakurzpulslasers hat das Forschungsgebiet an einen Punkt gebracht, in dem nun kommerziell verfügbare Quellen in speziellen industriellen und wissenschaftlichen Anwendungen zum Einsatz kommen. Um das Anwendungsgebiet dieser Technologie weiter auszudehnen, werden derzeit Möglichkeiten zur Steigerung der Pulsenergie und Pulsspitzenleistung erforscht. Der Aufbau solcher Systeme erfordert jedoch die Berücksichtigung von Sättigungseffekten und von nichtlinearem Verhalten. Das Ziel der vorliegenden Arbeit ist es, die Wirkung dieser Effekte durch Pulsformung zu steuern und somit Nachteile zu vermeiden.

Herkömmlicherweise müssen bei der Verstärkung von ultrakurzen Pulsen nichtlineare Effekte vermieden werden, da nur so eine hohe Qualität des Ausgangspulses und damit nutzbare hohe Pulsspitzenleistungen zu erreichen sind. In faseroptischen Ultrakurzpulsverstärkern kommt daher das Verfahren der Verstärkung von gestreckten Pulsen und Großkernfasern zum Einsatz. All diese Methoden werden in modernen Systemen angewendet. Trotzdem wird die Skalierung der Pulsenergie durch das Auftreten von nichtlinearen Effekten begrenzt. Der Einfluss von nichtlinearen Effekten äußert sich durch eine schnelle Abnahme der Pulsqualität. Die Entwicklung von neuen Methoden zur Kontrolle des Einflusses der nichtlinearen Effekte ist daher ein entscheidender Schritt hin zu verbesserten faseroptischen Kurzpulsverstärkersystemen. Insbesondere, erlauben solche Verfahren eine weitere Skalierung der Pulsenergie.

Ein Ziel der vorliegenden Arbeit ist es, ein Modell für die Verstärkung von gestreckten Pulsen unter dem Einfluss von Nichtlinearität zu entwickeln. Es konnte gezeigt werden, dass die Wirkung der Selbstphasenmodulation durch eine spektrale Phase beschrieben werden kann. Der Verlauf der Phase entspricht der Gestalt des Spektrums und der maximale Phasenhub wird durch das B-Integral bestimmt. Aufgrund dieser theoretischen Untersuchungen konnte experimentell gezeigt werden, dass Selbstphasenmodulation gestreckter Pulse durch positive Dispersion kompensiert werden kann. An dieser Stelle sei darauf hingewiesen, dass für nahezu bandbreitenbegrenzte Pulse negative Dispersion mit einem Ausgleich von Selbstphasenmodulation in Verbindung gebracht wird.

Das Model bildet insbesondere die Grundlage für Verfahren zur Kontrolle der Selbstphasenmodulation in faseroptischen Ultrakurzpulsverstärkern. Darüber hinaus wurde die Stabilität dieser Art von Verstärkung untersucht. Insbesondere wurde der Einfluss kleiner Störungen auf der Einhüllenden des zu verstärkenden Pulses beschrieben. Es konnte im Rahmen dieser Arbeit gezeigt werden, dass kleine Störungen des Pulses vor der Verstärkung einen starken Einfluss auf den Kontrast der Ausgangspulse haben. Diese Verschlechterung des Pulskontrasts äußert sich in Form von Nebenpulsen. Die Intensitäten der Nebenpulse steigen mit zunehmendem B-Integral und sind von der Qualität des zu verstärkenden Pulses abhängig. Der nichtlineare Verstärkungsbereich erfordert daher eine exzellente Pulsqualität. Durch diese Untersuchungen konnten sinnvolle Operationsbereiche bestimmt werden.

Die Entwicklung neuer Verfahren zur Steigerung der Pulsspitzenleistung stellt einen wesentlichen Schwerpunkt dieser Arbeit dar. Pulsformung kommt zum Einsatz, um den Einfluss der Nichtlinearität zu steuern. Das entwickelte Modell findet hier seine Anwendung. Eine Methode basiert auf der aktiven Formung der Amplitude. Das Prinzip des Verfahrens ist, dass eine veränderte Form des sich ausbreitenden Pulses eine Kompensation der Selbstphasenmodulation durch den Kompressor erlaubt. Es konnte experimentell gezeigt werden, dass ein parabolisches Spektrum nahezu bandbreitenbegrenzte Pulse am Verstärkerausgang ermöglicht, wohingegen herkömmliche spektrale Formen wie z.B. Gauß oder sech^2 zu einer Verschlechterung der Pulsqualität führten. Zwischen der Formung der Amplitude und der Verstärkerdynamik besteht jedoch eine Wechselwirkung. Das Verstärkerverhalten hängt stark von der Signalintensität ab. Darüber hinaus müssen in diesem Verfahren Veränderungen des Spektrums im Strecker (z.B. durch die spektrale Effizienz der Gitter), als auch in den Vorverstärkern oder in anderen optischen Komponenten mit berücksichtigt werden, um ein parabelförmiges Spektrum im letzten Abschnitt des Hauptverstärkers, dort wo die Nichtlinearität wirkt, zu erhalten. Amplitudenformung erfordert somit ein iteratives Verfahren.

Im Rahmen dieser Arbeit wurde auch die Phase aktiv geformt. Mit dieser Methode konnten nahezu bandbreitenbegrenzte Pulse am Verstärkerausgang auch für nicht-parabelförmige Spektren realisiert werden. Ein Vorteil dieses Verfahrens ist, dass die Kompensation nur von der Ausgangsphase abhängig ist und nicht von der Entwicklung in diesen Ausgangszustand. Idealerweise ist daher nur ein Schritt notwendig um die Phase auszugleichen. Eine Phasenkompensation mittels Phasenformung ist nur dann exakt durchführbar, wenn die Restphase genau bekannt ist. Allerdings muss hierfür diese Phase exakt gemessen werden, was wiederum sehr aufwendig ist. Im Rahmen dieser Arbeit wurde daher eine alternative Herangehensweise entwickelt. Das Verfahren

beruht auf einer modellbasierten Formung der Phase. Die Methode erfordert nur eine Messung des Spektrums anstatt einer komplizierten Messung der Phase. Darüber hinaus kann das B-Integral der nichtlinearen Ausbreitung des Pulses experimentell bestimmt werden. Jenseits des herkömmlichen, von Nichtlinearität beschränkten Arbeitsbereiches, konnten bandbreitenbegrenzte Pulse von einem faseroptischen Verstärkersystem erzeugt werden. Die Pulsenergie war 1 mJ hoch. Das B-Integral wurde zu 8 rad bestimmt. Im Vergleich zu dem System ohne Pulsformung konnte die relative Pulsspitzenleistung mittels adaptiver Phasenformung um mehr als einen Faktor zwei erhöht werden. Dieses Ergebnis stellt einen beachtlichen Fortschritt hinsichtlich Pulsqualität und Pulsspitzenleistung dar. Das Verfahren arbeitet reproduzierbar. Experimentell wurde die Technik durch das Auftreten von höheren Moden begrenzt. Verbesserte Faserdesigns werden dieses Problem jedoch in naher Zukunft beheben.

Im Rahmen dieser Arbeit konnte zum ersten Mal experimentell nachgewiesen werden, dass die Verwendung von zirkular polarisiertem Licht für die nichtlineare Ultrakurzpulsverstärkung vorteilhaft ist. Mittels der modellbasierten Phasenformung konnte gezeigt werden, dass das B-Integral für zirkular polarisiertes Licht gegenüber linear polarisiertem Licht reduziert ist. Darüber hinaus lässt sich mit zirkular polarisiertem Licht die Schwelle für Selbstfokussierung (bei einer Wellenlänge von 1 μm) von ungefähr 4 MW auf 6 MW erhöhen.

Die Formung von Phase und Amplitude kann auch kombiniert werden. Solch eine Herangehensweise sollte noch bessere Ergebnisse liefern, da ein Spektrum, welches so verändert wird, dass es insgesamt flacher ist und weniger Energie in den Rändern aufweist, ein kleineres B-Integral bei gleicher Pulsenergie liefert. Amplitudenformung könnte solch ein vorteilhaftes Spektrum erzeugen. Dann sollte Phasenformung ausgeführt werden, um bandbreitenbegrenzte Pulse zu erzeugen. Darüber hinaus könnten genauere Verfahren zur Charakterisierung von Pulsen zu einer besser an das Problem angepassten Lösung führen. Die Verstärkerdynamik könnte so auch mit berücksichtigt werden.

In naher Zukunft wird der Pulsformer ein Standardinstrument in jedem größeren Ultrakurzpulsverstärker sein. Für den erfolgreichen Einsatz im nichtlinearen Regime muss jedoch die Qualität des zu verstärkenden Pulses verbessert werden. Zukünftige Arbeiten müssen sich mit diesem Thema intensiv beschäftigen. In diesem Zusammenhang sollte auch über den Einbau von Materialien mit einer negativen nichtlinearen Brechzahl, wie z.B. Halbleiter oder quadratische Nichtlinearitäten, nachgedacht werden. Mit diesen Elementen ist neben der Kontrolle von Selbstphasenmodulation auch eine Verbesserung des Pulskontrasts möglich.

Die Zerstörung der Faserendfläche als auch Selbstfokussierung stellen ultimative Beschränkungen für die Steigerung der Ausgangsenergie in faseroptischen Verstärkern dar. Eine Kontrolle der Nichtlinearität bis zu diesen Grenzen erscheint durchführbar. Hierfür sollte jedoch die Komplexität der Pulsformer reduziert werden. Der Einsatz von adaptiver Pulsformung eröffnet neue Möglichkeiten. Kompakte Verstärkersysteme können aufgebaut werden; z. B. kann der Pulsformer die Phasenfehlpassung zwischen einem kompakten Strecker und dem Kompressor ausgleichen. Höhere Durchschnittsleistungen und Pulsspitzenleistungen können so von zunehmend kompakteren Systemen produziert werden. Dies wird den faseroptischen Ultrakurzpulslaser zu einem Standardinstrument in vielen Laboren und in industriellen Anwendungen machen.

Acknowledgements

I gratefully acknowledge the support of many people during the course of this thesis:

I would like to thank Prof. Andreas Tünnermann for giving me the chance to work on this interesting project in the outstanding infrastructure at the Institute of Applied Physics at Friedrich Schiller University Jena.

Special thanks to Dr. Jens Limpert for his assistance, for allowing me great latitude, and for supporting ideas.

I would like to say a special thanks to my diploma students Doreen Müller, Clemens Ruchert, and Enrico Seise.

Thank you to all past and present colleagues at the institute, in particular Dr. Cesar Jauregui Misas, Dirk Nodop, Alexander Steinmetz, Tino Eidam, Steffen Hädrich, Jan Rothhardt, Fabian Röser, Oliver Schmidt, Fabian Stutzki, Marco Plötner, Dr. Bülel Ortac, Martin Baumgartl, Jens Thomas, Gabor Mathäus, and Dr. Stefan Nolte.

Finally, I would like to thank my family and friends.

Lebenslauf

Damian Nikolaus Schimpf

geb. am 6. März 1980

in Halle (Saale)

Juni 1998

Abitur am Ernst-Abbe-Gymnasium, Jena

1998 - 1999

Zivildienst beim Deutschen Roten Kreuz, Jena

2000 - 2005

Studium der Physik an der
an der Friedrich-Schiller-Universität Jena

2004 - 2005

externe Diplomarbeit am Imperial College, London

November 2005

Hochschulabschluß Diplomphysiker,
Friedrich-Schiller-Universität Jena

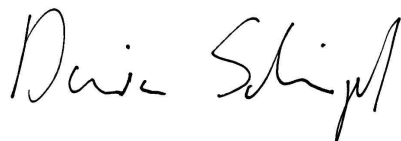
ab Dezember 2005

wissenschaftlicher Mitarbeiter am
Institut für Angewandte Physik,
Friedrich-Schiller-Universität Jena

2006 - 2009

Doktorand am
Institut für Angewandte Physik,
Friedrich-Schiller-Universität Jena

Jena, den 28.9.2009

Handwritten signature of Damian Schimpf in black ink.

Ehrenwörtliche Erklärung

Ich erkläre hiermit ehrenwörtlich, dass ich die vorliegende Arbeit selbständig, ohne unzulässige Hilfe Dritter und ohne Benutzung anderer als der angegebenen Hilfsmittel und Literatur angefertigt habe. Die aus anderen Quellen direkt oder indirekt übernommenen Daten und Konzepte sind unter Angabe der Quellen gekennzeichnet.

Bei der Auswahl und Auswertung folgenden Materials haben mir die nachstehend aufgeführten Personen in der jeweils beschriebenen Weise entgeltlich/unentgeltlich geholfen:

Barbara Albrethsen-Keck (Fremont, CA, USA), Englischkorrektur

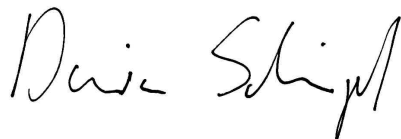
Weitere Personen waren an der inhaltlich-materiellen Erstellung der vorliegenden Arbeit nicht beteiligt. Insbesondere habe ich hierfür nicht die entgeltliche Hilfe von Vermittlungs- bzw. Beratungsdiensten (Promotionsberater oder andere Personen) in Anspruch genommen. Niemand hat von mir unmittelbar oder mittelbar geldwerte Leistungen für Arbeiten erhalten, die im Zusammenhang mit dem Inhalt der vorgelegten Dissertation stehen.

Die Arbeit wurde bisher weder im In- noch im Ausland in gleicher oder ähnlicher Form einer anderen Prüfungsbehörde vorgelegt.

Die geltende Promotionsordnung der Physikalisch-Astronomischen Fakultät ist mir bekannt.

Ich versichere ehrenwörtlich, dass ich nach bestem Wissen die reine Wahrheit gesagt und nichts verschwiegen habe.

Jena, den 28.9.2009

A handwritten signature in black ink, reading "Denise Schippl". The signature is written in a cursive, flowing style.